1-1-2004

X-ray metallicities and luminosity functions of galaxy clusters

Sandip Thanki
University of Nevada, Las Vegas

X-RAY METALLICITIES AND LUMINOSITY FUNCTIONS OF GALAXY CLUSTERS

by

Sandip Thanki

Bachelor of Science
Widener University
1997

Master of Science
University of Nevada Las Vegas
1999

A dissertation submitted in partial fulfillment
of the requirements for the

Doctor of Philosophy Degree in Physics
Department of Physics
College of Science

Graduate College
University of Nevada, Las Vegas
December 2004

UMI Number: 3176941

UNLV

Dissertation Approval
The Graduate College
University of Nevada, Las Vegas

11/18, 20 04

The Dissertation prepared by

Sandip G. Thanki

Entitled

X-ray Metallicities and Luminosity Functions of Galaxy Clusters

is approved in partial fulfillment of the requirements for the degree of

Doctor of Philosophy in Physics

Nov 18 2004

Examination Committee Chair

Dean of the Graduate College

Examination Committee Member

Examination Committee Member

Graduate College Faculty Representative

PR/1017-52/1-00

ABSTRACT

X-ray Metallicities and Luminosity Functions of Galaxy Clusters

by

Sandip Thanki

Dr. George Rhee, Examination Committee Chair
Associate Professor
University of Nevada, Las Vegas

We present a comparison of the photometric quantities of rich galaxy clusters to their X-ray metallicity (Z). The intra-cluster medium (ICM) is enriched with more metals than expected for a primordial gas. The most plausible source of the metals are the constituent galaxies, in particular, supernovae winds from those galaxies. In an effort to probe the Z variations, we studied photometric quantities of a sample of galaxy clusters. White (2000) and Horner (2001) present X-ray data for large samples of clusters, including their metallicity. We analyzed photometric data for a sample of 35 clusters chosen from their list. Here, we present luminosity functions for those clusters with a metallicity range of 0.00 to 0.42 $Z_{\odot}$. There is a possible decrease in r band characteristic magnitude (M_r^*), of the luminosity functions for the clusters, as their metallicity increases. This result favors the hypothesis of ICM enrichment due to supernovae winds.

TABLE OF CONTENTS

LIST OF TABLES

LIST OF FIGURES

ACKNOWLEDGEMENTS

I would like to thank my advisor Dr. George Rhee and our collaborator Dr. Jason Pinkney for their guidance. I also thank my committee members Dr. Lon Spight, Dr. Stephen Lepp and Dr. David Emerson.

I thank John Kilburg for introducing me to Perl, Awk, and many other tools that made my work efficient. I am thankful to Mark Hancock Greg Piet, Daniel Koury and Tae Song Lee for their help and support.

Finally, I thank my family, especially my wife Tejal for her patience.

This research has made extensive use of NASA's Astrophysics Data System Bibliographic Services

CHAPTER 1

INTRODUCTION

First studied in visible light in the early 20^{th} century by Wolf (1906), clusters of galaxies are massive, virialized, high density systems consisting of a few hundred to thousand galaxies bound by self-gravity in a radius of about 2 Mpc. Cluster galaxies are predominantly ellipticals or S0s, and an exceptionally massive galaxy called a cD galaxy is found in the center of many of the clusters (Sarazin 1988). The total luminosity of a galaxy cluster is $\sim 10^{12}$ $L_{\odot}$ (Parolin et al. 2003). Galaxy clusters are the largest objects whose total masses can be directly estimated using their velocity dispersion. They have velocity dispersions of $300 - 1800$ km/s (Struble & Rood 1999) and the masses are on the order of $10^{14} - 10^{15}$ $M_{\odot}$ (Carlberg et al. 1996). The space between the galaxies is filled with gas that has a temperature of $\sim 10^{7} - 10^{8}$K (White 2000; Ikebe et al. 2002; Horner 2001). The number density of the gas molecules is on the order of $10^{-2} - 10^{-4}$ cm^{-3} (Schindler 2004), and bremsstrahlung radiation from this intra-cluster medium (ICM) can be detected through X-rays. The mass of the ICM is about 2-10 times the mass of the cluster galaxies. The combined mass of the ICM and the galaxies is $\lesssim 30\%$ of the virial mass of the cluster (Horner 2001).

1.1 Intra-cluster Metallicity and The Enrichment Mechanisms

The X-ray spectra of ICMs contain lines of heavy elements (White 2000; Horner 2001). The lines correspond to metallicities of about 0.2 to 0.4 in solar units. This finding implies that the ICM cannot be purely primordial. Part of the gas must

have come from the inter-stellar medium (ISM) of the constituent galaxies of the clusters. A variety of mechanisms can be responsible for the transport of the parts of ISM into the ICM.

Schindler (2004) discusses four well-accepted processes that can potentially enrich the ICM: ram-pressure stripping, galactic winds, galaxy-galaxy interaction and jets from active galaxies.

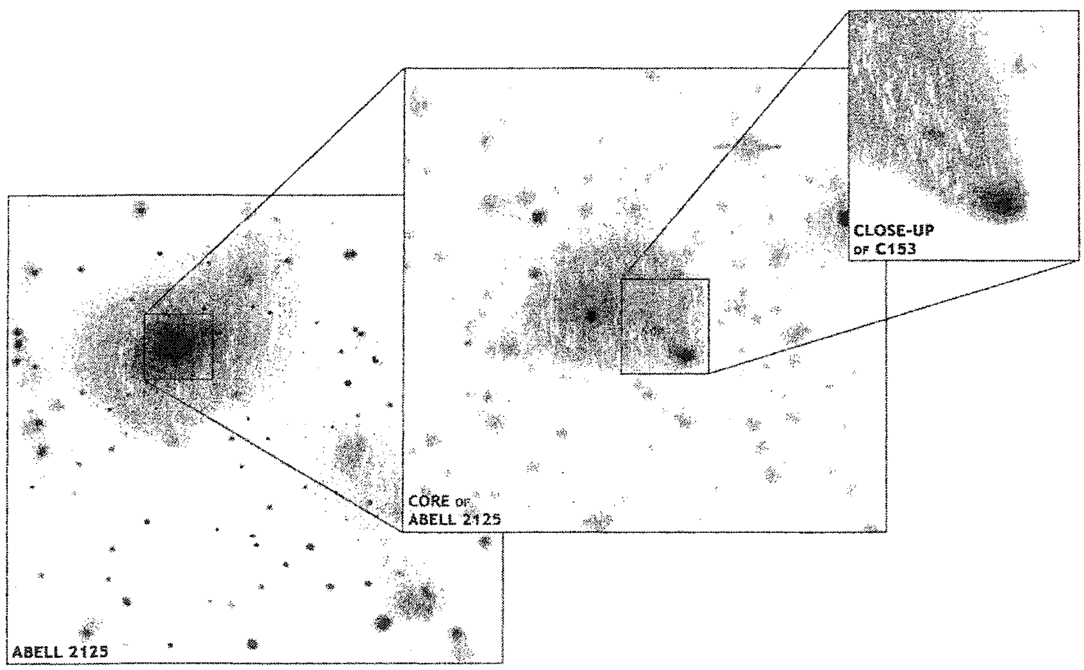

Figure 1 Evidence ICM enrichment by ram-pressure stripping in an X-ray image of Abell 2125 taken by the Chandra Telescope (Wang et. al 2004)

First suggested by Gunn & Gott (1972), ram-pressure stripping is a mechanism in which a galaxy approaching the cluster center experiences the increasing pressure of the ICM and loses its metal enriched ISM to the intra-cluster gas. As described by Shu (1982), this mechanism is analogous to the wind knocking the hat off a rapidly pedaling cyclist. Figure 1 shows this mechanism at work in the cluster Abell 2125. An X-ray trail appears on one side of the fast-moving galaxy C153 due

to ram-pressure stripping (Wang et. al 2004).

Simulations done by Bekki et. al (2002) suggest that ram-pressure stripping could also be responsible for transforming spiral galaxies into passive spirals with weak or absent star formation. Hubble Space Telescope observations have revealed significant numbers of passive spiral galaxies in distant clusters (e.g. Dressler et. al 1999). Passive spiral galaxies are likely to be a key galaxy population in transition between red, elliptical/S0 galaxies in low-redshift clusters and blue, spiral galaxies more numerous in higher-redshift clusters (Goto et. al 2003). This could provide an explanation for the Butcher-Oemler effect which shows that the fraction of spiral galaxies increases with redshift (Butcher & Oemler 1984). If ram-pressure stripping is a dominant mechanism for ICM enrichment, a redshift-metallicity connection can be expected. The ICM metallicity should decrease with increasing redshift. Mushotzky & Loewenstein (1997) and Horner (2001) find no evolution in ICM abundance with increasing redshift. Better metallicity measurements are needed to reach a definitive conclusion. Since ram-pressure stripping is density dependent, Renzini (1997) has argued that it cannot have played a major role because a correlation between velocity-dispersion, a property related to cluster density, and metallicity is not supported by observations. This has motivated us to compare redshift with metallicity and compare ICM metallicity with the galaxy number density of the clusters.

Galactic winds, driven by supernovae, are another possible process for ICM enrichment. The out-flowing enriched supernova gas is blown into the ICM. Mathews & Baker (1971) proposed that the absence of observable gas in ellipticals can be due to the heating produced by supernova blast waves. Calculations show that enough metals can be passed on to the ICM by the cluster galaxies in a time shorter than the Hubble time, under a variety of initial conditions, to have present amount of

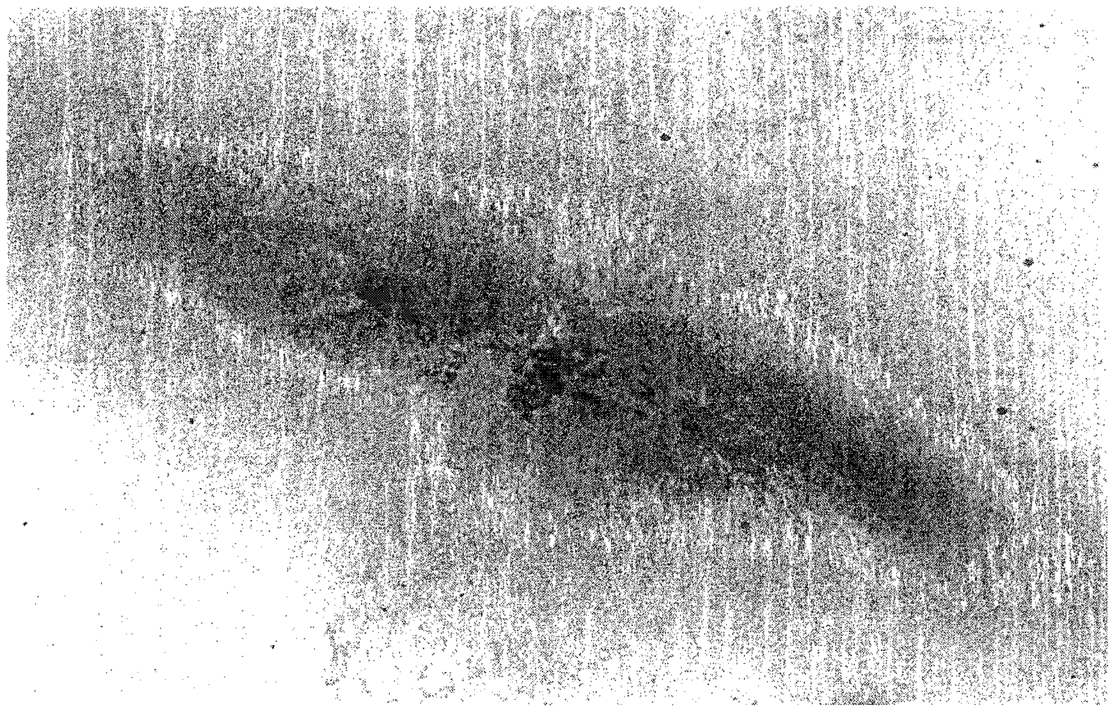

Figure 2 Evidence for ICM enrichment by Supernova Winds in a B,V and H_α image of the Cigar Galaxy M82 taken by the Subaru Telescope (Lehnert 1999)

ICM metallicity (De Young 1978).

Figure 2, an image of the Cigar Galaxy M82 taken by the Subaru Telescope, shows this process enriching the halo with the winds moving towards the ICM (Lehnert 1999).

It has been suggested that decreasing galactic mass can lead to increasing outflow of metals from the galaxies due to that fact that lower-mass galaxies have shallower potential wells (Larson 1974; Larson & Dinerstein 1975). This implies that the ICM metallicity would increase with increasing number of low-mass galaxies. It has been shown that the ISM metallicity increases with increasing galaxy mass in low-mass galaxies (Tamura 2001). This could mean that high mass galaxies would retain their metallicity more efficiently than low mass galaxies, implying a ICM metallicity-mass relation. For a constant mass-to-light ratio, this would translate to a metallicity-

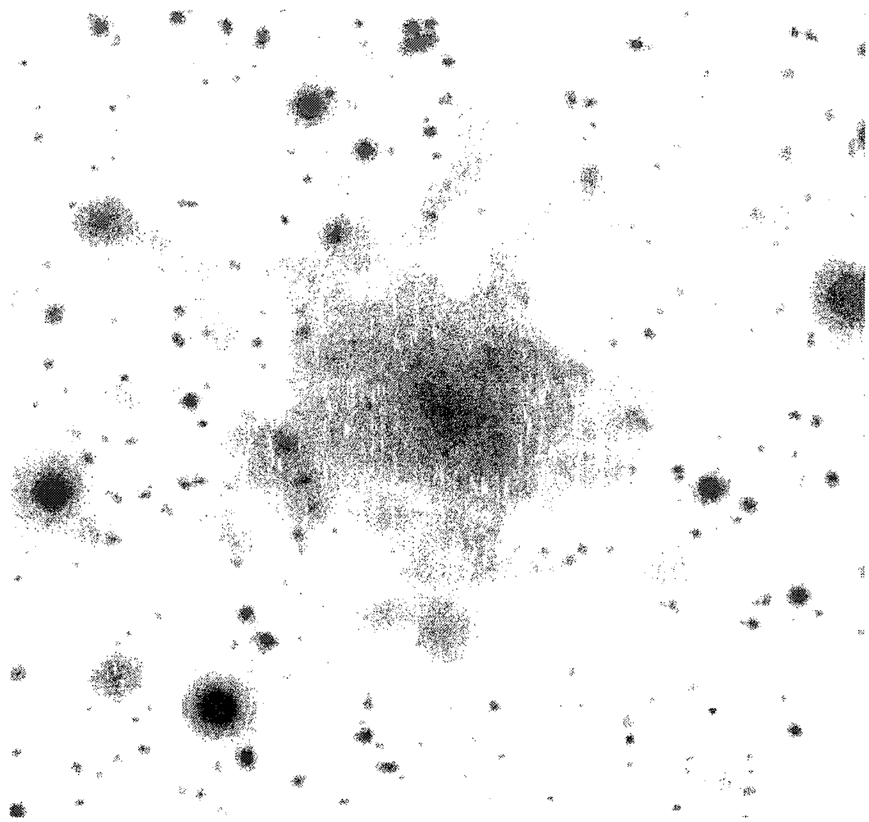

Figure 3 Evidence for ICM enrichment by Mergers in a composite image of the cluster RDCS 1252.9-2927 with the X-ray data from the Chandra and XMM-Newton X-ray telescopes and the optical data from the Hubble Space Telescope and ground based VLT (Rosati et al. 2003)

luminosity relation. A cluster with larger ICM metallicity can be expected to have larger number of low-mass (low-luminosity) galaxies. This idea is tested in this project.

Galaxy-galaxy interactions, or galactic mergers, also play a role in passing on the ISM metallicity to ICM. Close encounters between two or more galaxies can tidally strip gas from the galaxies into the ICM. Such encounters can also result into mergers blowing part of the interstellar gas into the ICM. Figure 3, a composite of and X-ray and optical data of the cluster RDCS 1252.9-2927 at the redshift of 1.24, shows X-ray concentration around the galaxies merging toward the cluster center

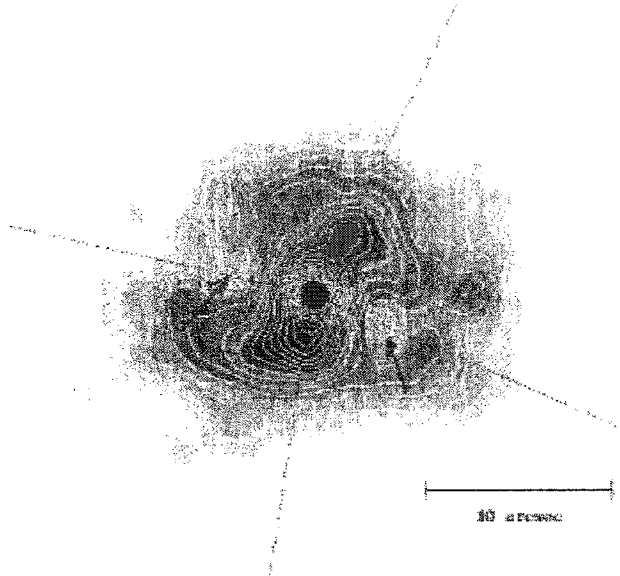

Figure 4 Evidence for ICM enrichment by Jets in an X-ray image of the cluster RBS767 from the Chandra telescope (De Filippis 2002)

(Rosati et al. 2003). The X-ray data is from the Chandra and XMM-Newton X-ray telescopes and the optical data is from the Hubble Space Telescope and ground based VLT. Enriched X-ray emission from the merging galaxies indicate outflow of the gas into the ICM. The galaxy-galaxy interactions would be more common in a dense cluster or a cluster with high velocity-dispersion. As mentioned above, a correlation between metallicity and velocity-dispersion is not supported by observations.

Another possible mechanism is jets that are emitted by active galaxies in the clusters. Figure 4 shows a Chandra image of the cluster RBS767 at the redshift of 0.35. The image shows two X-ray minima, indicated by the arrows, on both side of the cluster center that indicate interaction of the galaxy jets and the ICM. The metallicity of the ICM drops radially from the cluster center, indicating enrichment of the intra-cluster gas via jets (De Filippis 2002). Therefore, the answer to the question of whether the cluster has had a history of jets can be found in the metallicity gradients.

There could exist other mechanisms, in addition to the four above, that are responsible for the metal enrichment of the intra-cluster gas. Intra-cluster supernovae have been discovered that could also enrich the ICM (Domainko et al. 2004). Dust grain expulsion by stellar radiation pressure has also been considered a potential mechanism (Wiebe 1999).

Whether one of the mechanisms discussed above is more efficient over the others and plays a dominant role in ICM enrichment is a question of debate. Computer simulations with different enrichment processes have been performed, and the results have been quite discordant. Gnendin (1998) found that galaxy mergers eject most of the gas, while galactic winds play only a minor role. Aguirre et al. (2001) argue that ram-pressure and tidal interactions are relatively ineffective in transferring metallicity to the ICM and winds are most important.

1.2 Source of Intra-cluster Metallicity

The primary source of the ICM metallicity are the galaxies within the clusters. Regardless of the processes at work, a cluster with more ICM metallicity would have had more contributions from the constituent galaxies than a cluster with low ICM metallicity. This suggests a connection between optical characteristics of the cluster galaxies and the metallicity of the ICM. A luminosity function of a cluster is one of the basic measurement of its optical data. Analytical functions can be fit to the luminosity functions to generate quantitative descriptions such as the slope of the functions at the faint end and a characteristic magnitude of the cluster.

1.3 Outline

The major goal of this work is to search for a connection between the amount of intra-cluster metallicity and its source, presumably the galaxies that move through

the intra-cluster medium.

We have obtained photometric data through observations at the MDM observatory and from the archive of Sloan Digital Sky Survey for a sample of Abell clusters (Abell 1958). Luminosity functions are generated for a sample of galaxy clusters whose metallicity is known. In efforts to find the contributions from metallicity transfer mechanisms to ICM, discussed in section 1.1, we compare the following parameters with the ICM metallicity: redshift, characteristic magnitude of the luminosity functions and the faint-end slope of the luminosity functions.

In chapter 2 we discuss how the sample for this project was selected. For better statistics the size of the sample was maximized by using all the available optical data, with redshift constraint, for the clusters whose metallicities are known.

The ICM metallicities used in this project were found using the data from the ASCA X-ray telescope. In chapter 3 we discuss the telescope and the instruments used to collect the X-ray data. We also describe the process for computing the metallicity from the X-ray data.

Preliminary optical data for this project were obtained using the MDM 1.3-m telescope at the Kitt Peak National Observatory. We describe the telescope and the instrumentation used to collect the data in chapter 4. The data reduction, done using the Image Reduction and Analysis Facility (IRAF), is also described in this chapter.

The area of the clusters on the sky could not be covered by one CCD exposure. Mosaics were created by joining several CCD images to create a single image for a cluster. In chapter 5 we discuss the process used to combine and calibration the images using the standard stars.

Once the CCD images were reduced and, if necessary, mosaiced, they were ready for star/galaxy classification and photometry. In chapter 6, we discuss the process

used for classification and photometry.

In addition to the data from our observations, we also obtained data from the Automatic Plate Measuring Catalog, maintained by the Institute of Astronomy in Cambridge, and the Sloan Digital Sky Survey undertaken at the Apache Point Observatory, in Sunspot, New Mexico. In chapter 7 we discuss the archives and compare the photometry from different sources.

Once the data was compiled, we generated cluster luminosity functions in efforts to parameterize the cluster photometry. In chapter 8 we outline the process used to generate the luminosity functions (LF), analytical functions that are fit to the LFs, and present the LFs and the fits.

In chapter 9 we present the results comparing the X-ray metallicity to the optical parameters mentioned above. We conclude with ideas for future work.

CHAPTER 2

THE SAMPLE

In this chapter, we discuss our sample selection criteria and the sources used to acquire the data for the sample.

One of the goals for this project was to investigate a possible connection between the X-ray metallicities of the intra-cluster mediums (ICM) and the luminosity functions (LF) of the galaxy clusters. White (2000) and Horner (2001) present ICM metallicities for clusters with a redshift range of 0.00 to 0.45. The method used by them to find the metallicities is described in the next chapter. Our sample is drawn from their data sets.

A luminosity function for a galaxy cluster is the number distribution for the luminosity of the cluster galaxies. Depending on the distances to the clusters and the limiting magnitude of a telescope, only certain clusters can be observed to generate meaningful luminosity functions. This is explained in the following argument. A characteristic luminosity for a galaxy cluster can be found by fitting analytical functions to the LF. One of the widely used models for galaxy cluster LF has been developed by Schechter (1976). In terms of absolute magnitude, the Schechter function for the differential LF is $n(M)dM = k\ N^*\ e^{k(\alpha+1)(M^*-M)-e^{k\ (M^*-M)}}dM$, where M^* is the characteristic magnitude, or the 'knee' of the LF, α is the slope of the faint end of the function, k =ln(10)/2.5, and N^* is determined by requiring that the total number of galaxies expected by the Schechter function equal the number of galaxies in a given magnitude range. Figure 5 is an example of a typical field corrected LF for a galaxy cluster. The characteristic magnitude, M^*, of galaxy clusters ranges around

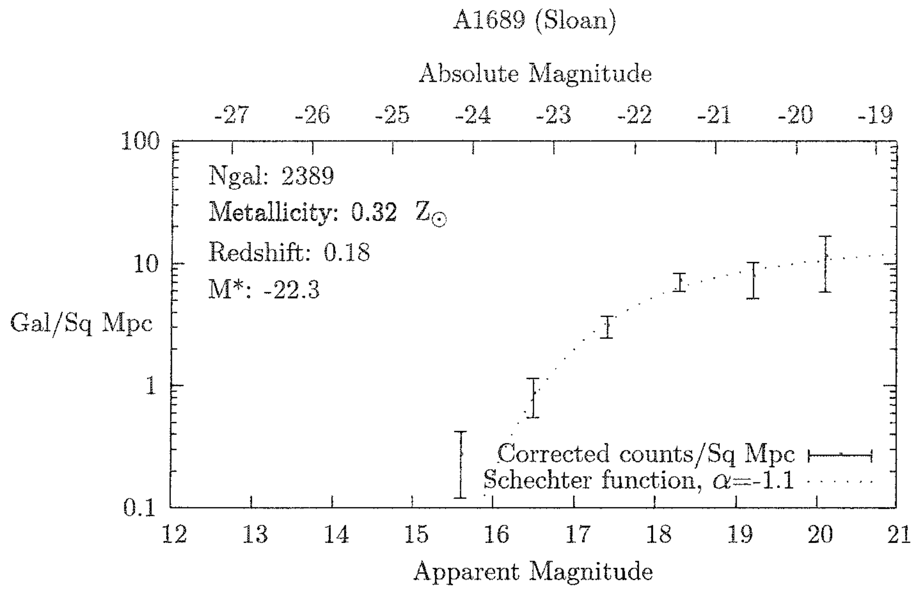

Figure 5 Luminosity function for Abell 1689

the absolute magnitude of -22. Absolute magnitude is given by $M = m - \mu - A - K_z$, where m is the apparent magnitude, μ is the distance modulus, and A is the galactic absorption. K_z is the K-correction which corrects for the stretching of the spectrum due to the redshift, and is estimated by $K_z = 2.5\ \log\,(1+z)$ (Sandage 1973). The distance modulus, $\mu = 42.384 - 5\ \log(h) + 5\ \log(z)$, where z is the redshift and $h = H_0/100$, H_0 being the Hubble constant (See Appendix for derivation of μ). Figure 5 shows M^* determined using the Schechter function for the cluster Abell 1689. In order to obtain a reliable M^* using the luminosity function, there needs be sufficient amount of data on the faint end of the LF beyond the characteristic magnitude at least up to one magnitude. To generate the LF just for the cluster, and not for the cluster field, one needs to subtract the background galaxies in the survey region from each magnitude bin. It is found using the Sloan Digital Sky Survey (SDSS) that the number of galaxies $N(m)$ per square degrees per magnitude in the

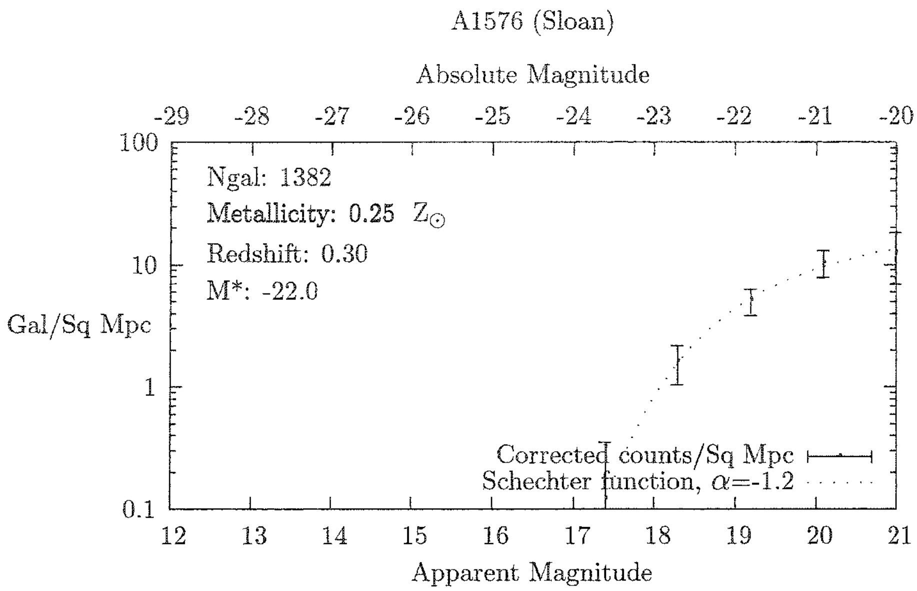

Figure 6 Luminosity function for Abell 1576

R band can be approximated by N(m)=(0.39 ±0.063) $m - (4.67 \pm 1.01)$ (Parolin et al.2003). For a distant cluster, M^* would correspond to fainter apparent magnitude than a nearby cluster. At fainter magnitudes ($\gtrsim$ 20) the number of background galaxies per square degrees would have significant contribution to the total counts from the cluster field. Therefore, the cluster contrast against the background is less strong for higher redshift clusters. This induces greater errors towards the bright end of high redshift cluster luminosity function making it difficult to determine M^* reliably. Figure 6 shows a cluster at the redshift of 0.30 with larger error-bars closer to M^* than a cluster at redshift of 0.18 (Figure 5). At higher redshifts the amount of data towards the find-end of the luminosity funciton is also less. The values of M^* corresponding to $m \lesssim 20$ would provide much more reliable characteristic magnitudes for the clusters. This can be clearly seen in Figure 5. From $m = M + \mu$, for the apparent magnitude of 20 to correspond with the absolute magnitude of -22,

typical M^* value, the upper limit on the redshift would be ~ 0.42. This effect is somewhat compensated by tendency to select richer cluster at high redshift.

Based on the availability of data that would provide reliable values for the 'knee' of the luminosity functions, we selected 34 clusters of galaxies in our sample. Data for 16 clusters were obtained at the MDM Observatory in Tuscon, Arizona in summer of 2000. The right ascension range of the MDM data was limited to 10h-18h for our observing dates. The telescope used was a 1.3 meter reflector. The magnitude limit of the telescope limited the redshift to ~ 0.2. Data for 24 clusters were obtained using the Automatic Plate Measurement (APM) archive. The selection was based on the redshift of the clusters with $z = 0.1$ being the limit. This data turned out to be non-usable for the reasons explained in Chapter 7. Data for 30 clusters were obtained from the Sloan Digital Sky Survey (SDSS). 2.5 meter SDSS telescope is capable of photometry to much fainter magnitudes than MDM and APM and therefore, the clusters chosen from SDSS had the redshift limit of $z = 0.35$. The clusters that were common among the surveys were used for comparison of the results. Data acquisition through observing and from the archives is described in the following chapters.

Table 1 shows the complete sample along with the central redshifts and the X-ray metallicities of the clusters.

Table 1 Sample

Cluster	z	$Z(\ \mathrm{Z}_\odot)$	90 %cl	Source
A0963	0.21	0.34	0.26 - 0.42	MDM
A0990	0.14	0.23	0.18 - 0.27	MDM
A1068	0.14	0.42	0.36 - 0.48	MDM
A1204	0.17	0.35	0.28 - 0.43	MDM
A1553	0.17	0.25	0.18 - 0.32	MDM
A1650	0.08	0.40	0.37 - 0.43	MDM
A1689	0.18	0.32	0.28 - 0.37	MDM
A1914	0.17	0.30	0.24 - 0.36	MDM
A1942	0.22	0.27	0.12 - 0.44	MDM
A2034	0.11	0.29	0.23 - 0.34	MDM
A2104	0.16	0.32	0.26 - 0.38	MDM
A2142	0.09	0.28	0.23 - 0.33	MDM
A2204	0.15	0.39	0.34 - 0.44	MDM
A2218	0.18	0.20	0.14 - 0.25	MDM
A2219	0.23	0.27	0.19 - 0.34	MDM
A2261	0.22	0.37	0.29 - 0.45	MDM

The Sample (Cont.)

Cluster	z	$Z(\,Z_\odot)$	90 %cl	Source
A0267	0.23	0.26	0.17 - 0.34	SDSS
A0611	0.29	0.19	0.12 - 0.27	SDSS
A0697	0.28	0.24	0.17 - 0.31	SDSS
A0773	0.20	0.29	0.20 - 0.38	SDSS
A0854	0.21	0.09	0.00 - 0.19	SDSS
A0959	0.35	0.04	0.00 - 0.19	SDSS
A0963	0.21	0.34	0.26 - 0.42	SDSS
A0990	0.14	0.23	0.18 - 0.27	SDSS
A1068	0.14	0.42	0.36 - 0.48	SDSS
A1430	0.21	0.00	0.00 - 0.08	SDSS
A1553	0.17	0.25	0.18 - 0.32	SDSS
A1576	0.30	0.25	0.14 - 0.36	SDSS
A1650	0.08	0.40	0.37 - 0.43	SDSS
A1682	0.23	0.21	0.10 - 0.32	SDSS
A1689	0.18	0.32	0.28 - 0.37	SDSS
A1704	0.22	0.37	0.26 - 0.49	SDSS
A1763	0.19	0.12	0.05 - 0.19	SDSS
A1774	0.17	0.08	0.02 - 0.14	SDSS
A1835	0.25	0.30	0.24 - 0.37	SDSS
A1914	0.17	0.30	0.24 - 0.36	SDSS
A1942	0.22	0.27	0.12 - 0.44	SDSS
A1995	0.32	0.19	0.01 - 0.36	SDSS
A2029	0.08	0.32	0.29 - 0.35	SDSS
A2034	0.11	0.29	0.23 - 0.34	SDSS
A2142	0.09	0.28	0.23 - 0.33	SDSS
A2219	0.23	0.27	0.19 - 0.34	SDSS
A2244	0.10	0.29	0.25 - 0.33	SDSS
A2255	0.08	0.31	0.26 - 0.35	SDSS
A2259	0.16	0.18	0.12 - 0.24	SDSS
A2670	0.08	0.25	0.18 - 0.33	SDSS

CHAPTER 3

X-RAY METALLICITIES OF THE ICM

In this chapter we review the X-ray instruments that collected the X-ray data used in this project, models for determining X-ray metallicities of the ICM, and the process used to find the metallicities.

3.1 The X-ray Instruments

An X-ray space telescope mission using a satellite called Advanced Satellite for Cosmology and Astrophysics (ASCA) was undertaken between 1993 and 2001. ASCA was initially named Astro-D and was launched by Japan's Institute of Space and Astonautical Science (ISAS). The X-ray telescope (XRT) on ASCA was developed as a collaboration between Japanese and U.S. scientists. It was the first XRT capable of simultaneous imaging and spectroscopic observations over an energy range of 0.5-10 keV (Tanaka et al. 1994). The ASCA XRT collected data with two types of instruments, the Gas Imaging Spectrometer (GIS) and the Solid-state Imaging Spectrometer (SIS).

GIS is an imaging gas scintillation proportional counter (IGSPC). Focused X-ray photons enter the detector through a thin beryllium entrance window into the "drift region" containing Xenon with ten percent of Helium. The X-rays ionize the Xenon atoms and the electrons produced by the ionization drift into the "scintillation region" which contains the same mixture of gases as the "drift region." The electrons in the "scintillation region" are accelerated by a strong electric field parallel to the entrance window whose voltage is such that the electrons gain enough energy to

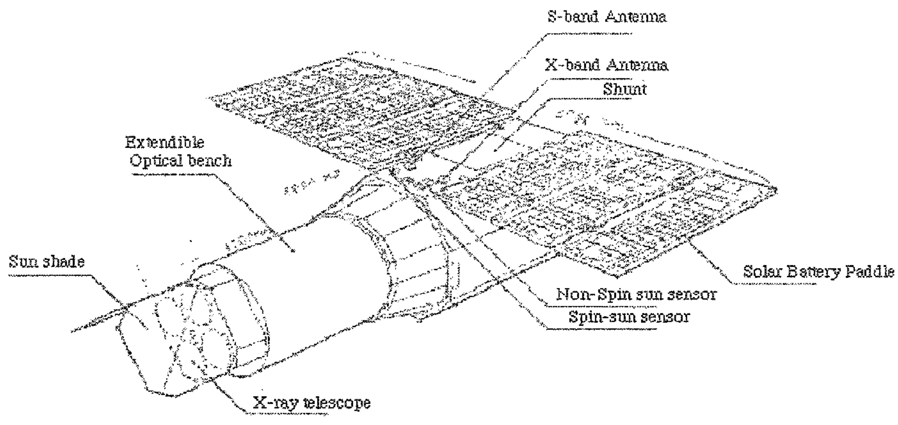

Figure 7 Diagram of ASCA

excite Xenon atoms but not to ionize them. When these exited atoms de-excite, ultra violet scintillations with their intensity proportional to the energy of the original X-ray are produced. These scintillations are then detected by the position sensitive phototube (PSPT). The two-dimensional position of the scintillation corresponds to the position of the incident X-ray photon since the electric field is parallel to the window.

SIS consists of four 420×422 pixel Charge Coupled Device (CCD) chips. The chips are arranged in an 2×2 array. Focused X-ray photons are absorbed in the body of the detector and produce electrons whose total charge is proportional to the original photon energy. Since SIS is directly exposed to X-rays, it is more prone to radiation damage than GIS.

The GIS circular field of view covers an area four times larger than the square field of view of SIS. The energy resolution of SIS, on the other hand, is up to four times better than GIS. Two SIS (SIS0 and SIS1) and two GIS (GIS2 and GIS3)

operated simultaneously through four identical X-ray telescopes. Four telescopes increased the total effective area and provided consistency checks between the instruments. Figure 7 shows a schematic diagram of ASCA. The following table summarizes some basic properties of the telescope.

Table 2 ASCA XRT

Property	Value
Length	4.7 m
Mass	417 kg
Focal Length	3.5 m
Angular Resolution	20% of the photons are within $1'$
GIS field of view	$50'$ (circular)
SIS field of view	$22' \times 22'$ (square)
Energy range	0.5-10 keV
GIS Energy Resolution ($E/\Delta E$)	$\sim$ 13 at 6 keV
SIS Energy Resolution ($E/\Delta E$)	$\sim$ 50 at 6 keV

Even though the energy range of both types of detectors is 0.5-10 keV, GIS is practically insensitive below $\sim$ 1 keV. Later in the mission accumulated radiation damage to the SIS CCDs made them unusable below 0.8 keV. Figure 8 and Figure 9 show examples of images taken by GIS and SIS instruments.

3.2 The X-ray Metallicity

The X-ray emission from hot ICM is due to thermal bremsstrahlung radiation. The emissivity, e_ν^{ff}, at frequency ν from an ion of charge Z_i with a temperature of T_x is given by,

$$e_\nu^{ff} = \frac{2^5 \pi e^6}{3 m_e c^3} \left(\frac{2\pi}{3 m_e k} \right)^{1/2} \sum_i Z_i^2 n_e n_i g_{ff}(Z_i, T_x, \nu) T^{-1/2} e^{h\nu/kT_x}.$$

where n_e and n_i are the number density of ions and electrons, respectively. The Gaunt $g_{ff}(Z_i, T_x, \nu)$, of order unity, corrects for quantum mechanical effects and for

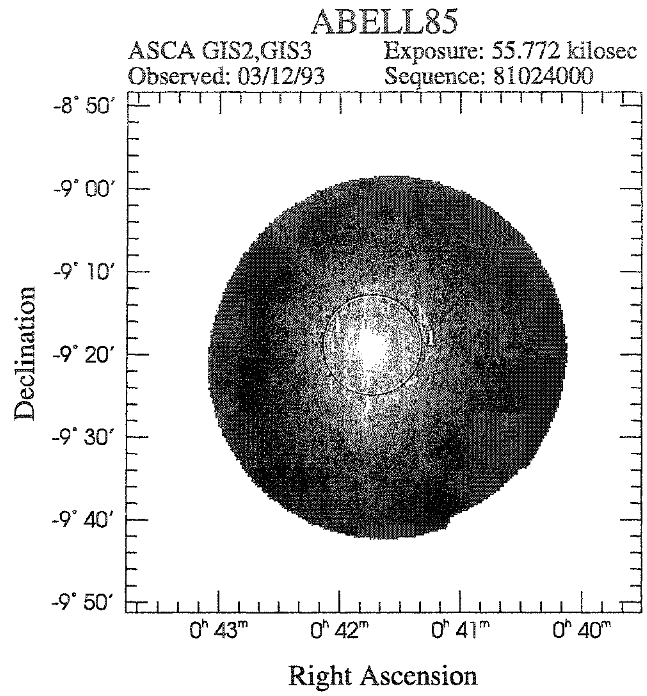

Figure 8 GIS image of Abell 0085

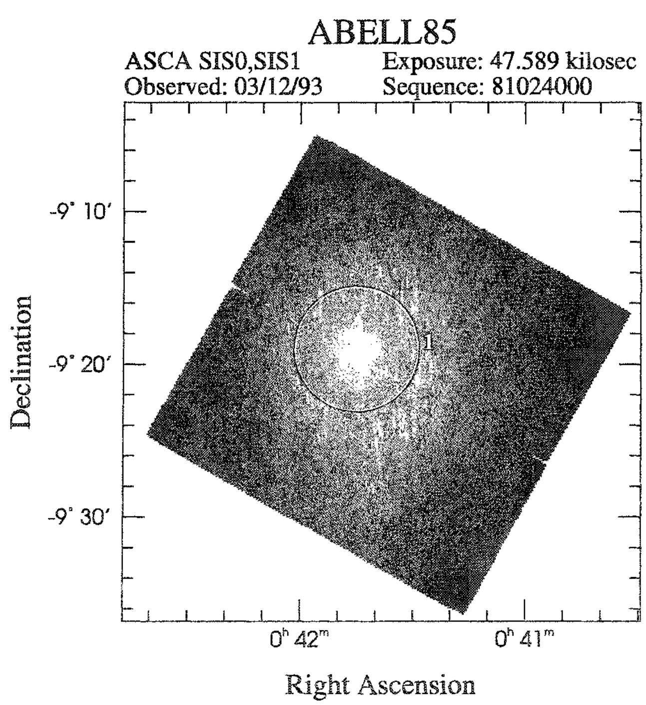

Figure 9 SIS image of Abell 0085

the effect of distant collisions. It is a slowly varying function of temperature and energy (Sarazin 1988).

White & Buote (2000) use processed GIS observations obtained from the High Energy Astrophysics Science Archive Research Center (HEASARC) database to determine the X-ray temperatures and abundances of 106 clusters. Larger field of view of GIS allows them to determine the cluster properties to larger radii. Spectra were obtained for each cluster for a band of 1-9 keV. To determine the temperature and the metallicities of the ICM gas, a spectral model is fit to the ICM spectrum of each cluster. The model used is a single thermal emission component (MEKAL: Mewe, Gronenschild, van den Oord 1985; Mewe, Lemen, van den Oord 1986), modified by foreground absorption (Morrison & McCammon 1983) of X-ray by neutral Hydrogen according its galactic column density (Stark et al. 1992). Horner (2001) also computed metallicities using the ASCA data for 273 clusters. The models used by Horner are MEKAL and Raymond-Smith (Raymond & Smith 1977).

Figure 10 through 13 show the predicted spectra by the MEKAL model for various ICM temperatures and metallicities. Figure 11 shows an a MEKAL spectra fit to an ASCA spectra of Abell 85.

Metallicities computed by White (2000)and Horner (2001) are used in this project for investigating the relationship between the metallicities and the photometric properties of the galaxy clusters.

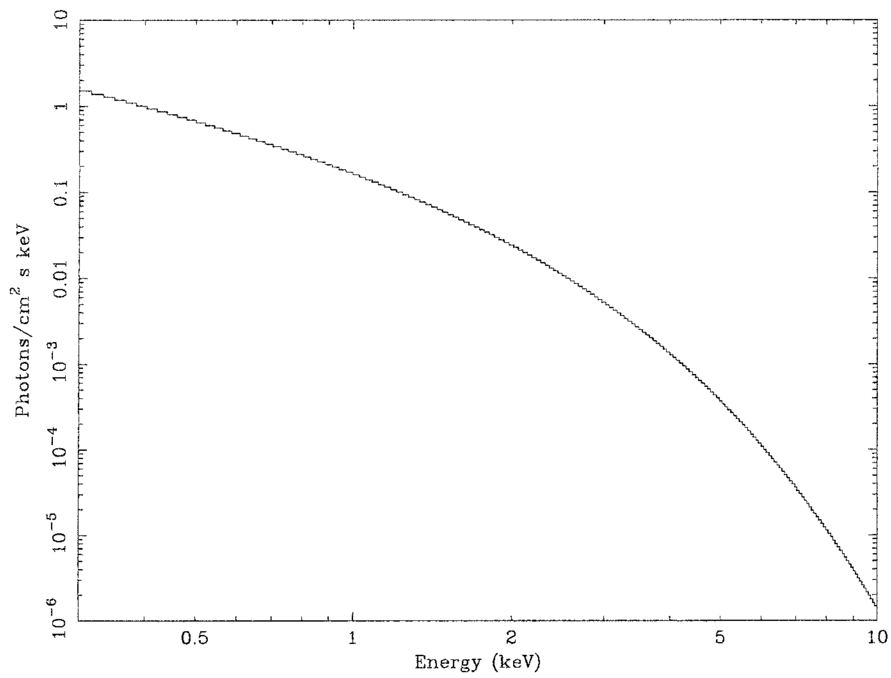

Figure 10 Zero-redshift MEKAL model for $T = 1$ keV and $Z = 0.0$ $Z_{\odot}$

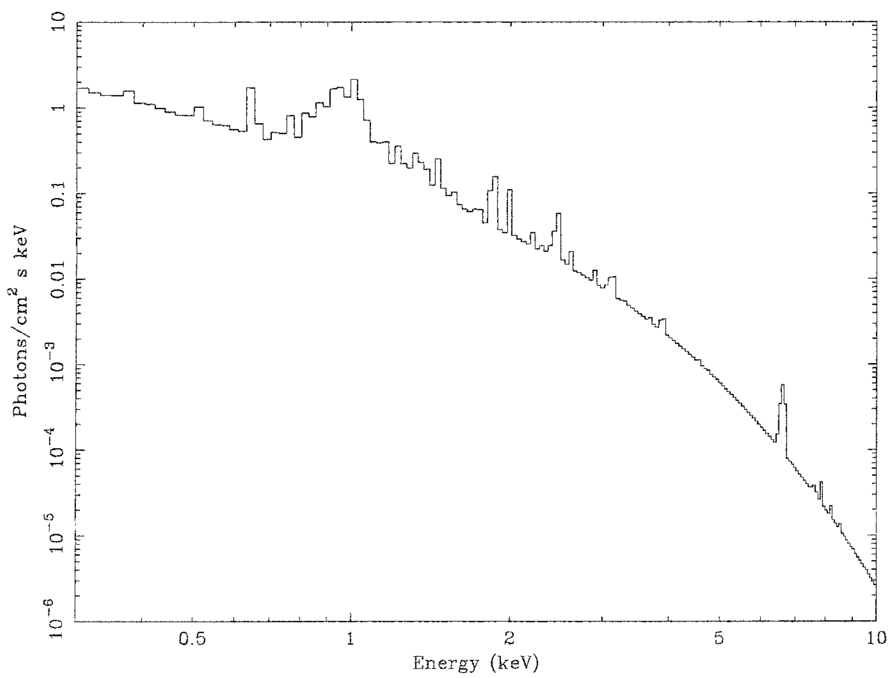

Figure 11 Zero-redshift MEKAL model for $T = 1$ keV and $Z = 0.5$ $Z_{\odot}$

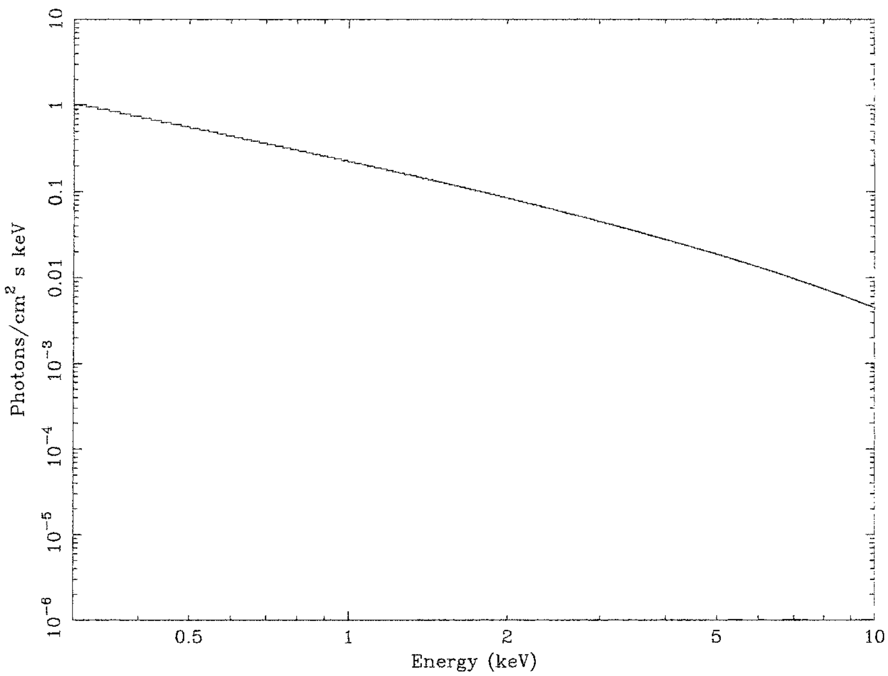

Figure 12 Zero-redshift MEKAL model for $T = 10$ keV and $Z = 0.0\ Z_\odot$

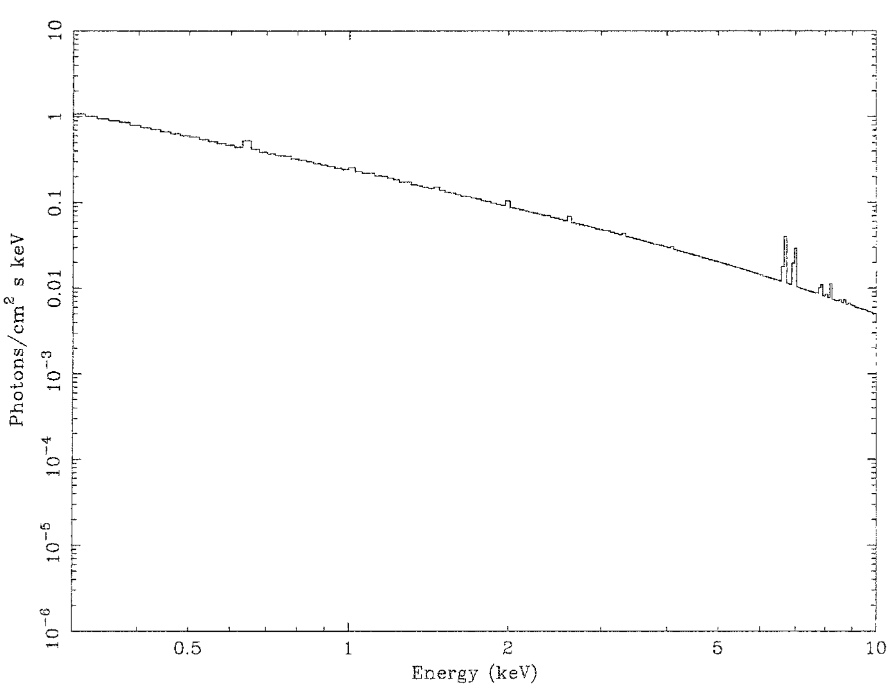

Figure 13 Zero-redshift MEKAL model for $T = 10$ keV and $Z = 0.5\ Z_\odot$

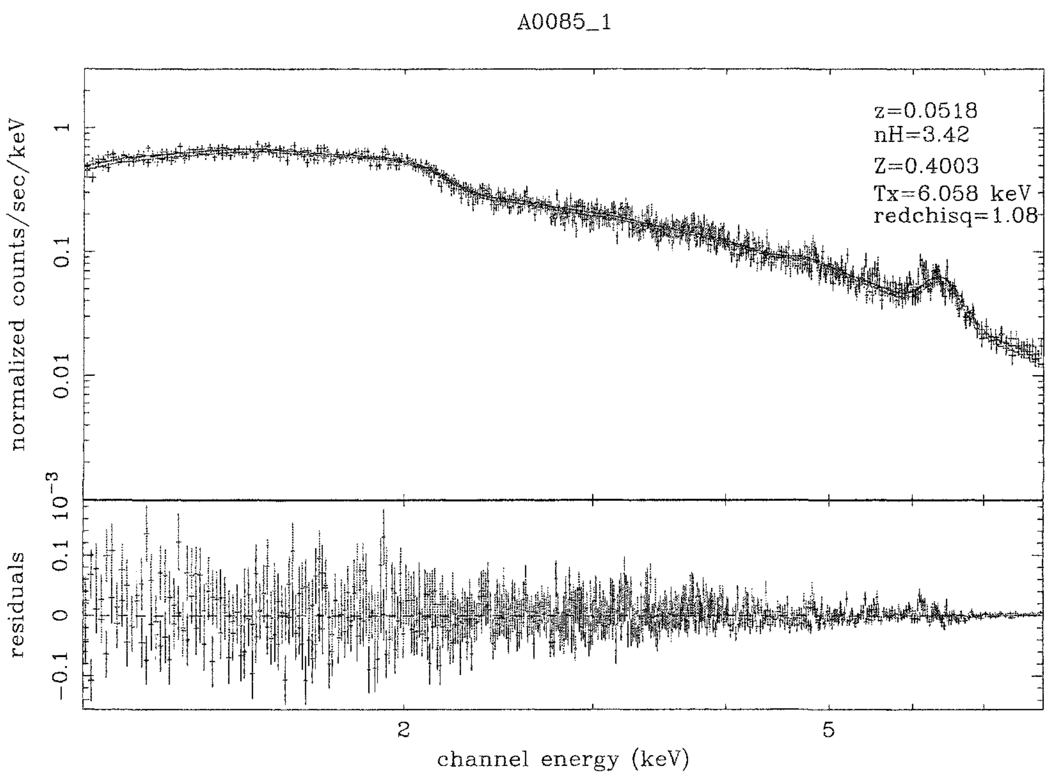

Figure 14 MEKAL model fit to the Spectra of Abell 85

CHAPTER 4

OBSERVATIONS AND DATA REDUCTION

In this chapter we describe the telescope and the instrumentation used to collect the optical data for a preliminary sample. The data reduction process is also described.

4.1 Observations

A sample of 16 galaxy clusters was observed with the MDM 1.3-m telescope at Kitt Peak National Observatory. The observations were made with a 2048×2048 CCD camera named Echelle. The camera is manufactured by Scientific Imaging Technologies (SITe). Each pixel is 24μm wide, making the CCD 49 mm ($2048 \times 24\mu$m) on the sides. The MDM 1.3-m telescope has a scale of $20.72''$/mm when used at $f/7.6$ and $11.81''$/mm when used at $f/13.5$. Since the clusters of galaxies are wide objects the telescope was setup to give us $20.72''$/mm which translates to a field of view of $17'$ (49 mm $\times$ $20.72''$) for our observations.

The observations were made on seven nights starting on May 3, 2000. Three nights (May 3, 4 and 9) were photometric while others where partly cloudy. During each clear night Landolt standard stars were observed throughout the night (Landolt 1992). Divided into these three clear nights, all the clusters in the sample were observed with short exposure time of one minute. This was done so that we could calibrate the short exposure images using the standard stars. The short exposures could then be used to calibrate the long exposure images recorded on non-photometric nights.

The number of frames required to image the clusters was determined based on the apparent sizes of the clusters. The apparent size depends on the distance of the cluster and the cosmology used.

The apparent angular size θ radians of an object of size y Mpc with a redshift of z is given by using $\theta = y/r$ with the angular size distance r being

$$r \simeq (1+z)^{-1} \frac{c}{H_0} \left(z - \frac{1+q_0}{2} z^2 \right),$$

where H_0 is the Hubble constant in Km/s/Mpc, c is the speed of light in vacuum in units of Km/s, $q_0 = 0.5\Lambda_m - \Lambda_k$. Λ_m and Λ_k are the density parameters (Peacock 1999).

For $z = 0.16$ the Abell diameter has an apparent size of $17'$ (field of view of our telescope) for $H_0 = 75$ Km/s/Mpc.

Clusters with higher redshifts ($z > 0.16$) have smaller angular sizes than the field of view of $17'$; therefore, a single exposure on the cluster center contains whole cluster. Such a distant cluster has to be imaged for a longer exposure time for us to have a high enough signal/ratio to capture faint galaxies. High redshift clusters were imaged for 45 minutes. To ensure quality of the images this exposure time was broken down into three 15 minute exposures and each 15 minute exposure image was checked before the next image was taken. The images were shifted slightly ($20''$) with respect to each other. This technique, known as dithering, takes away any inhomogeneity due to the dust particles on the mirror, bad pixels, or differences in pixel sensitivity that could exist in individual images from the final combined image.

For clusters with low redshift ($z < 0.16$) the apparent sizes are bigger than the field of view of the telescope. Different parts of such clusters had to be imaged individually in order to capture the whole clusters. These images formed mosaics

of 2×2 to 4×4 depending on the distances, hence the sizes of the clusters. The constituent images of the mosaics were taken in such a way that they overlapped the adjacent images. This was to ensure that we could digitally attach them without any loss of data. Since the the clusters with low redshift are nearby, a relatively short exposure time is enough to get high signal/noise for faint galaxies. Exposure time of 5 minutes was used to image each constituent field of the low redshift ($z < 0.16$) clusters.

The exposure times were determined by the distance of the clusters. To generate meaningful luminosity functions, it is required that we capture galaxies at least one magnitude fainter than M^* for the clusters as explained in chapter 2. Our exposure times were chosen to give us high signal to noise ratio for galaxies at least one magnitude fainter than M^*.

The clusters were observed with the R band filter with its central wavelength at 6300Åwith a full width half maximum of 1180Å. Figure 15 shows the response curve for this filter. The reason for observing in the R band filter is that the majority of the population in the galaxy clusters are elliptical galaxies which are red and therefore observing them in the R band gets us the most amount of light allowing us to observe galaxies with fainter magnitudes.

A set of calibration images was recorded along with the data. There is a zero (or bias) exposure current that goes through the CCD camera every time the camera is triggered. This needs to be taken out from the images. Since this current could vary each night, several zero exposure images were taken each night. The images also have a common non-uniformity in them due to the spatial variations in the CCD's sensitivity and the dust on the telescope optics. This non-uniformity can be characterized by observing uniform objects such as twilight sky. Such frames are called the flat fields. Division of the images by these flat fields removes the non-

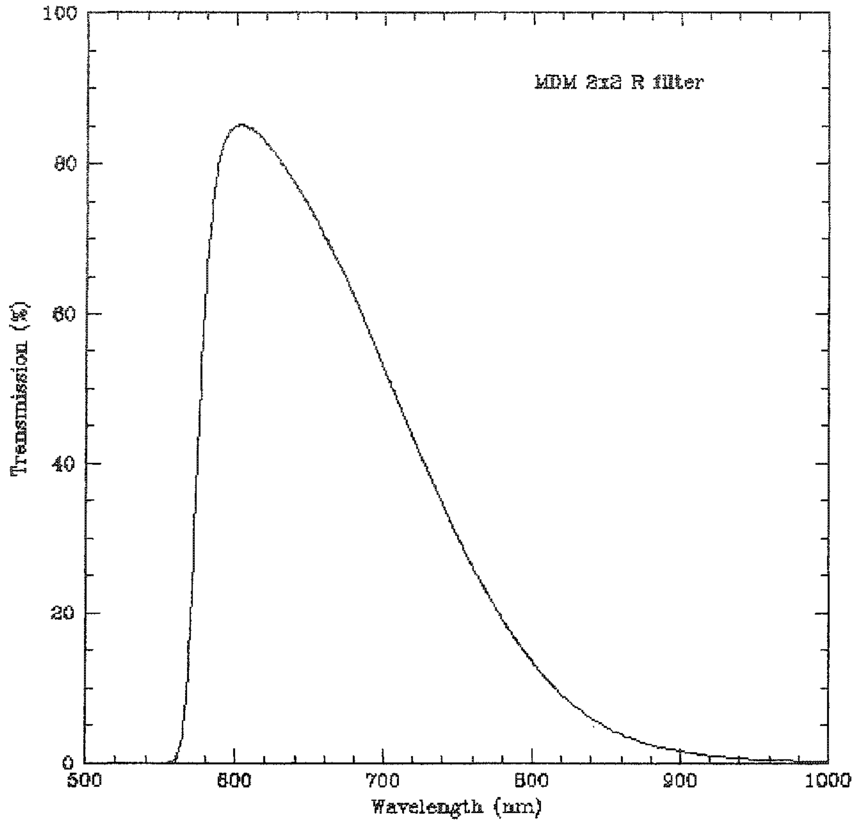

Figure 15 MDM Harris R Filter

uniformity. In order to be able to do this, several flat fields were observed at evening twilights and the morning twilights. The reasons for multiple flat field observations was to be able to average out the variations in them.

4.2 Data Reduction

The data were reduced using standard IRAF (Image Reduction and Analysis Facility) tasks. The zero and flat field frames for each night were combined by averaging them using the IRAF tasks ZEROCOMBINE and FLATCOMBINE. Some of the CCD pixels were not usable. A bad pixel file containing the coordinates of

pixels that were bad in the CCD was used to interpolate the values of the bad pixels using the adjacent pixel values. The CCD images also include a section in the image called the overscan section. The overscan section is the section of the CCD that is not exposed to the light and contains counts that would be part of the whole image. These counts need to be removed from the images, and overscan sections need to be trimmed out from the images. The images were corrected for zero, flats, bad pixels and overscan using the IRAF task CCDPROC.

CHAPTER 5

CALIBRATION

In this chapter we discuss processing of the reduced data, described in chapter 4, and calibration of the images using the standard stars.

5.1 Creating Mosaics

Since the area of our clusters on the sky could not be covered by one CCD exposure we created mosaics by joining several CCD images. To create a single image for a cluster, individual images were combined using the overlap regions. One of the images in the set was chosen as a reference image. For rest of the images, horizontal and vertical shifts in the pixels were computed using common stars in the overlap regions. All the images of the set were then combined, using the IMCOMBINE task of IRAF, forming one image for the whole cluster. Multiple single field images, which were dithered, for high redshift clusters were also combined with the IMCOMINE task. The only difference was that the shifts where small ($20''$) compared to the images that were mosaiced.

5.2 Cluster Centers and The Equatorial Grid

In order to generate a luminosity function for a given cluster one has to select galaxies within a region large enough to include most of member galaxies. A region with an Abell radius (1.5 Mpc) contains most of the cluster galaxies. Knowing the centers for the clusters is crucial for determining the location of this region. The centers of the clusters are also found to be the hottest regions of the clusters. Such

regions are $\sim 10^7 - 10^8$ K and radiate in X-rays. The centers were found by using intensity (I) weighted moments on the SIS x-ray images, available through the ASCA archives. SIS images were chosen for this task because they have better spatial resolution than GIS images and provide better accuracy for center coordinates. The x and y coordinates of the centers in the units for Right Ascension (RA) and Declination (DEC) are given by:

$$x_c = \frac{\sum_x \sum_y I(x,y)x}{\sum_x \sum_y I(x,y)}; \quad y_c = \frac{\sum_x \sum_y I(x,y)y}{\sum_x \sum_y I(x,y)}.$$

Locating these points on the CCD images requires mapping of the RA and DEC grid on the images. This was done using the United States National Observatory (USNO) sky survey. The survey includes astrometry of the entire sky and can be used to find the RA and DEC for bright stars in any field. The fields of our CCD images were matched with the USNO fields to find the equatorial coordinates using sets of five stars, four close to the corners and one close to the center. An IRAF coordinate transformation task, CCMAP, was used to map the equatorial grid on the CCD images using the physical (in units of pixels) and equatorial coordinates of the set of stars.

5.3 Calibration Using Standard Stars

On each of the three clear nights, Landolt (1992) standard stars were observed. These stars were used to calibrate the short exposure images of the clusters on those clear nights. An IRAF task, PHOT, was used to find the instrumental magnitudes of the standard stars. The true apparent magnitudes for these stars were looked up in the Landolt catalog. The relation between the instrumental magnitudes and the apparent magnitudes is based on the colors and the airmasses of the objects. The R band apparent magnitude, R, is given by,

$$R = M_r - R_1 - R_2\,X_r - R_3\,(V-R) - R_4\,(V-R)\,X_r$$

where R is the apparent magnitude, M_r is the instrumental magnitude, X_r is the airmass, $V-R$ is the $V-R$ color index, and R_1, R_2, R_3 and R_4 are constants. $R_4(V-R)X_r$ term is negligible and therefore R_4 is assumed to be zero. The instrumental magnitudes of the standard stars were found by using the IRAF task PHOT. To find the values for the constants, two separate catalogs were made, one containing the instrumental magnitudes with errors and the airmasses for the standard stars, and one containing the Landolt magnitudes and $(V-R)$ of the same standard stars. The constants were computed using these catalogs and the IRAF package PHOTCAL for each photometric night. The values for the constants are shown in Table 3.

Table 3 Constants for the transformation equation

Night of	R_1	R_2	R_3
May 3	2.508 ± 0.018	0.123 ± 0.011	0.061 ± 0.013
May 4	2.385 ± 0.105	0.187 ± 0.057	0.139 ± 0.090
May 9	2.578 ± 0.038	0.097 ± 0.027	0.024 ± 0.024

The transformation equations with the constants above were used to find the apparent magnitudes for the bright stars in the short exposure images taken on the clear nights. These brights stars are used to calibrate the long exposure images taken on the nights that were not photometric. All our observations were made using the R band filter which restricts us from using the R_3 $(V-R)$ term in our transformation equations for the bright stars. This terms affects the 100th place in the magnitude adding an error of less than a percent of a magnitude. We thus set R_3 to zero for calibrating the bright stars for the photometric nights. The apparent magnitudes, calculated by this method, were used on the non-photometric nights to

find a zero point for the images taken on those nights.

CHAPTER 6

PHOTOMETRY

In this chapter we discuss the photometry of the data that is reduced and calibrated as discussed in chapter 3 and 4. We also discuss how the star/galaxy classification is done.

6.1 Star-Galaxy Classification and Photometry Using SExtractor

The photometry done so far is on selected bright stars for calibration and is done using the IRAF task PHOT. Photometry done by PHOT requires lists of coordinates for the sets of objects on which the photometry is to be done. In order to create such lists for cluster galaxies, the stars and galaxies in the images have to be separated. PHOT also does photometry using fixed circular aperture. For better results, the aperture for galaxies should be varied based on the angular sizes and shapes of the galaxies. Since the clusters in our sample are rich clusters of galaxies, de-blending is also required for high density regions before performing photometry. SExtractor (Source Extractor), software written for such tasks, optimally detects, deblends, measures and classifies sources from images (Bertin & Arnouts, 1995). SExtractor analyzes the images in six steps: estimation of the sky background, detection, deblending, filtering of the detection, photometry and star/galaxy separation. This process is ideal for our project.

The background is estimated by clipping the local background histogram iteratively until it converges at $\pm 3\sigma$ around its median, and recording the mean of the clipped histogram as the local background. If σ changes by more than 20% during

the clipping process, the field is considered crowded and the mode of the histogram is recorded as the background. A background grid is generated using this process for the whole image.

After the background is generated, the objects are detected using a technique called thresholding. 8-connected contiguous pixels above a threshold value from the background, are extracted by convolving a Point Spread Function with them. This is done using Lutz's one pass algorithm (Lutz, 1979)

Deblending is done by re-thresholding at 30 different levels between primary extraction threshold and its peak value. If a branch of multiple sets of connected pixels is detected above a level and if the integrated pixel intensity (above the level) of the branch is greater than a certain fraction of the total intensity of the composite object, the object is consider a blend of multiple objects.

When dealing with extended sources like galaxies, it is possible that one could erroneously detect separate objects for peaks in the wings of such sources. SExtractor computes the contribution to the mean surface brightness of each object from its neighbors. This contribution is then subtracted, and if the mean surface brightness still falls above the detection threshold, the object is accepted as a separate object.

For each object SExtractor computes 2 types of magnitudes, one uses the adaptive aperture, and the other an isophotal correction. For each object, adaptive aperture method computes an elliptical aperture with ellipticity ϵ, position angle θ and size $6\sigma_i so$, where $\sigma_i so$ is the mean standard deviation of the bivariate Gaussian profile of the object. The counts in this aperture are integrated to compute the magnitude.

SExtractor uses the adaptive aperture magnitudes to catalog the objects unless a neighbor is suspected to bias the magnitude by more than 0.1 magnitude. In such cases the corrected isophotal magnitude is used.

Star/galaxy classification is done by SExtractor using a neural network. The assumption that the galaxy images look more extended than stars or QSO's is the basis of the neural network used by SExtractor. The parameters are 8 isophotal areas, 1 peak intensity, and the seeing which is entered by the user. The isophotal areas are in the units of the "squared seeing (FWHM)". The output contains of a "stellarity index':" 0 for a galaxy, 1 for a star, or any intermediate value for ambiguous objects.

SExtractor is used for doing photometry on all the clusters we observed at the MDM observatory. Since seeing is one of the most important parameters used by the star/galaxy classifier used by SExtractor, great care was taken in computing the seeing for individual images. The objects with the stellar index less then 0.2 were confirmed by eye to be galaxies using multiple images. For each cluster, right ascensions and declinations of all the objects with their stellar index less than 0.2, and R band magnitudes measured by SExtractor with their measurement errors were tabulated.

CHAPTER 7

ARCHIVE DATA

In this chapter we discuss the Automatic Plate Measuring (APM) and Sloan Digital Sky Survey (SDSS) archives used to obtain data to supplement the CCD observations. The archives contain photometric data and include star/galaxy classification for the objects.

7.1 Automatic Plate Measuring (APM) Catalog

The Automatic Plate Measuring (APM) machine (Figure 16) is a National Astronomy Facility run by the Institute of Astronomy in Cambridge. The APM facility typically processes a data stream of well over 10 Gbytes per day from which the parameters of about 1 million images are extracted. The facility has digitized the first generation of The National Geographic Society-Palomar Observatory Sky Survey (POSS1) to 20 degrees from the Galactic plane and southern UK Schmidt Telescope (UKST) survey to 30 degrees from the Galactic plane with a few missing parts. Although, a large part of the service provided by this facility consists of off-line data processing, POSS1 and UKST data have been made available on-line which include photometry of the objects. Position and photometry data for 83 Abell clusters were obtained from the APM site. Figure 17 and 18 show the POSS1 and UKST coverage. The white regions are the regions of the galactic plane and are not covered by the surveys.

The APM system uses a fast laser microdensitometer with a dedicated hardware-based front end for signal preprocessing. Control of the hardware, communication

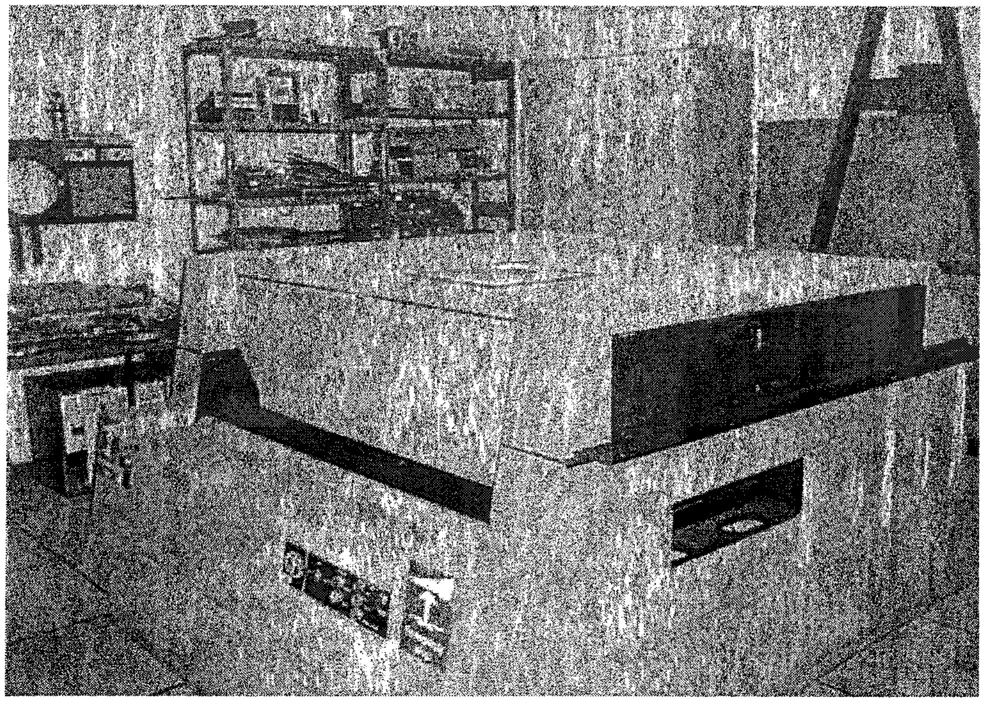

Figure 16 The Automatic Plate Measuring (APM) machine

with the microdensitometer, and data acquisition are done using a computer with an average transfer rate of 1 Mbyte/s. The signal conditioning hardware, programmable via the PC interface, performs 16-bit analog to digital conversion and look-up-table (LUT) transformations from transmission to density (or intensity), and digitally smears the spot if required. The computer controls the complete scanning system, forms the control interface for the user, and also carries out the image analysis. The high scanning speed is achieved by sweeping the laser beam across the plate in strips 2 mm wide using an acousto-optic deflector. A massive $x - y$ table is used to move the plate relative to the beam and a scan is built up by moving the table in the y direction with the x coordinate fixed. Subsequently the table is moved 2 mm in x and another y strip is measured. Each scan line within the 2 mm strip is digitized into 256 samples at 7μm spacing. The rms repeatability (expected deviation in the signal) is $\sim 0.5\mu$ for both axes. The scanning and processing time for a complete

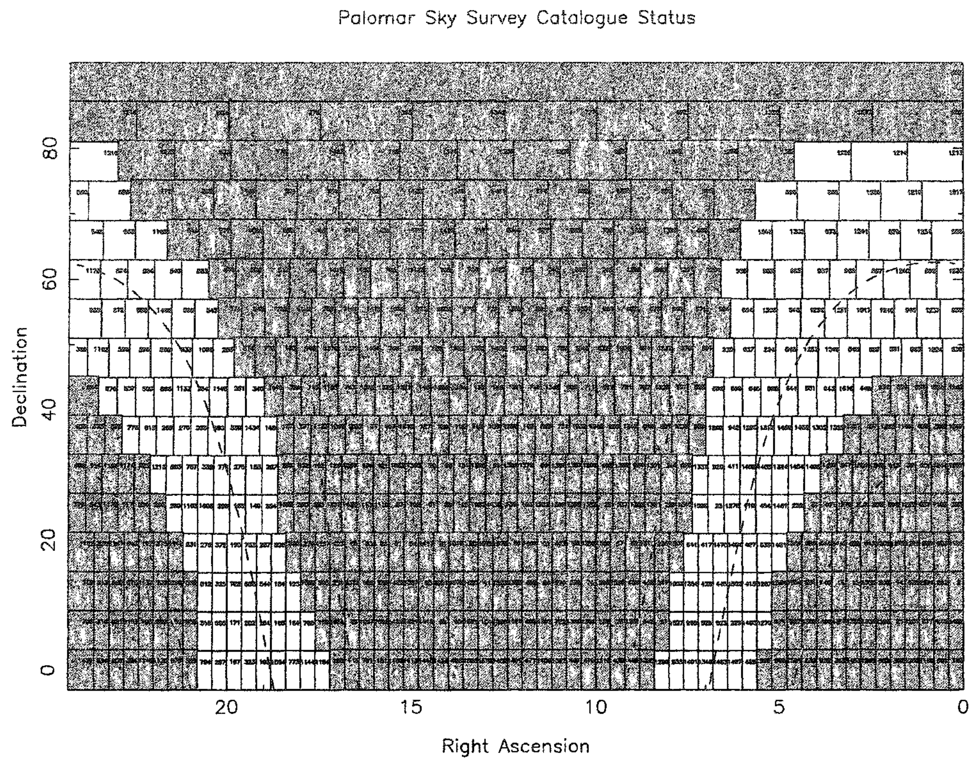

Figure 17 POSS1 Sky Coverage

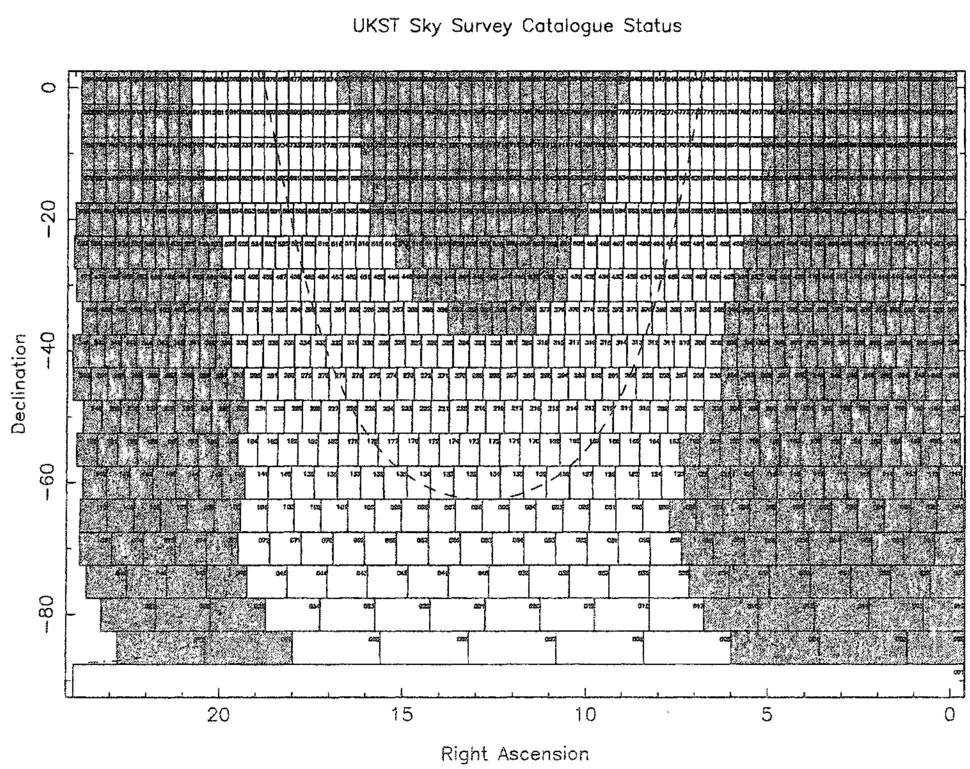

Figure 18 UKST Sky Coverage

UK or Palomar Schmidt plate at 0.5 arcsec resolution is just over 4 hours.

The majority of the APM objects have an internal position accuracy of approximately 0.1 arcsec except stars brighter than about 11^{th} magnitude and fully resolved galaxies. The external accuracy is about 0.5 arcsec and is governed by the density and magnitude range of the astrometric standards used, and is limited by residual plate distortions and magnitude-dependent terms.

The APM magnitudes are given as "red" and "blue" plate magnitudes. For UKST survey plates "blue" = Bj (i.e. 3900Å-5400Å bandpass) while "red" = OR (i.e. 5900Å-6900Å bandpass). For POSS1 survey plates "blue" = O (i.e. 3200Å-4900Å bandpass) while "red" = E (i.e. 6200Å- 6800Å bandpass). The magnitude limits of the commonly used plates to within 0.5 magnitude are: UKST/POSS2 Bj=22.5; UKST/POSS2 R=21.0; POSS1 E=20.0, POSS1 O=21.5. Internal accuracy for the majority of images brighter than 1 magnitude above the plate limit are typically 0.1 magnitude, with the same exceptions as in position accuracy. External accuracy is about 0.3 magnitudes for the fainter images but can be much worse than this (i.e. 1+ magnitudes) for bright images. This was a problem for this project as discussed in section 7.3.

7.2 Sloan Digital Sky Survey

The Sloan Digital Sky Survey (SDSS) is an ambitious astronomical survey that maps in detail one-quarter of the entire sky, determining the positions and magnitudes of more than 100 million objects. It also provides distance measurements to more than a million galaxies and quasars. Apache Point Observatory, site the of the SDSS telescopes, is operated by the Astrophysical Research Consortium (ARC).

SDSS is a joint project of The University of Chicago, Fermilab, the Institute for Advanced Study, the Japan Participation Group, The Johns Hopkins Univer-

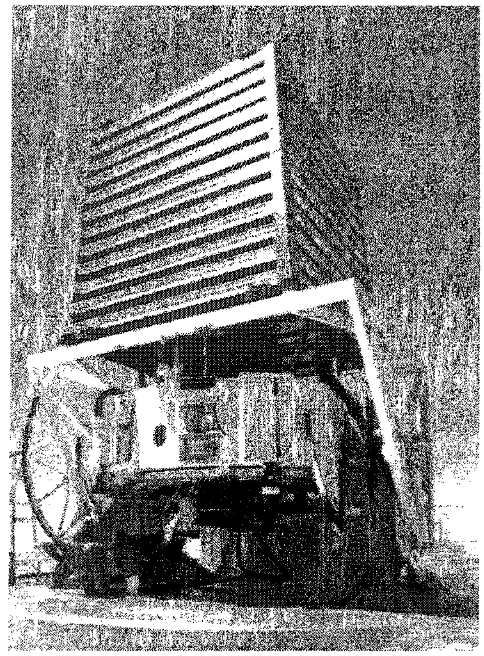

Figure 19 SDSS 2.5 Meter Telescope

sity, the Los Alamos National Laboratory, the Max-Planck-Institute for Astronomy (MPIA), the Max-Planck-Institute for Astrophysics (MPA), New Mexico State University, University of Pittsburgh, Princeton University, the United States Naval Observatory, and the University of Washington. The project is funded by the Alfred P. Sloan Foundation, the participating institutions, the National Aeronautics and Space Administration, the National Science Foundation, the U.S. Department of Energy, the Japanese Monbukagakusho, and the Max Planck Society.

The 2.5-meter Sloan telescope has a wide-angle view, and is it made specifically to create a map of the sky. The telescope uses CCD cameras and two spectrographs. Figure 19 shows the telescope pointing toward zenith. The boxy metal structure is the outer wind baffle, mounted separately from the rest of the telescope. The telescope scans the sky at the sidereal rate. As of October 2004, three data releases have been made public by SDSS that cover 5282 square degrees of the northern

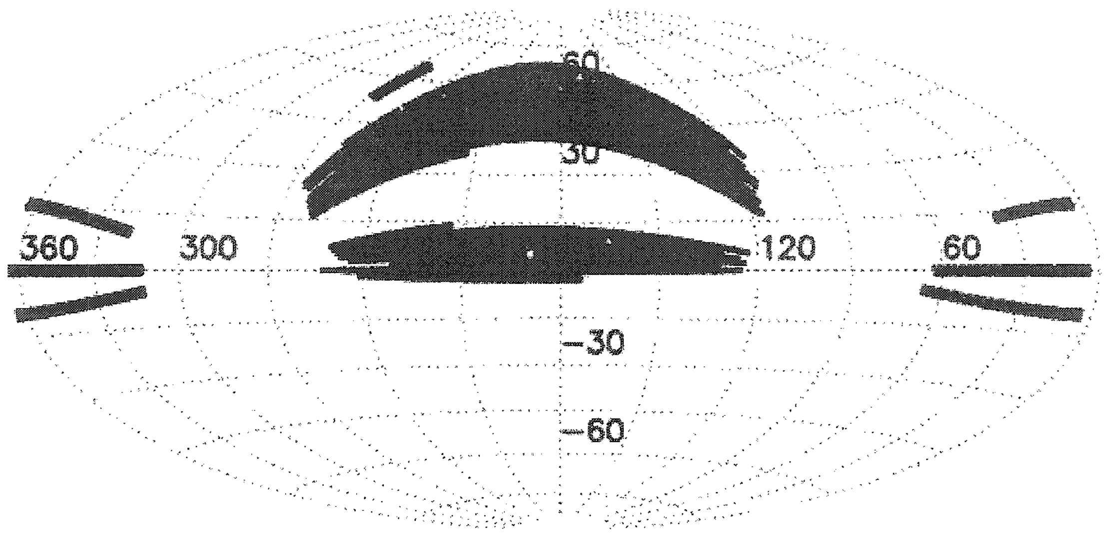

Figure 20 SDSS DR3 coverage

hemisphere. Figure 20 show the data release 3 (DR3) sky coverage of SDSS.

The filter system used by SDSS is summarized in Table 4.

Table 4 SDSS filters

Filter	λ_c	FWHM
u'	3540 Å	570 Å
g'	4770 Å	1370 Å
r'	6230 Å	1370 Å
i'	7630 Å	1530 Å
z'	9130 Å	950 Å

Figure 21 shows the SDSS filter system response curves. The responses are shown without atmospheric extinction (upper curves) and as modified by the extinction at 1.2 airmasses (lower curves). The curves represent expected total quantum efficiencies of the camera plus telescope on the sky.

The limiting magnitudes at the detection limit, S/N 5:1, is about $u' = 22.3$, $g' = 23.3$, $r' = 23.1$, $i' = 22.5$ and $z' = 20.8$. These limiting magnitudes are for

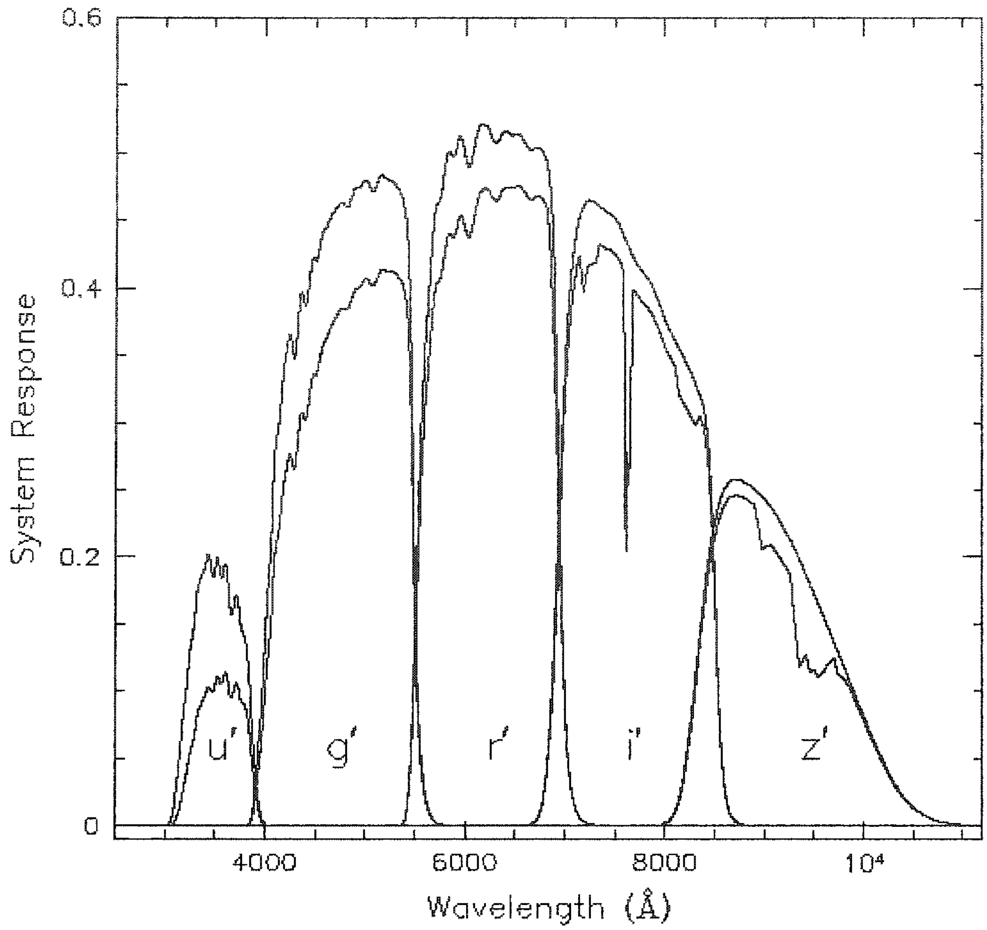

Figure 21 SDSS filter response

stars, and those for galaxies are typically between half a magnitude and a magnitude brighter at the same signal to noise ratio. We are concerned with the red magnitude, since most cluster galaxies are red, the limiting magnitude for the galaxies of interest is r'$\sim$ 22.

Figure 22 shows the completeness of SDSS in r' band as compared to the Classifying Objects by Medium-Band Observations (COMBO) survey. COMBO survey has imaged 1 square degree of sky in 17 filters using the Wide Field Imager at the MPG/ESO 2.2-m telescope at La Silla, Chile. The 17 passband allow classification into stars, galaxies and quasars to R < 24 (Wolf 2004).

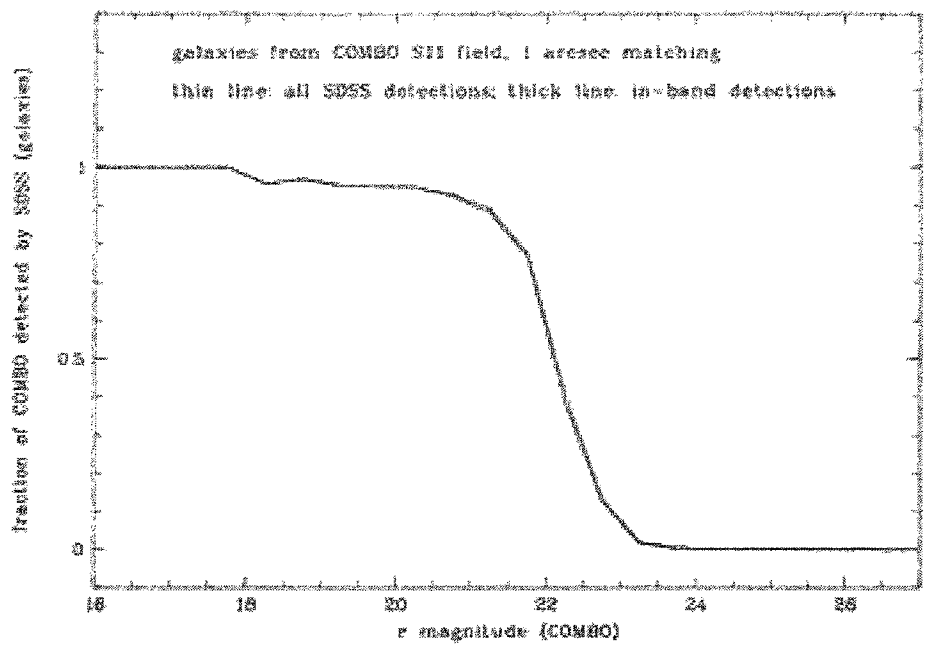

Figure 22 SDSS completeness for Galaxies in r band

7.3 Comparison of the APM, Sloan and MDM Samples

Sloan Digital Sky Survey (SDSS) is an all digital survey that is more recent and contains fainter objects than the digitized APM survey. We decided to compare the APM survey data with Sloan survey data to check the consistency of the photometry done in two different sets of data. The photometry of the sample observed at the MDM observatory is done using the software SExtractor which uses a method different than both APM catalog and SDSS, therefore, it is also important to compare the MDM results to APM catalog and SDSS for consistency checks.

As of October 2004, the APM catalog is still about 3 times (15000 degrees^2/5282 degrees^2) larger in survey area than SDSS, and contains all the clusters of our sample drawn from SDSS and the clusters observed at the MDM observatory. Therefore, the photometry of all the clusters of the samples drawn from SDSS and the clusters observed at the MDM observatory are compared with the APM sample. Five

common clusters between the SDSS and the MDM samples which are also compared.

In order to compare the photometry of individual clusters, a region of 0.2 Mpc from the cluster centers is chosen. In order to do this, the regions in arc-seconds corresponding to 0.2 Mpc are calculated from the center of each cluster using $\theta = 0.2/r$ with the angular size distance,

$$r \simeq (1+z)^{-1} \frac{c}{H_0} \left(z - \frac{1+q_0}{2} z^2 \right)$$

(Peacock 1999). All the galaxies with angular distance (ϕ) smaller than θ from the cluster center are kept. ϕ is determined using

$$\cos(\phi) = \sin(\delta_c)\sin(\delta) + \cos(\delta_c)\cos(\delta)\cos(\alpha_c - \alpha),$$

where α_c and δ_c are the center coordinates, and α and δ are the coordinates of the individual galaxies. Each galaxy in a cluster to be compared from the Sloan survey is used to look for a galaxy in the corresponding cluster from the APM survey within the distance of 2 arc-seconds, accounting for any position errors. Similarly, the clusters from the MDM sample are also compared with the APM survey. The same is done to compare common clusters between the Sloan and the MDM samples.

The following figures show the comparison done using the above method. Figures on the left show apparent magnitude verses apparent magnitude plots for the same galaxies from two different surveys. A line with a slope of 1 is plotted for reference on these plots. Figures on the right show the locations of the galaxies from two different surveys confirming that the same galaxies are being compared. Magnitudes from the APM data do not agree with SDSS data for bright galaxies. For some clusters (e.g. A2255) the data do not agree for most of the galaxies. Data from MDM are in strong agreement with SDSS. This makes the data from the APM survey unusable in generating luminosity functions.

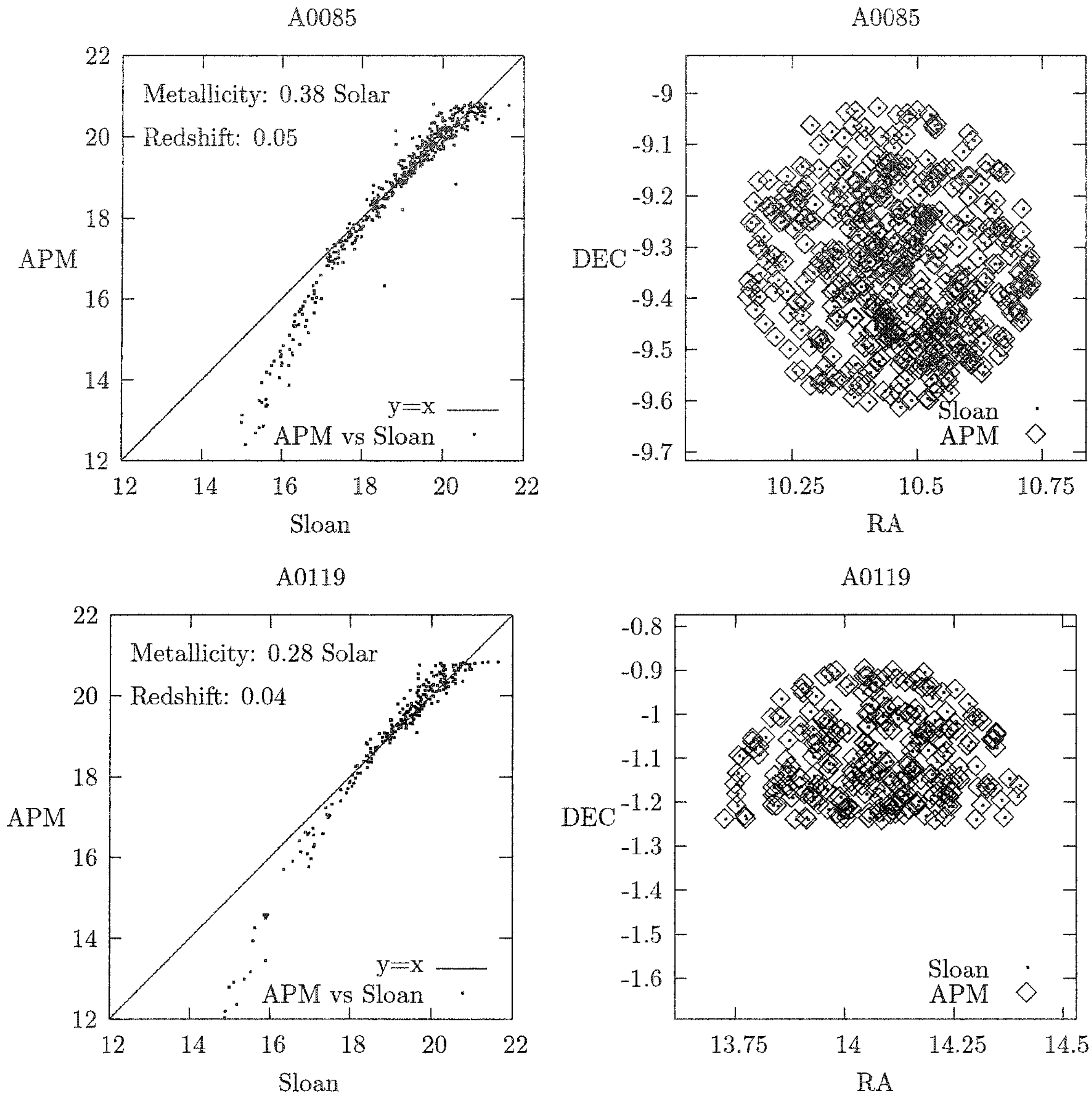
A0085
Metallicity: 0.38 Solar
Redshift: 0.05
y=x
APM vs Sloan
APM
Sloan
A0085
Sloan
APM
DEC
RA
A0119
Metallicity: 0.28 Solar
Redshift: 0.04
y=x
APM vs Sloan
APM
Sloan
A0119
Sloan
APM
DEC
RA

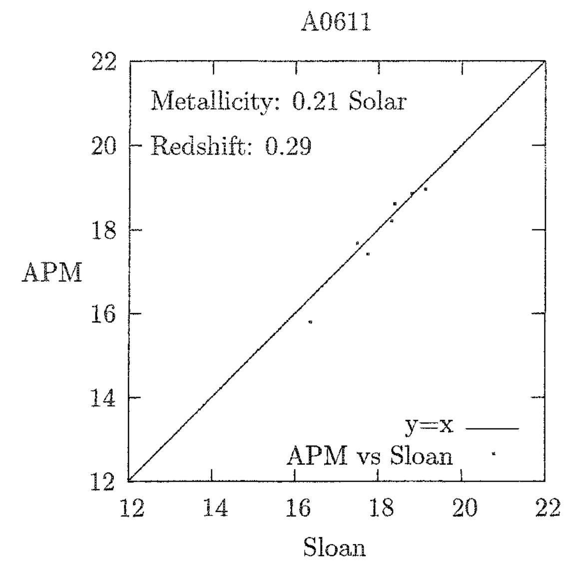
A0611
Metallicity: 0.21 Solar
Redshift: 0.29
APM
Sloan
y=x
APM vs Sloan
12
14
16
18
20
22

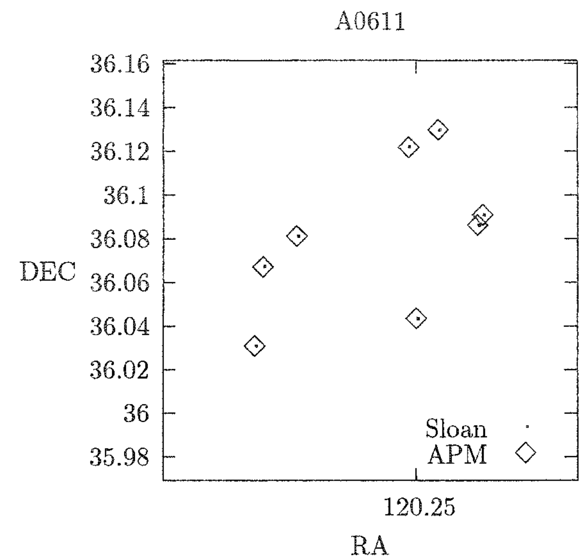
A0611
DEC
RA
36.16
36.14
36.12
36.1
36.08
36.06
36.04
36.02
36
35.98
120.25
Sloan
APM

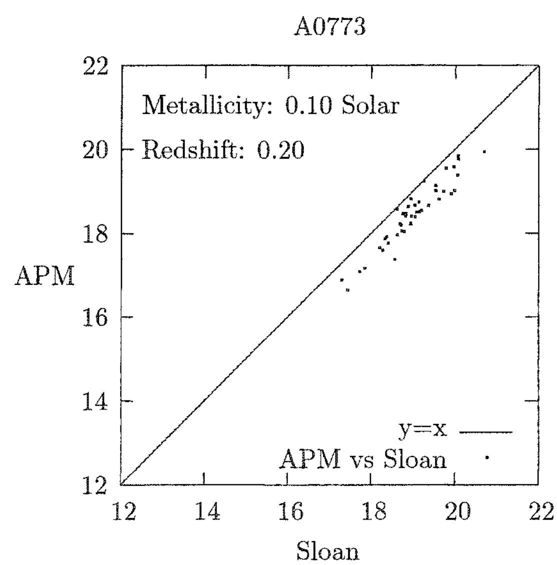
A0773
Metallicity: 0.10 Solar
Redshift: 0.20
APM
Sloan
y=x
APM vs Sloan
12
14
16
18
20
22

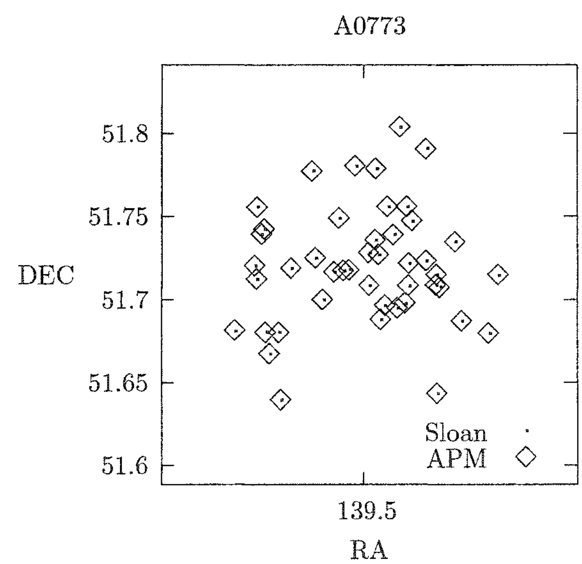
A0773
DEC
RA
51.8
51.75
51.7
51.65
51.6
139.5
Sloan
APM

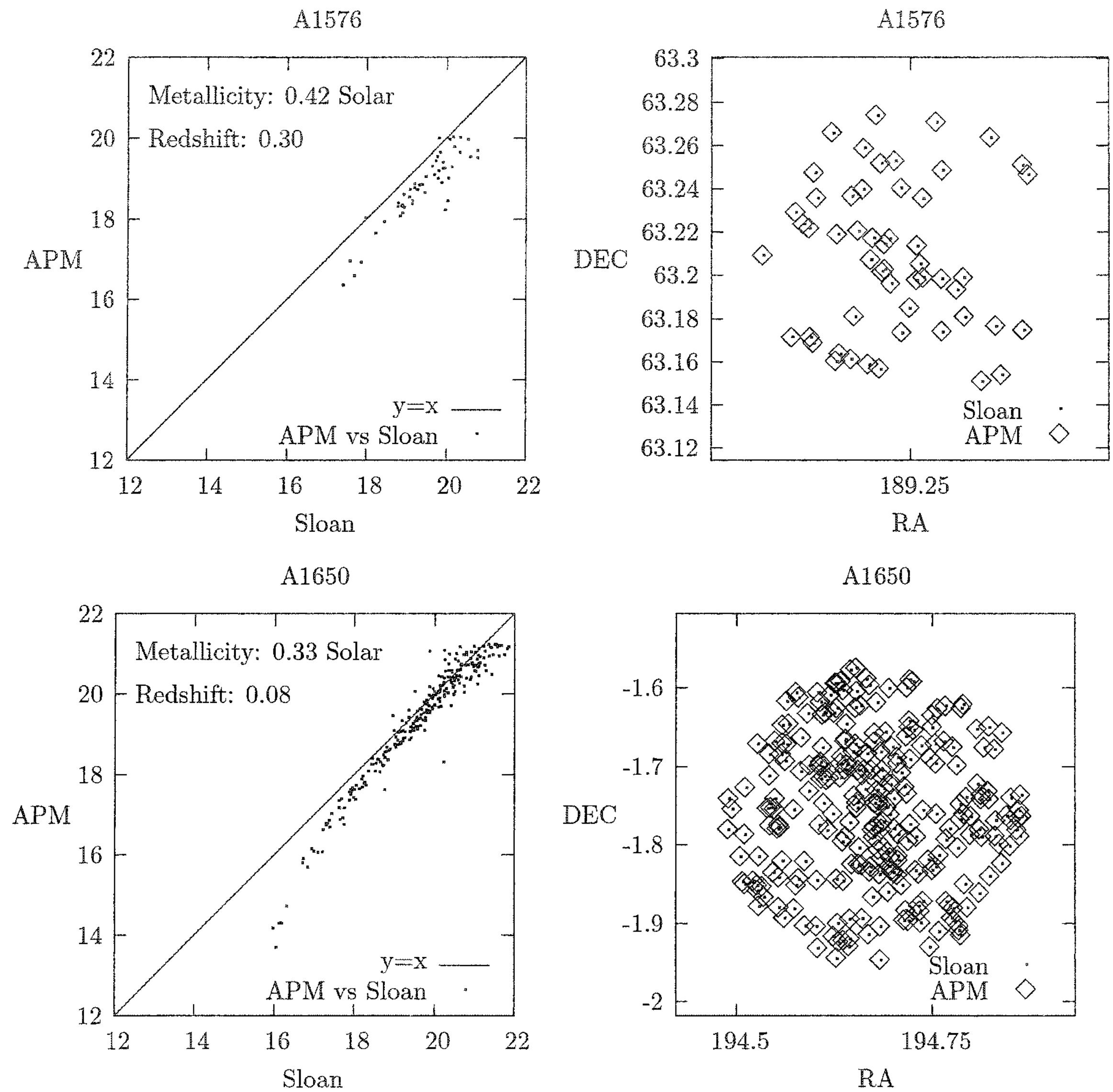
A1576
Metallicity: 0.42 Solar
Redshift: 0.30
y=x
APM vs Sloan
APM
Sloan
A1576
Sloan
APM
DEC
RA
189.25
A1650
Metallicity: 0.33 Solar
Redshift: 0.08
y=x
APM vs Sloan
APM
Sloan
A1650
Sloan
APM
DEC
RA
194.5
194.75

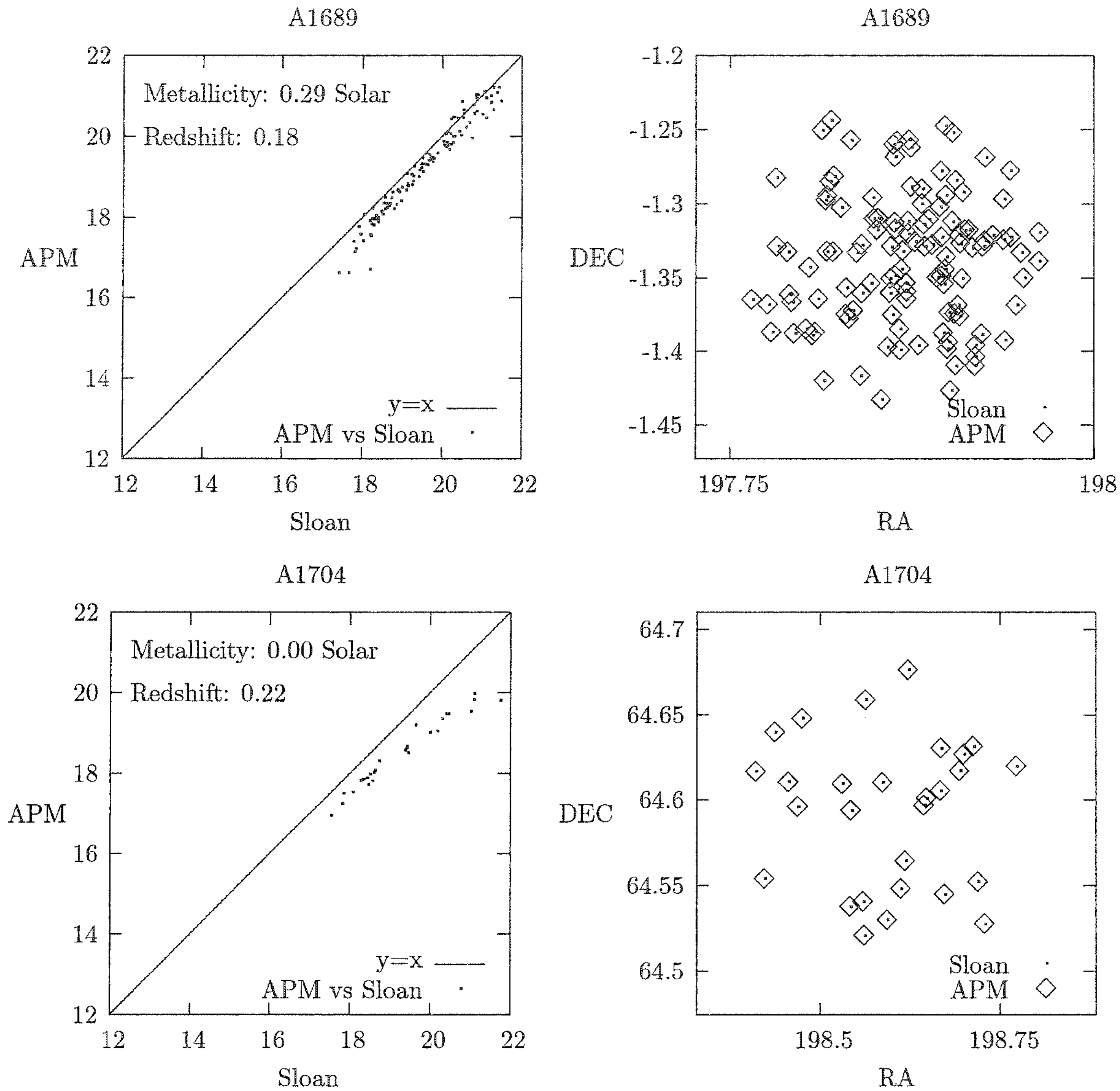
A1689
Metallicity: 0.29 Solar
Redshift: 0.18
y=x
APM vs Sloan
APM
Sloan
A1689
Sloan
APM
DEC
RA
A1704
Metallicity: 0.00 Solar
Redshift: 0.22
y=x
APM vs Sloan
APM
Sloan
A1704
Sloan
APM
DEC
RA

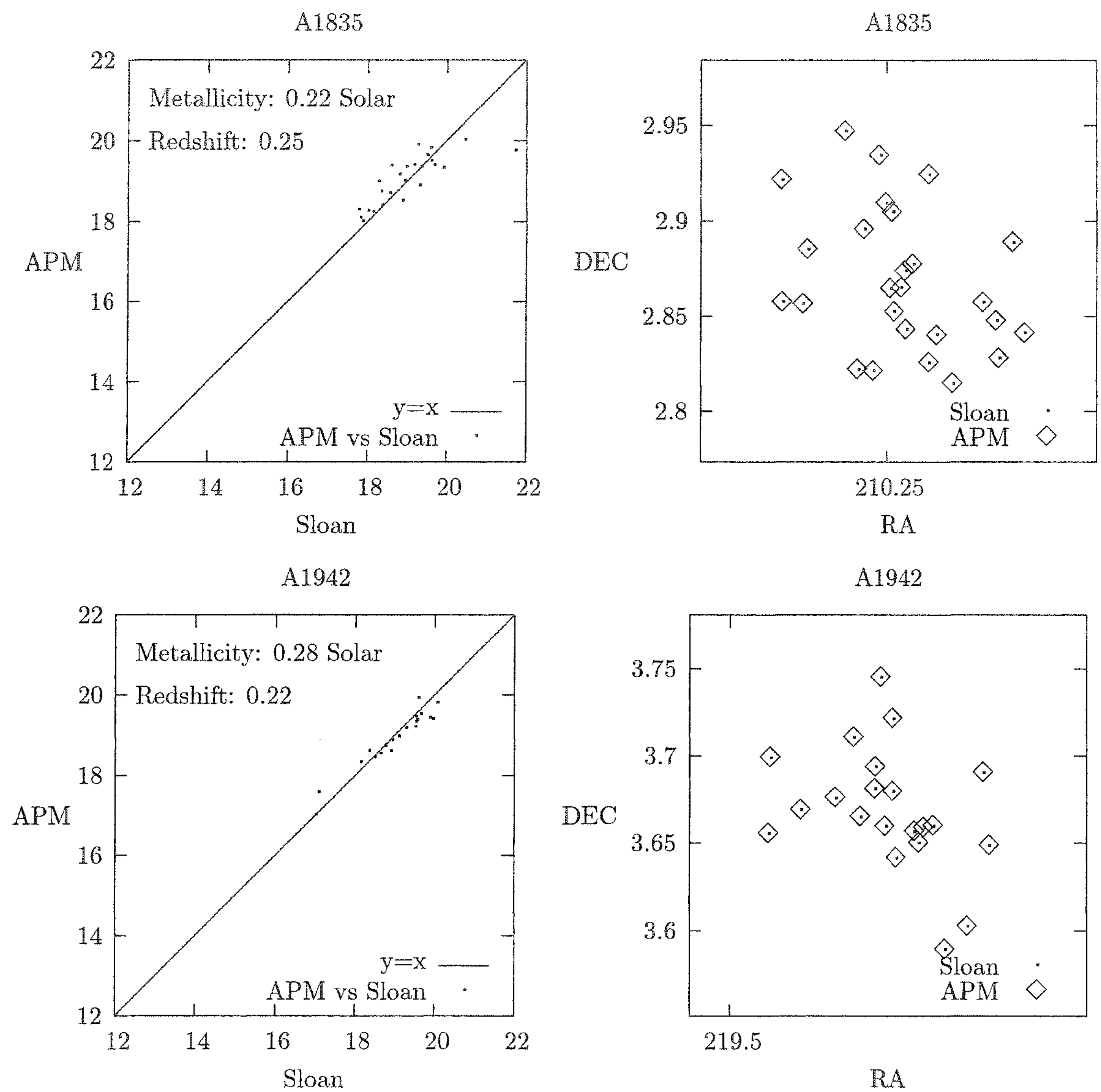
A1835
Metallicity: 0.22 Solar
Redshift: 0.25
APM
Sloan
y=x
APM vs Sloan
A1835
DEC
RA
210.25
Sloan
APM
A1942
Metallicity: 0.28 Solar
Redshift: 0.22
APM
Sloan
y=x
APM vs Sloan
A1942
DEC
RA
219.5
Sloan
APM

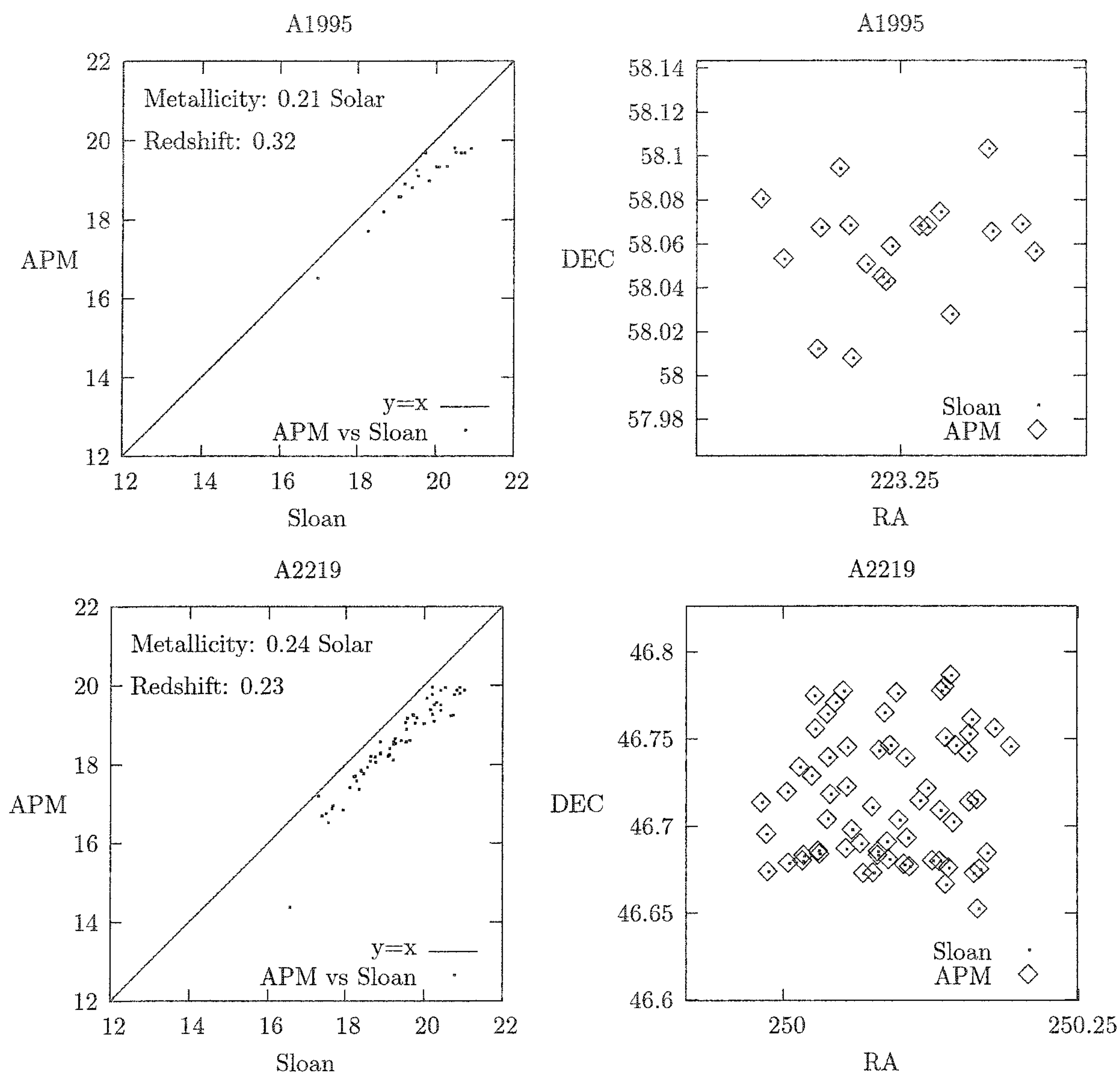

A1995
Metallicity: 0.21 Solar
Redshift: 0.32
APM
Sloan
y=x
APM vs Sloan
A1995
DEC
RA
223.25
Sloan
APM
A2219
Metallicity: 0.24 Solar
Redshift: 0.23
APM
Sloan
y=x
APM vs Sloan
A2219
DEC
RA
250
250.25
Sloan
APM

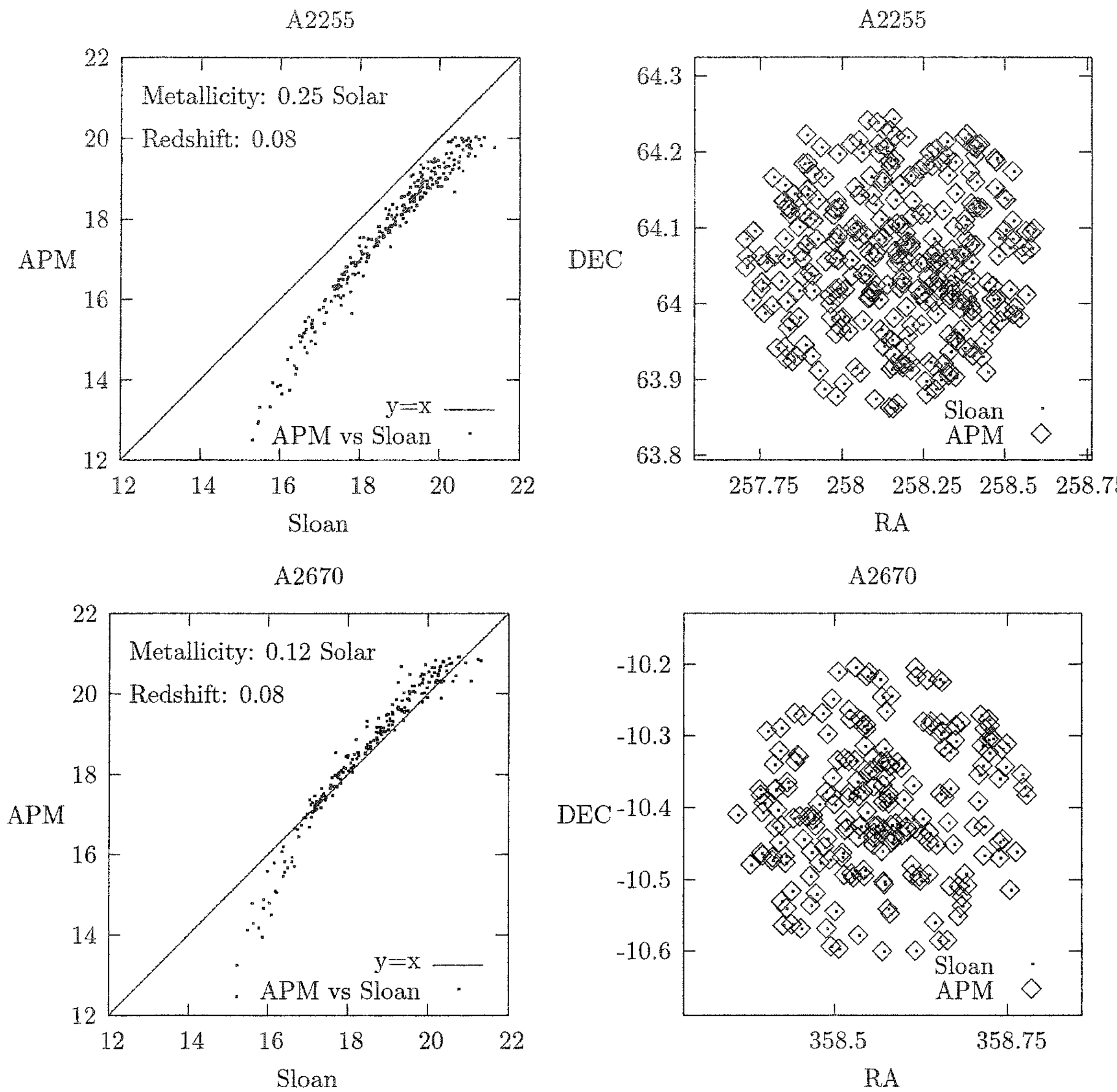
A2255
Metallicity: 0.25 Solar
Redshift: 0.08
APM
Sloan
y=x
APM vs Sloan
A2255
DEC
RA
Sloan
APM
A2670
Metallicity: 0.12 Solar
Redshift: 0.08
APM
Sloan
y=x
APM vs Sloan
A2670
DEC
RA
Sloan
APM

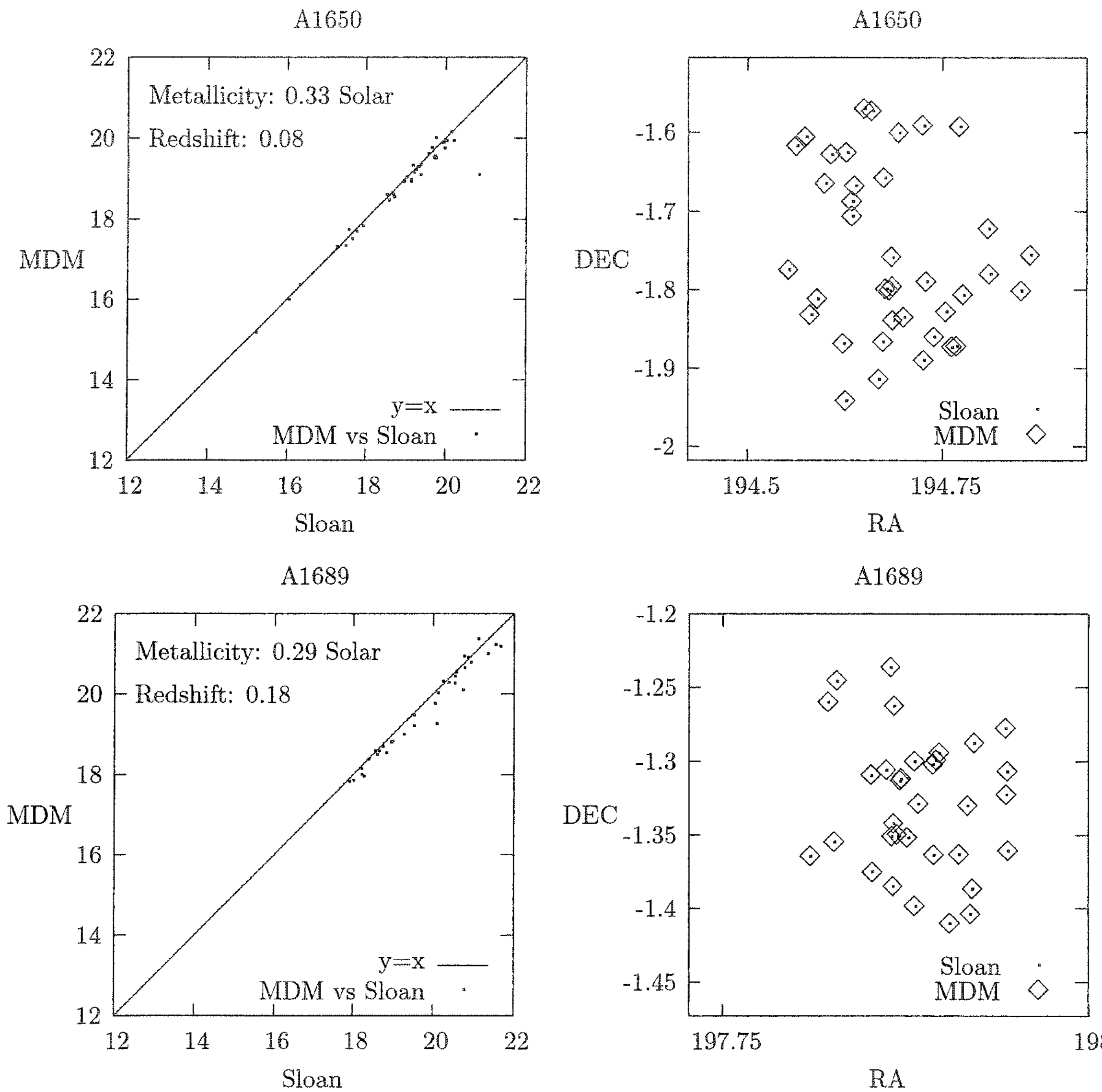
A1650
Metallicity: 0.33 Solar
Redshift: 0.08
y=x
MDM vs Sloan
MDM
Sloan
A1650
DEC
RA
Sloan
MDM
A1689
Metallicity: 0.29 Solar
Redshift: 0.18
y=x
MDM vs Sloan
MDM
Sloan
A1689
DEC
RA
Sloan
MDM

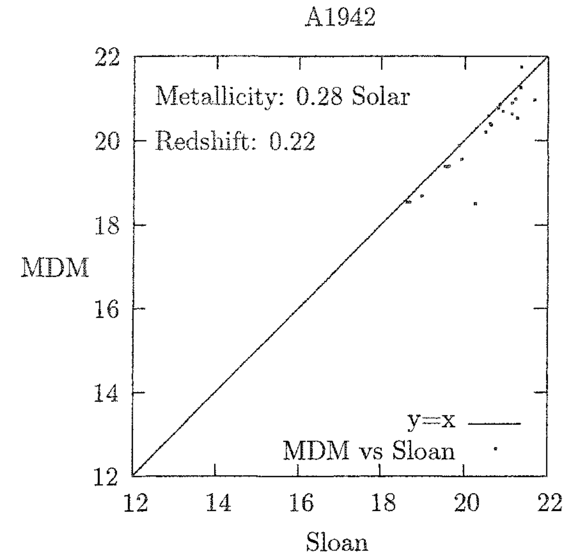
A1942
Metallicity: 0.28 Solar
Redshift: 0.22
MDM
Sloan
y=x
MDM vs Sloan
12
14
16
18
20
22

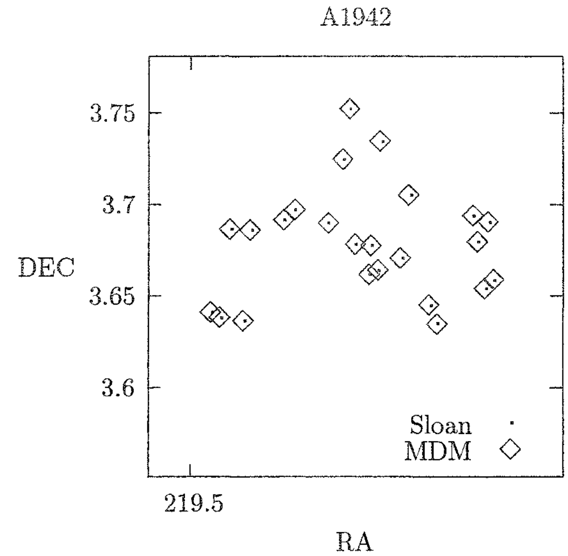
A1942
DEC
RA
3.75
3.7
3.65
3.6
219.5
Sloan
MDM

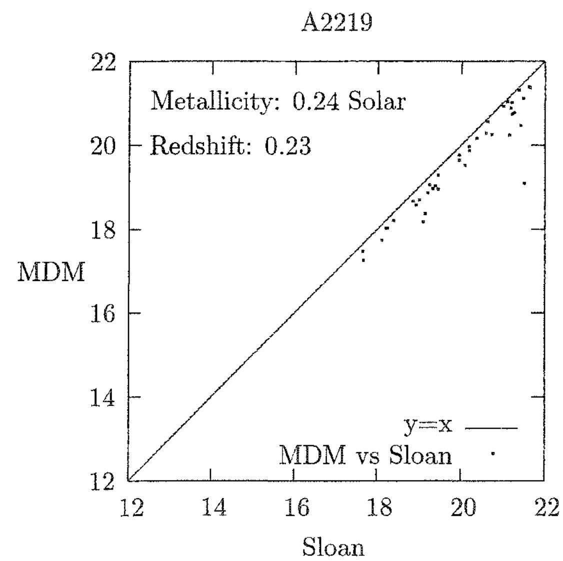
A2219
Metallicity: 0.24 Solar
Redshift: 0.23
MDM
Sloan
y=x
MDM vs Sloan
12
14
16
18
20
22

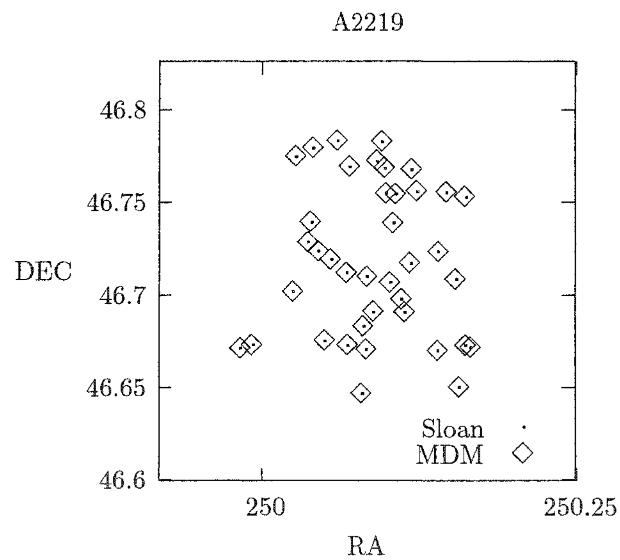
A2219
DEC
RA
46.8
46.75
46.7
46.65
46.6
250
250.25
Sloan
MDM

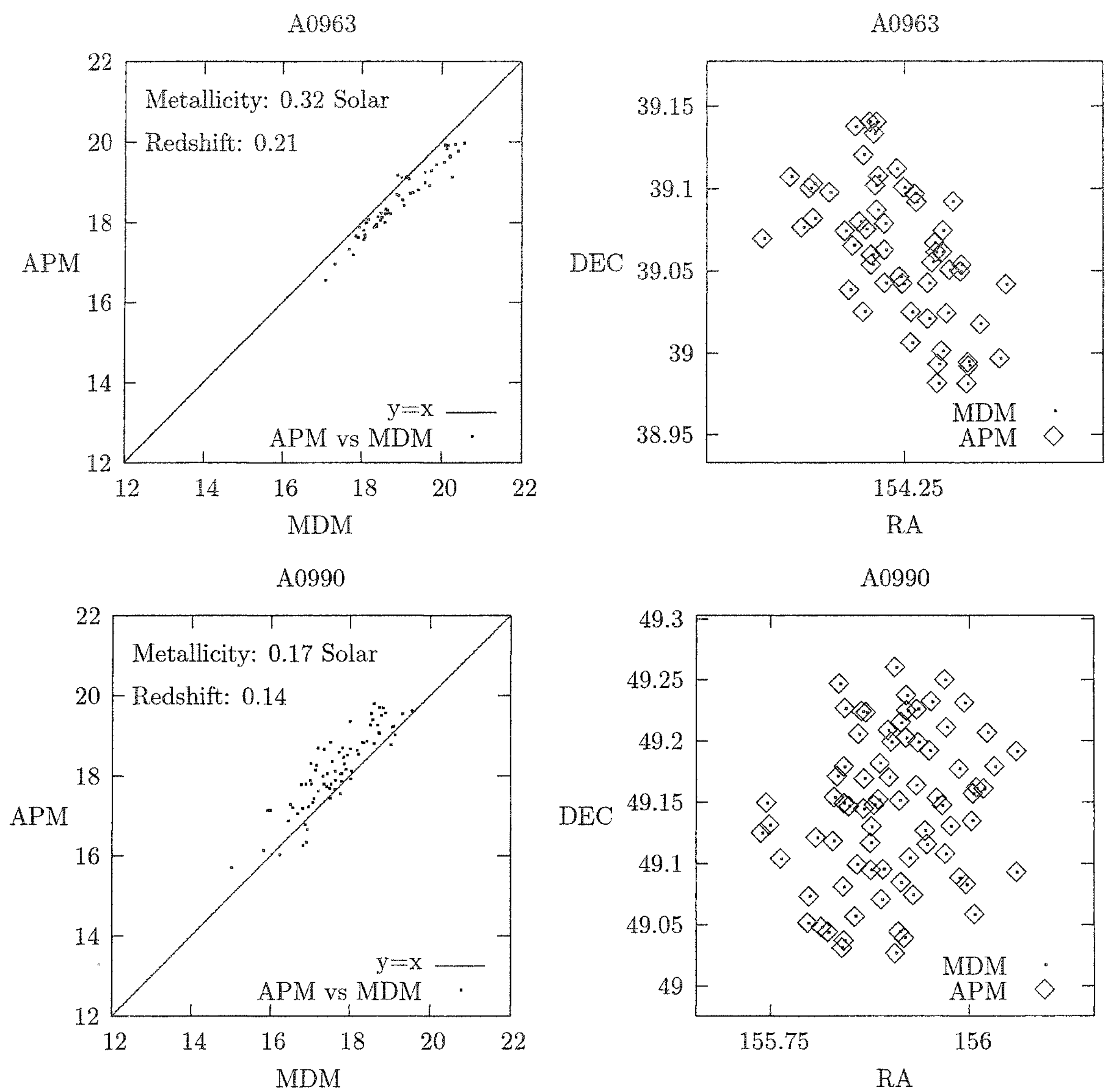
A0963
Metallicity: 0.32 Solar
Redshift: 0.21
y=x
APM vs MDM
APM
MDM
12
14
16
18
20
22
A0963
DEC
RA
39.15
39.1
39.05
39
38.95
154.25
MDM
APM
A0990
Metallicity: 0.17 Solar
Redshift: 0.14
y=x
APM vs MDM
APM
MDM
A0990
DEC
RA
49.3
49.25
49.2
49.15
49.1
49.05
49
155.75
156

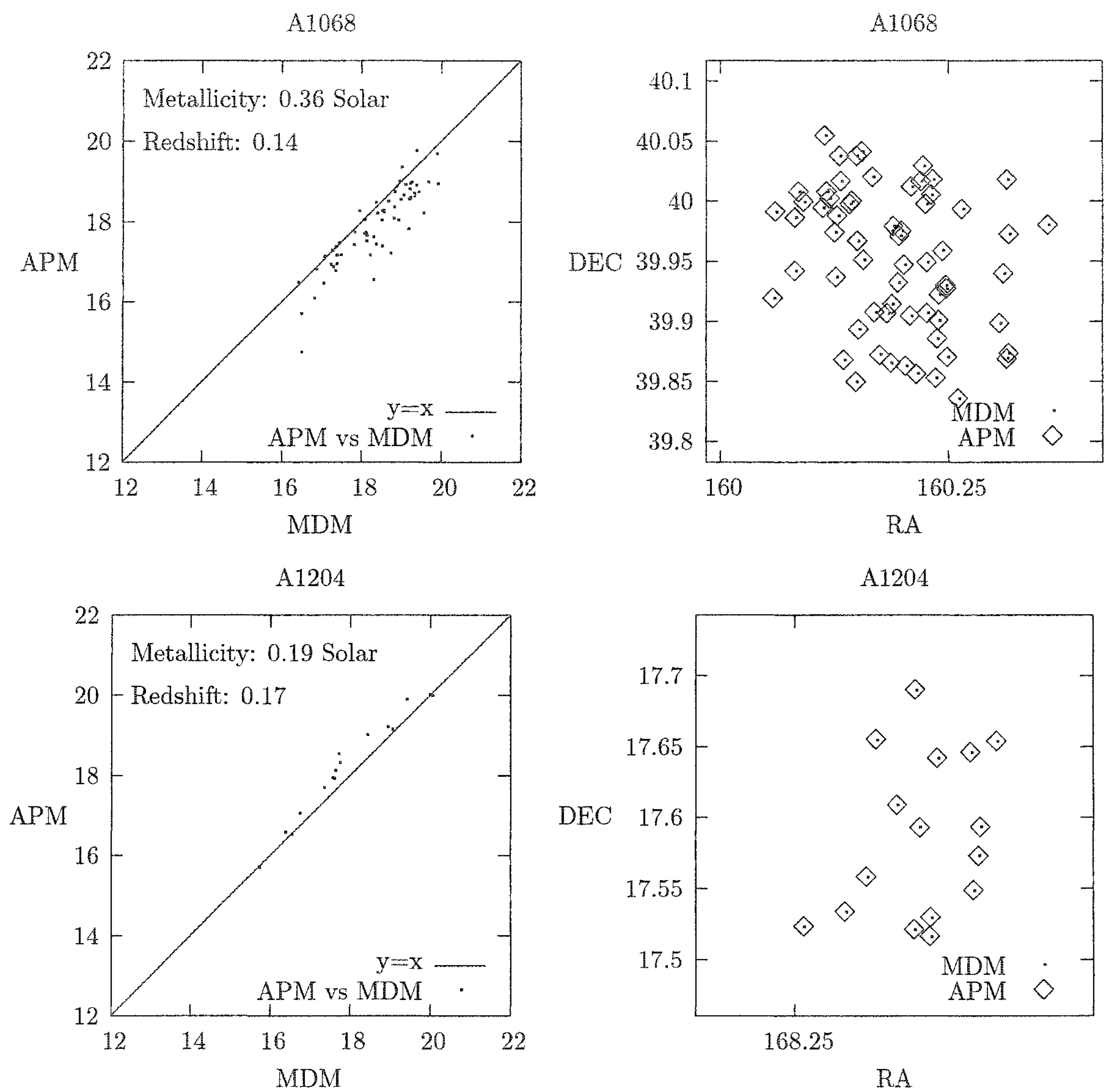
A1068
Metallicity: 0.36 Solar
Redshift: 0.14
APM
MDM
y=x
APM vs MDM
A1068
DEC
RA
MDM
APM
A1204
Metallicity: 0.19 Solar
Redshift: 0.17
APM
MDM
y=x
APM vs MDM
A1204
DEC
RA
MDM
APM

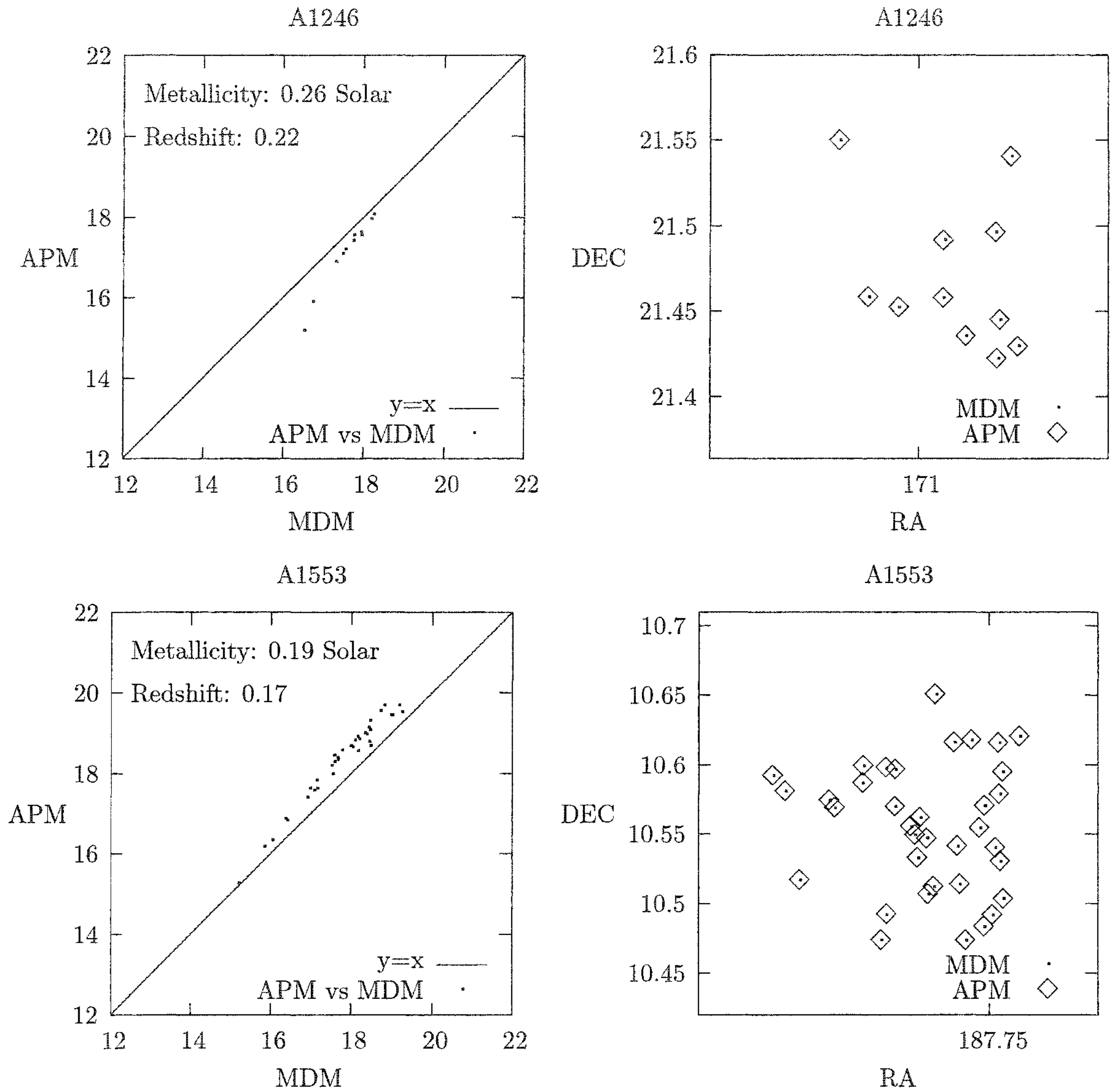
A1246
Metallicity: 0.26 Solar
Redshift: 0.22
APM
MDM
y=x
APM vs MDM
12
14
16
18
20
22
A1246
DEC
RA
21.6
21.55
21.5
21.45
21.4
171
MDM
APM
A1553
Metallicity: 0.19 Solar
Redshift: 0.17
APM
MDM
y=x
APM vs MDM
A1553
DEC
RA
10.7
10.65
10.6
10.55
10.5
10.45
187.75
MDM
APM

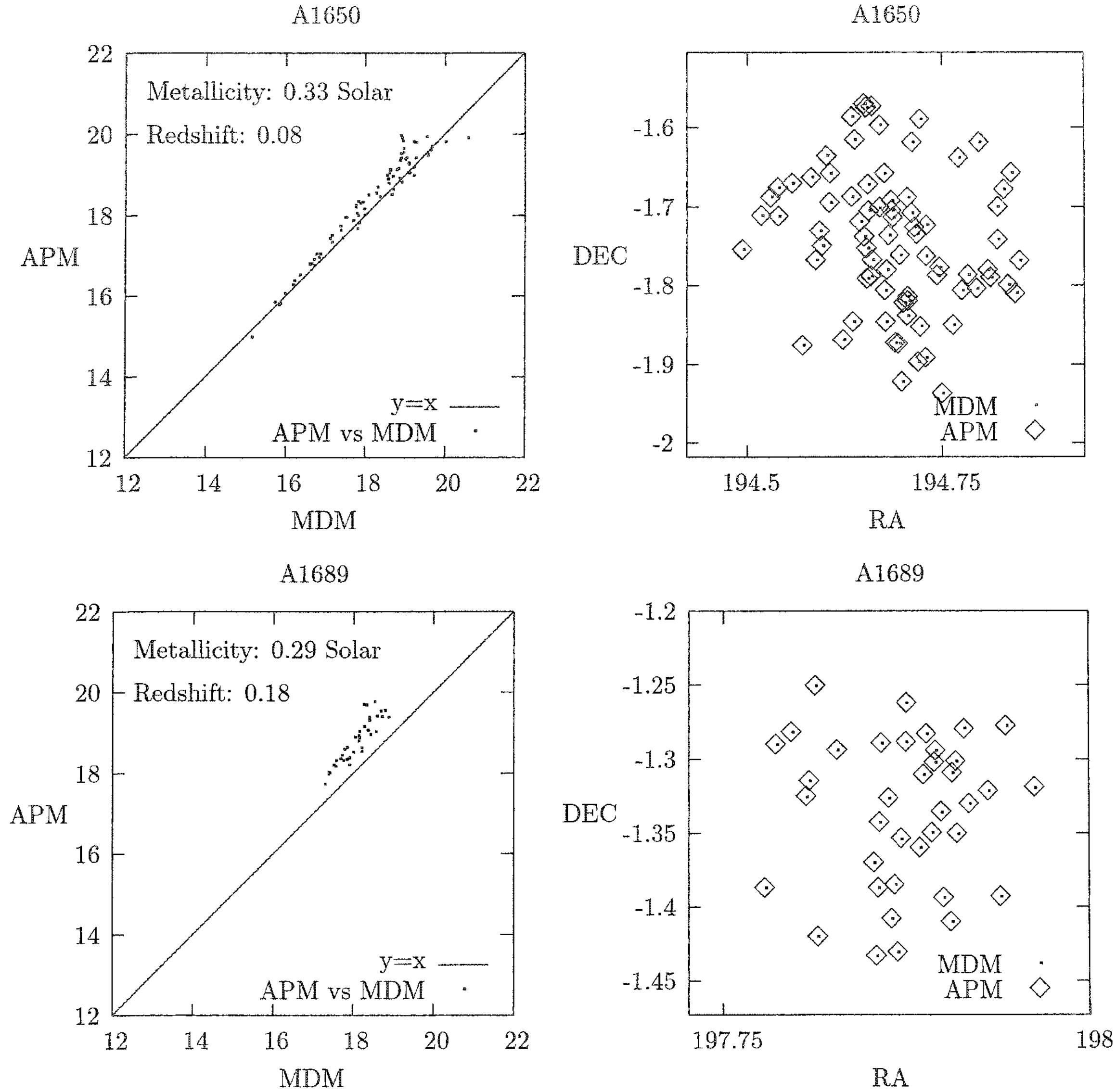
A1650
Metallicity: 0.33 Solar
Redshift: 0.08
APM
MDM
y=x
APM vs MDM
A1650
DEC
RA
194.5
194.75
MDM
APM
A1689
Metallicity: 0.29 Solar
Redshift: 0.18
APM
MDM
y=x
APM vs MDM
A1689
DEC
RA
197.75
198
MDM
APM

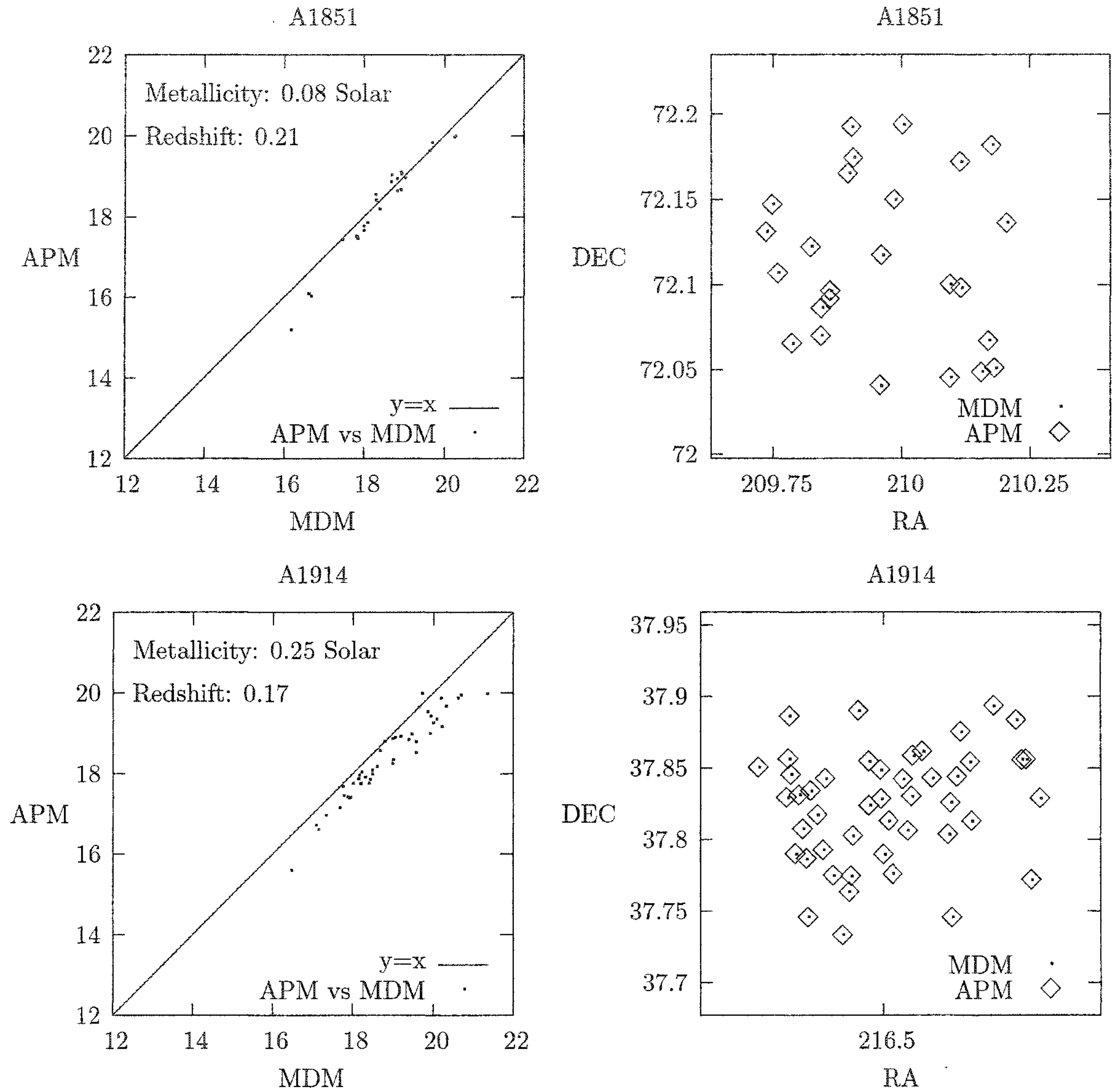
A1851
Metallicity: 0.08 Solar
Redshift: 0.21
y=x
APM vs MDM
APM
MDM
A1851
DEC
RA
MDM
APM
A1914
Metallicity: 0.25 Solar
Redshift: 0.17
y=x
APM vs MDM
APM
MDM
A1914
DEC
RA
MDM
APM

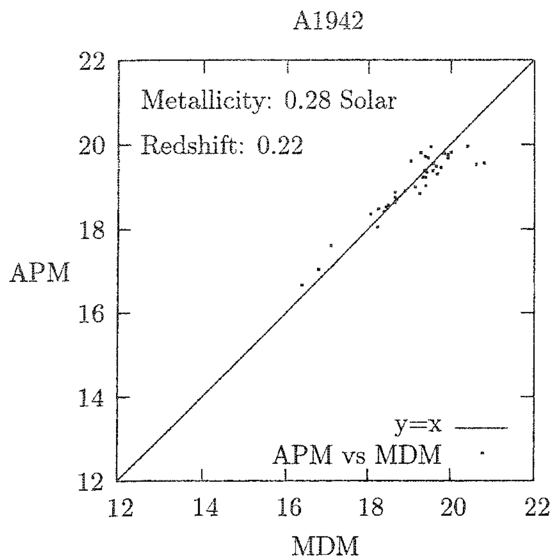
A1942
Metallicity: 0.28 Solar
Redshift: 0.22
y=x
APM vs MDM
APM
MDM
12
14
16
18
20
22

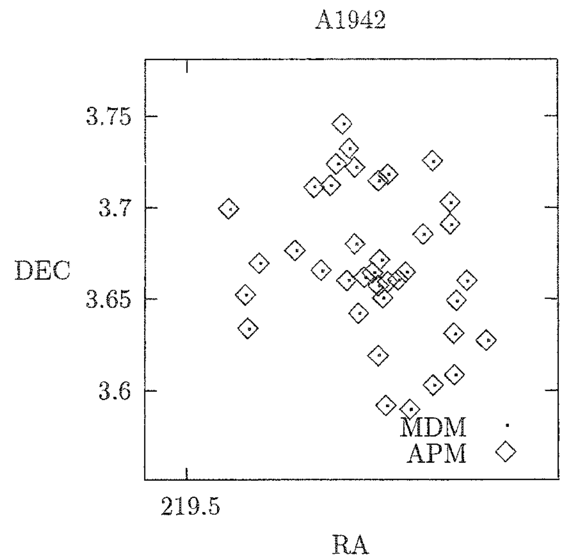
A1942
DEC
RA
3.75
3.7
3.65
3.6
219.5
MDM
APM

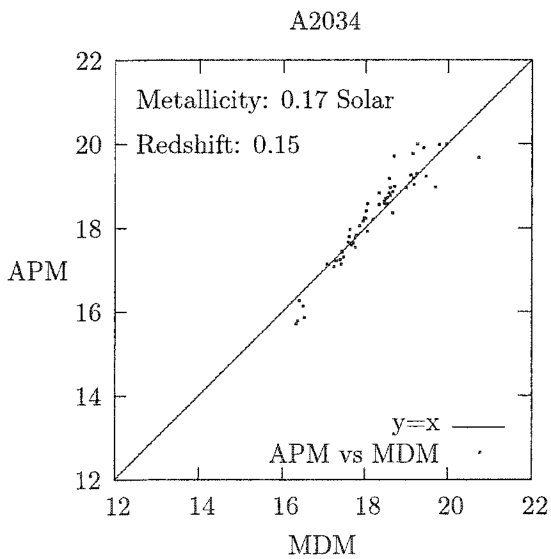
A2034
Metallicity: 0.17 Solar
Redshift: 0.15
y=x
APM vs MDM
APM
MDM
12
14
16
18
20
22

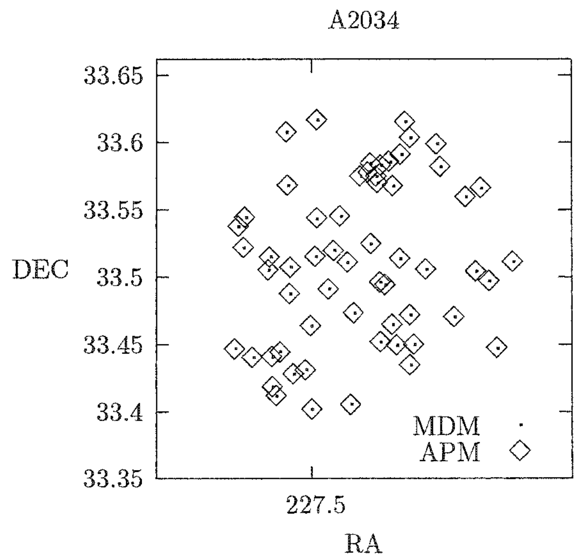
A2034
DEC
RA
33.65
33.6
33.55
33.5
33.45
33.4
33.35
227.5
MDM
APM

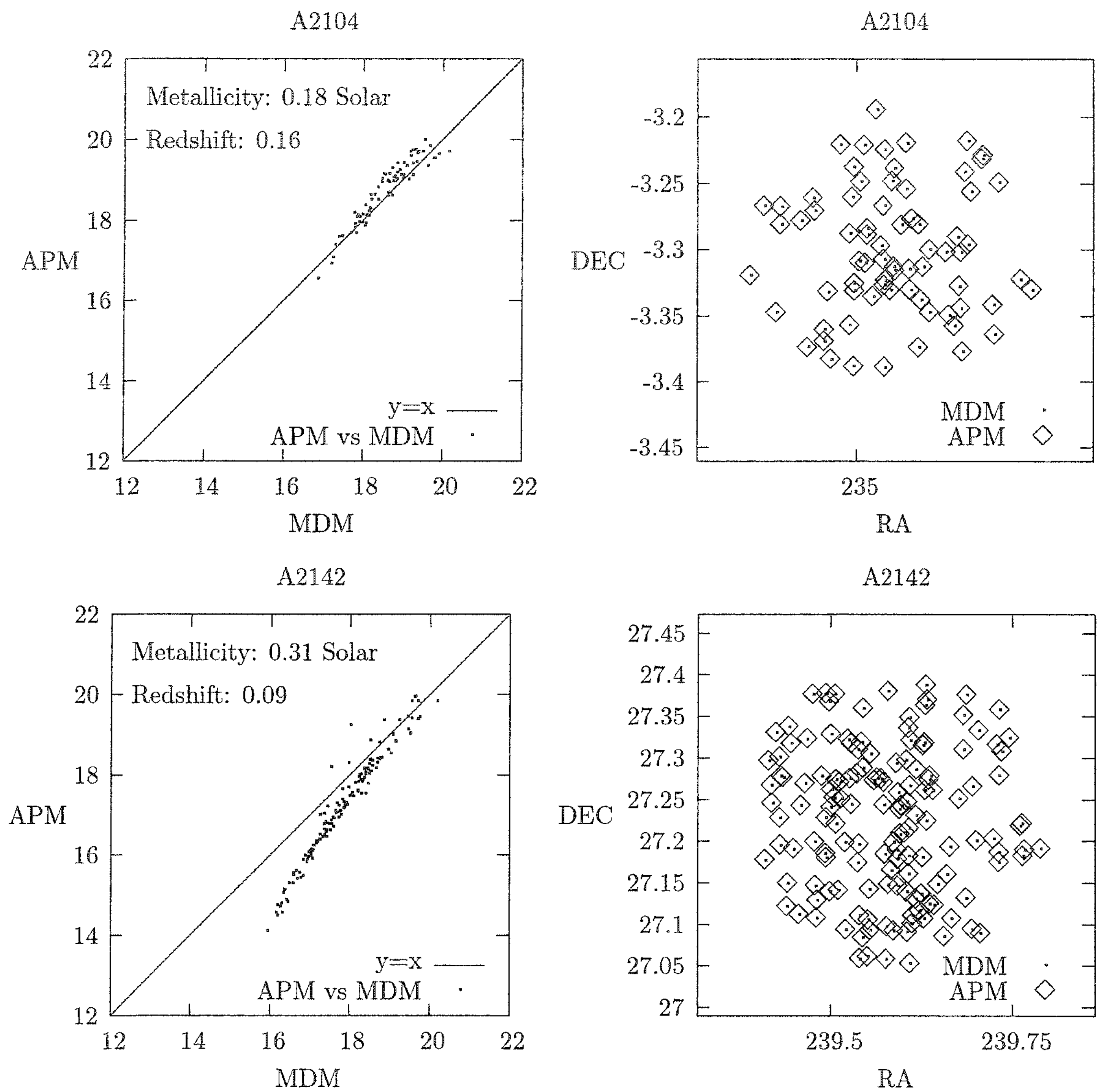
A2104
Metallicity: 0.18 Solar
Redshift: 0.16
APM
MDM
y=x
APM vs MDM
A2104
DEC
RA
MDM
APM
A2142
Metallicity: 0.31 Solar
Redshift: 0.09
APM
MDM
y=x
APM vs MDM
A2142
DEC
RA
MDM
APM

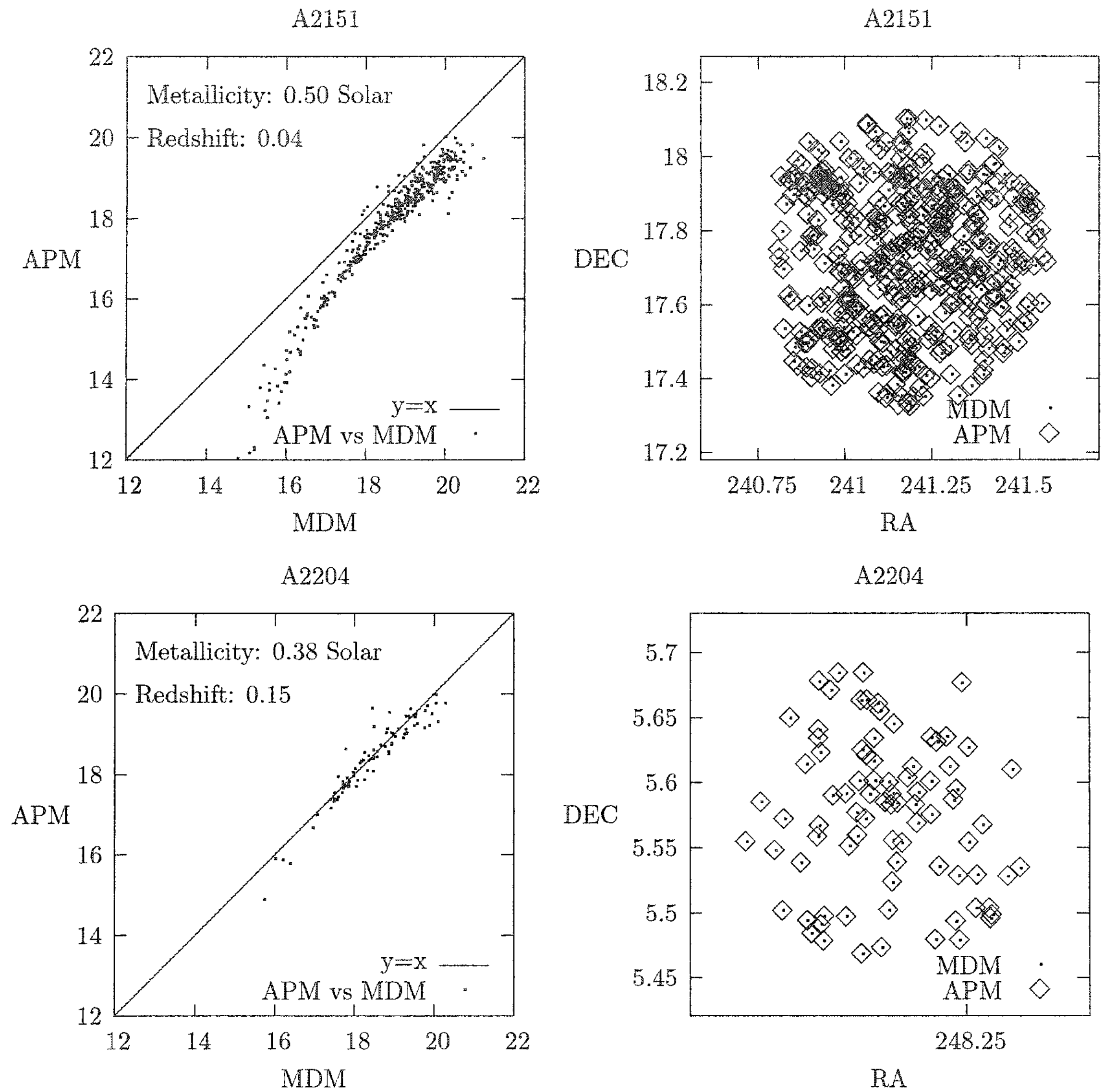
A2151
Metallicity: 0.50 Solar
Redshift: 0.04
y=x
APM vs MDM
APM
MDM
12
14
16
18
20
22
A2151
DEC
RA
18.2
18
17.8
17.6
17.4
17.2
240.75
241
241.25
241.5
MDM
APM
A2204
Metallicity: 0.38 Solar
Redshift: 0.15
y=x
APM vs MDM
APM
MDM
A2204
DEC
RA
5.7
5.65
5.6
5.55
5.5
5.45
248.25
MDM
APM

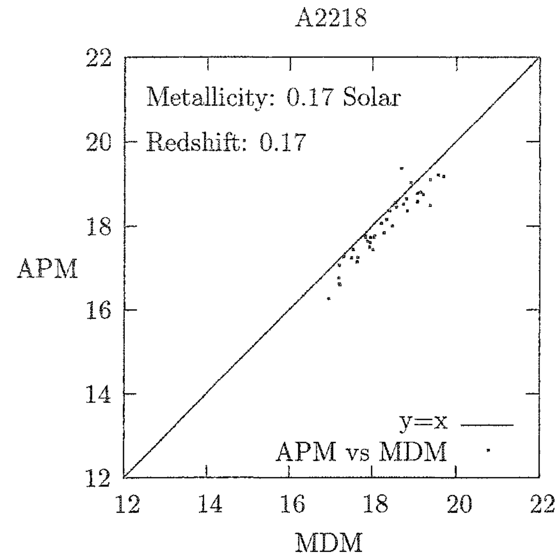
A2218
Metallicity: 0.17 Solar
Redshift: 0.17
APM
MDM
y=x
APM vs MDM
12
14
16
18
20
22

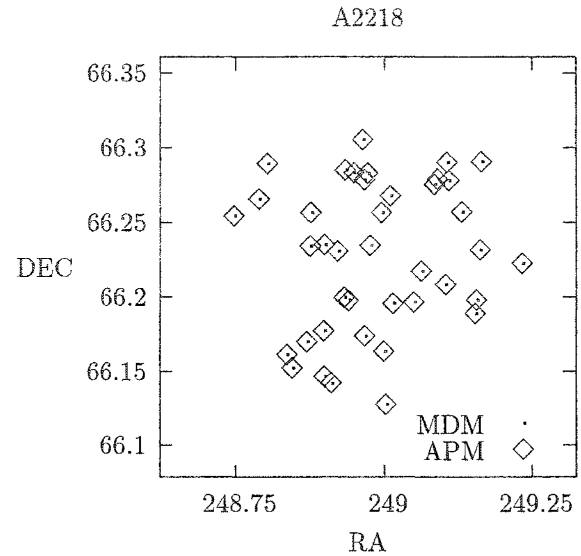
A2218
DEC
RA
66.35
66.3
66.25
66.2
66.15
66.1
248.75
249
249.25
MDM
APM

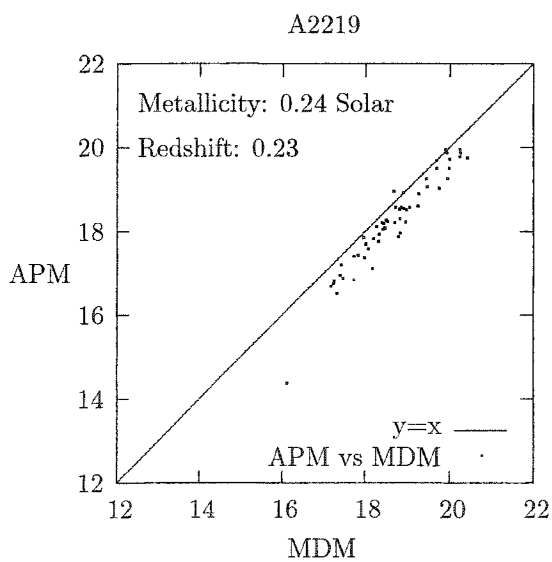
A2219
Metallicity: 0.24 Solar
Redshift: 0.23
APM
MDM
y=x
APM vs MDM
12
14
16
18
20
22

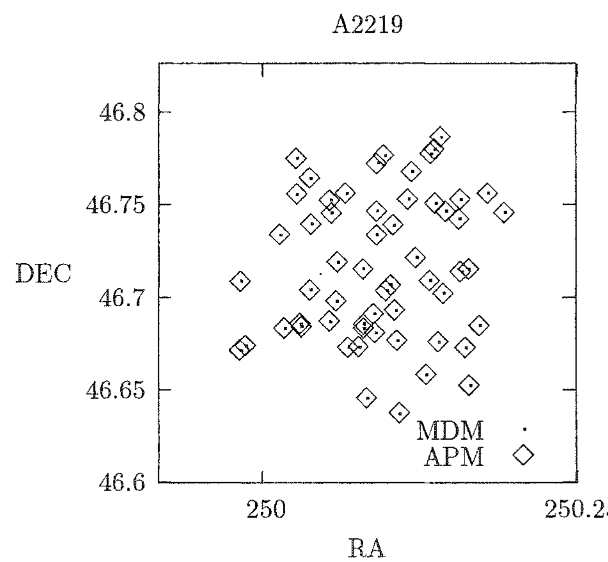
A2219
DEC
RA
46.8
46.75
46.7
46.65
46.6
250
250.25
MDM
APM

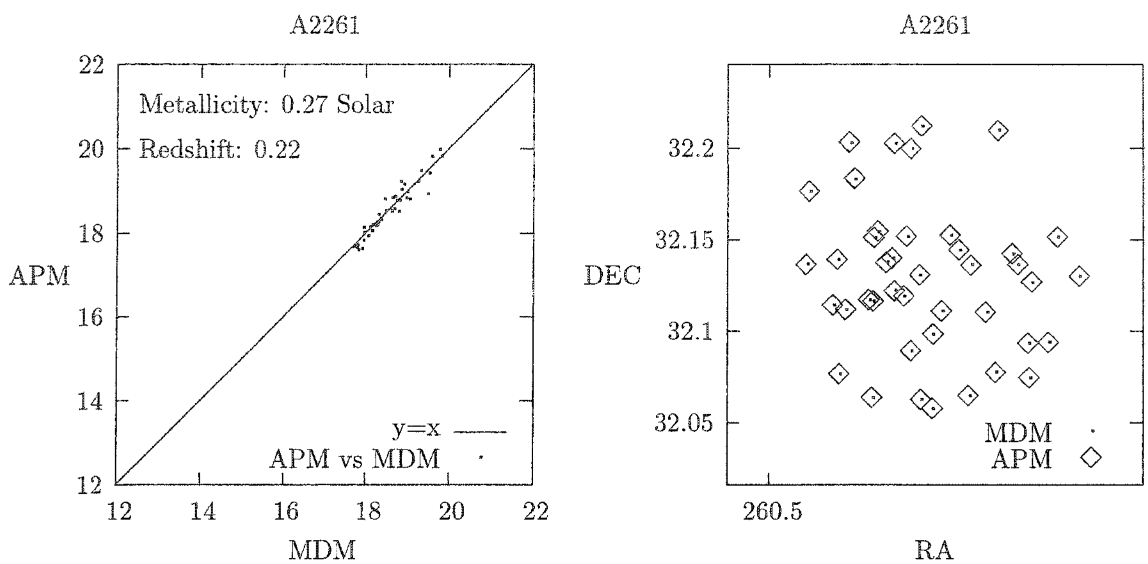
A2261
Metallicity: 0.27 Solar
Redshift: 0.22
y=x
APM vs MDM
APM
MDM
22
20
18
16
14
12
A2261
DEC
RA
32.2
32.15
32.1
32.05
260.5
MDM
APM

CHAPTER 8

LUMINOSITY FUNCTIONS

In this chapter we discuss how the absolute magnitudes are computed for the cluster galaxies. We discuss the method used to generate the luminosity functions, and present the luminosity functions for our entire sample.

8.1 Absolute Magnitude

In order to compare different clusters, it is important to calibrate the magnitude measurements. The absolute magnitude, M, an object is given by $M = m - \mu - A$ where m is the apparent magnitude and A is the galactic absorption. μ is a function of distance and therefore, depends on the cosmology used, the Hubble constant, and the redshift of the object. For $\Lambda_m = 0.25$ and Λ_k=0.75,

$$\mu = 42.384 - 5\log(h) + 5\log(z) + 5\log(1+z) + 5\log(1 - 0.1875z).$$

Appendix A shows the derivation of μ. Here the distance used contains the K-correction.

8.2 Galactic Absorption

A galaxy appears fainter in any given bandpass depending on the amount of the dust from the Milky Way in the line of site to the galaxy. The absorption in the R bandpass can be approximated by $A_r = 0.07(\csc|b| - 1)$ for $|b| \leq 50$ and $A_R = 0$ for $|b| > 50$ (Sandage 1973). The extinction can be computed, for a given direction and filter, if the amount of dust is known in that direction. Schlegel et

al (1998) present a full-sky 100 μm map, commonly referred to as SFD map, that is a reprocessed composite of the COBE/DIRBE and IRAS/ ISSA maps, with the zodiacal foreground and point sources removed. The fluxes can be converted to a number proportional to dust column density. The extinction in a given bandpass can be found by using this dust extinction value for a given galactic coordinate are made publicly available by Schlegel et al. Figure 23 and 24 show the extinction images for the northern and the southern hemispheres of our galaxy. The outer rim of the images correspond to the galactic equator and hence show the most amount of extinction. These dust maps are used to find the interstellar absorption in the R band for the clusters we observed and the clusters obtained from the APM archives. The SDSS archive contain the extinction that are derived from the SFD map.

The absolute magnitudes for all the cluster galaxies from all the sources used for this project (CCD observations, APM data and SDSS data) are computed using the average redshifts with respect to the cosmic background radiation (z), galaxy magnitudes in red, and the intergalactic absorption (A_R) using $M = m - 42.384 + 5\log(h) - 5\log(z) - 5\log(1+z) - 5\log(1-0.1875z) - A$.

8.3 Luminosity Functions

The Luminosity function for a galaxy cluster gives the number distribution for the luminosity of the cluster galaxies. The integral luminosity function $N(L)$ is the number of galaxies with luminosities greater than L, while the differential luminosity function $n(L)dL$ is the number of galaxies with luminosities between L and $L+dL$. Luminosity functions are often defined in terms of magnitudes $m \propto -2.5\ \log(L)$ with $N(m)$ being number of galaxies brighter than the magnitude of m. There are three types of analytical functions that have commonly been used for fitting the luminosity functions.

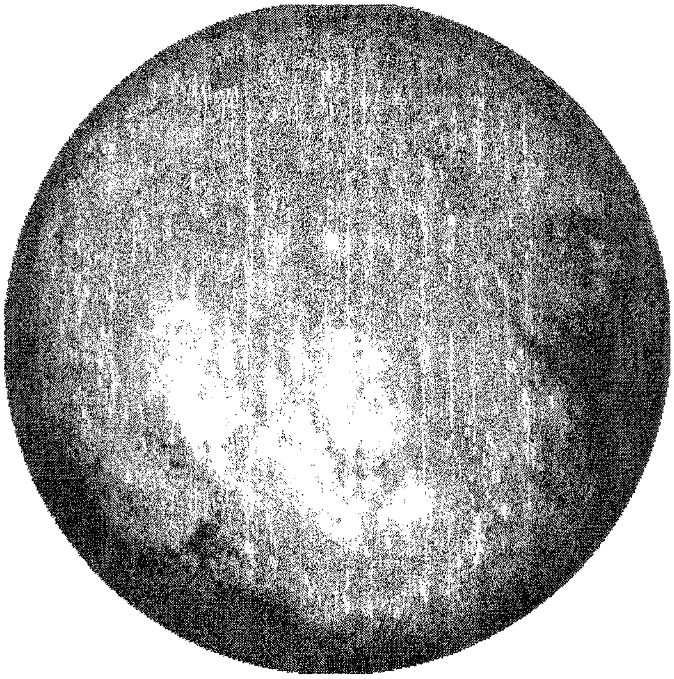

Figure 23 SFD Dust Map for Norther Galactic Hemisphere

1. A form proposed by Zwicky (1957):

$$N(M) = K(10^{0.2(M-M_1)} - 1),$$

where K is a constant and M_1 is the magnitude of the first brightest galaxy.

2. Two intersecting power lows suggested by Abell (1975):

$$\log N(M) = \begin{cases} K_1 + s_1\, M & M \leq M^* \\ K_2 + s_2\, M & M > M^* \end{cases},$$

where K_1 and K_2 are constants and the slops are approximately $s_1 \approx 0.75$ and $s_2 \approx 0.25$, and the power laws cross at $M = M^*$, making $K_1 + s_1\, M^* = K_1 + s_1\, M^*$.

3. A function proposed by Schechter (1976):

$$n(M)dM = k\; N^*\; e^{k(\alpha+1)(M^*-M) - e^{k\,(M^*-M)}} dM,$$

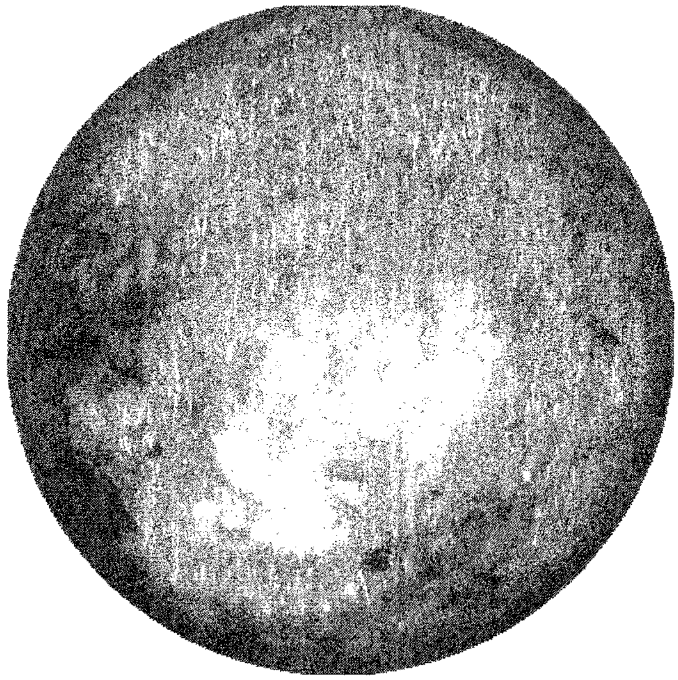

Figure 24 SFD Dust Map for Southern Galactic Hemisphere

where M^* is the characteristic magnitude, or the 'knee', of the LF, α is the slope of the faint end of the function, k =ln(10)/2.5, and N^* is determined by requiring that the total number of galaxies expected by the Schechter function equal the number of galaxies in a given magnitude range.

Figure 25 shows all of the above functions fit to the LF generated for the cluster Abell 2244. Unlike the Zwicky function, the Schechter function does not depend on the magnitude of the brightest cluster galaxy and therefore, shows a better fit at the bright end of LF. The Schechter function is also continuous like the Zwicky function opposed to a discontinuous Abell function. We use Schechter functions for our project to compute M^*'s for our sample. These M^* values are than used for investigating the possible connection with the cluster metallicities.

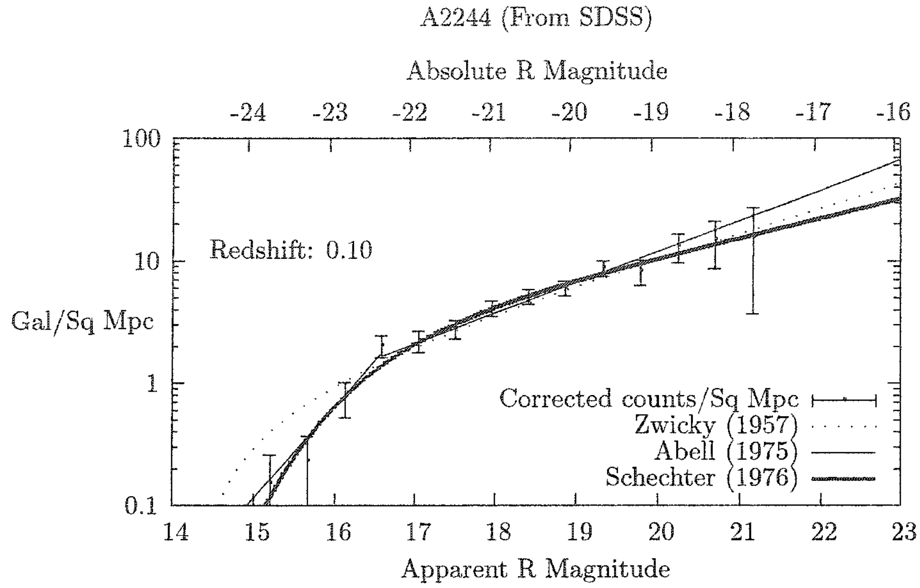

Figure 25 LF of A2244 with Analytical Functions Fits

8.4 Generating Luminosity Functions

Cluster data are sorted by brightness in 10 bins with the bin centers ranging from apparent magnitudes of 12 to 23. The bins include the brightest cD galaxies and galaxies fainter than the telescope limits. Each bin is corrected for background field galaxies using the background data obtained from SDSS. The number of background galaxies in each bin is estimated by averaging the number of galaxies in those bins from the fields centered on 4 Mpc east and west of the clusters in the SDSS sample. Figure 26 shows the plot of average number of galaxies per square Mpc verses apparent magnitude. It is found that number of galaxies $N(m)$ per square degrees per magnitude in the R band can be approximated by $\log N(m) = 0.42\ m - 5.0$. This result agrees with the findings by Parolin et al. (2003) of $\log N(m) = (0.39 \pm 0.063)\ m - (4.67 \pm 1.01)$.

Schechter functions are fit to the field corrected bins to compute M^* values for all the sample clusters. Towards the bright ends of the LFs, the fits exclude the

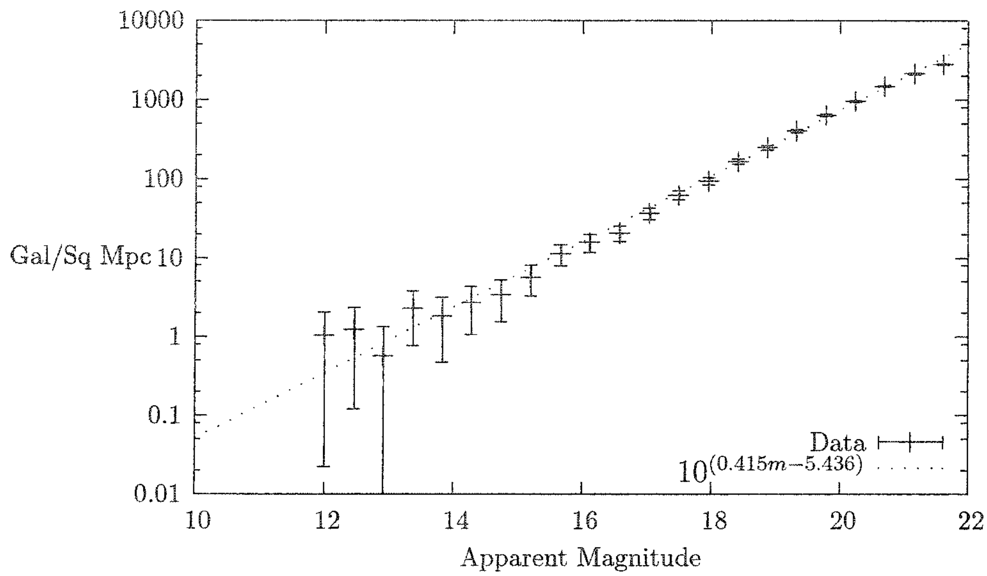

Figure 26 Average background from SDSS

bright cD galaxies, and galaxies fainter than the apparent magnitudes between 21 and 22 on the faint end. Even though the effective limiting magnitude of the SDSS telescope is 22, variations in airmass could make this limit brighter for some image. Figures on the following pages show the LFs and Schechter function fits to all the clusters in our sample. The figures also show the images of the clusters in X-ray, obtained from the ASCA archive, and position plots of the cluster galaxies using the SDSS data. The circles around the X-ray images are drawn with a radius of 500 Kpc.

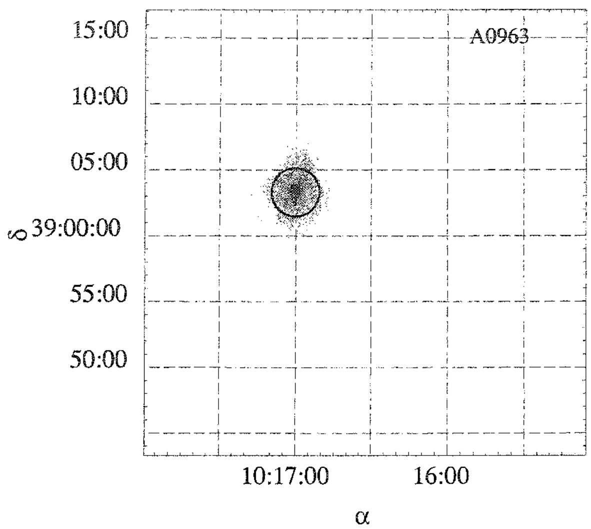
A0963
15:00
10:00
05:00
δ 39:00:00
55:00
50:00
10:17:00
16:00
α

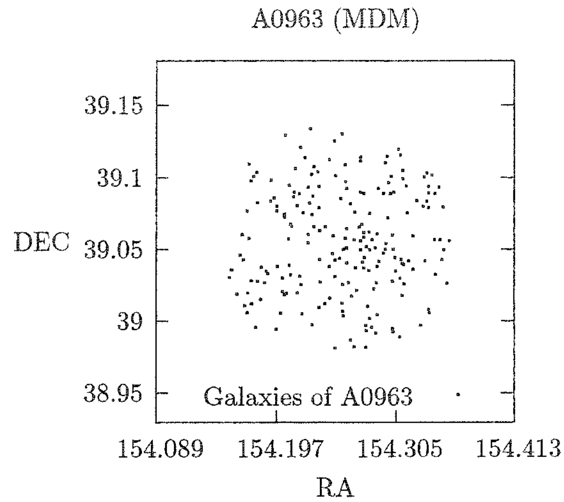
A0963 (MDM)
DEC
39.15
39.1
39.05
39
38.95
Galaxies of A0963
154.089
154.197
154.305
154.413
RA

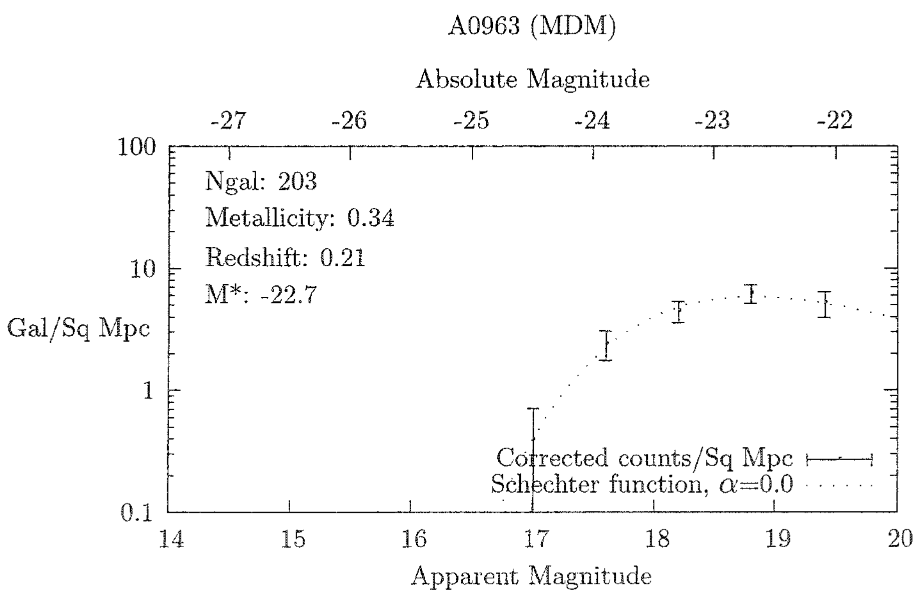
A0963 (MDM)
Absolute Magnitude
-27
-26
-25
-24
-23
-22
100
10
1
0.1
Gal/Sq Mpc
Ngal: 203
Metallicity: 0.34
Redshift: 0.21
M*: -22.7
Corrected counts/Sq Mpc
Schechter function, α=0.0
14
15
16
17
18
19
20
Apparent Magnitude

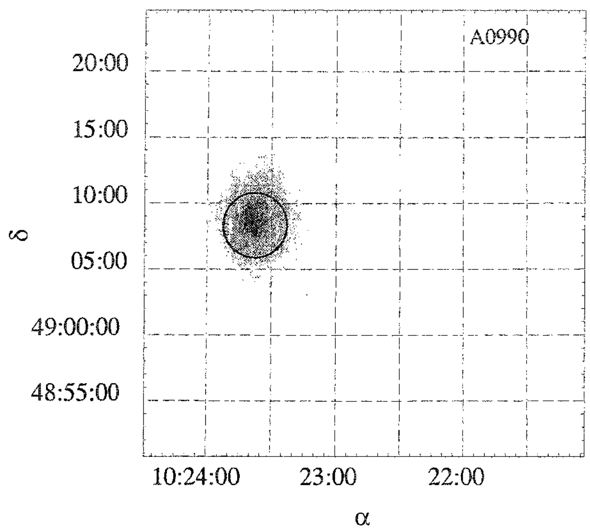
A0990
20:00
15:00
10:00
05:00
49:00:00
48:55:00
δ
10:24:00
23:00
22:00
α

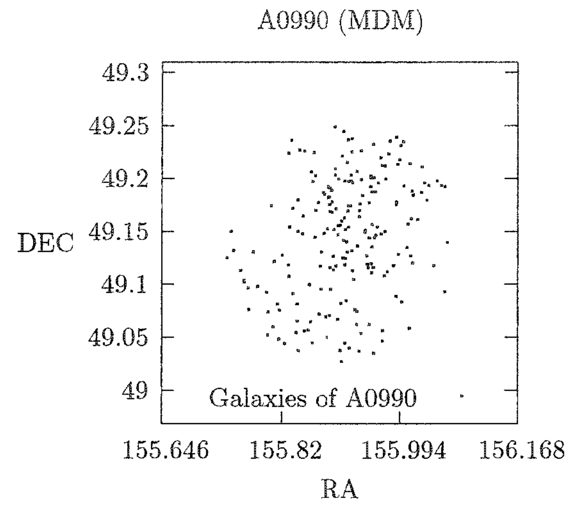
A0990 (MDM)
49.3
49.25
49.2
49.15
49.1
49.05
49
DEC
Galaxies of A0990
155.646
155.82
155.994
156.168
RA

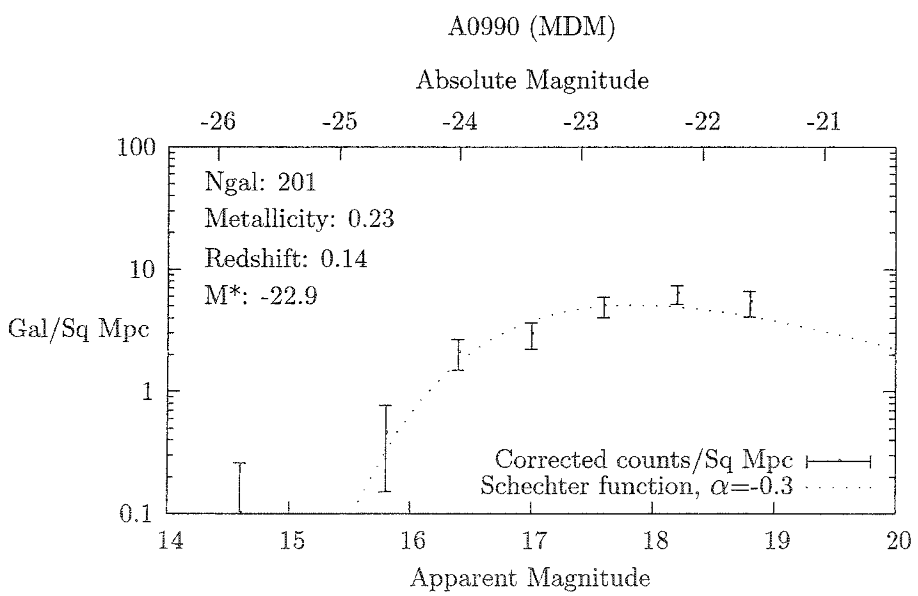
A0990 (MDM)
Absolute Magnitude
-26
-25
-24
-23
-22
-21
100
10
1
0.1
Gal/Sq Mpc
Ngal: 201
Metallicity: 0.23
Redshift: 0.14
M*: -22.9
Corrected counts/Sq Mpc
Schechter function, α=-0.3
14
15
16
17
18
19
20
Apparent Magnitude

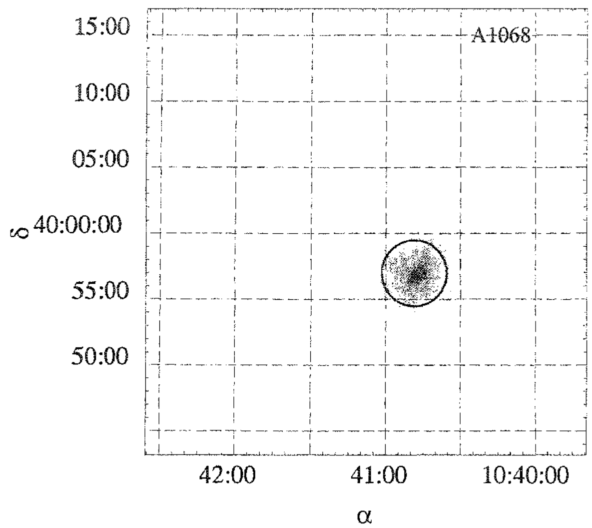
A1068
15:00
10:00
05:00
δ 40:00:00
55:00
50:00
42:00
41:00
10:40:00
α

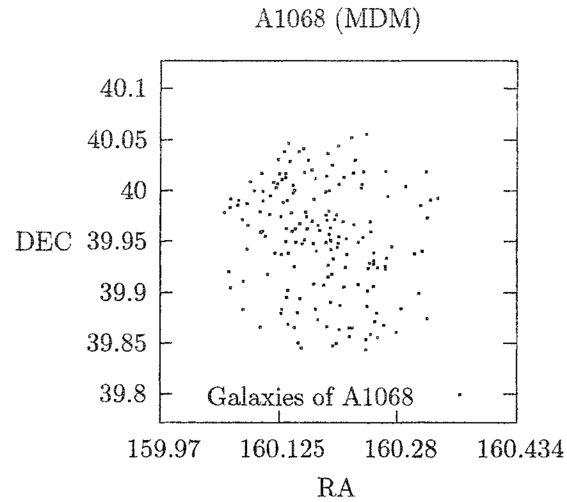
A1068 (MDM)
40.1
40.05
40
DEC 39.95
39.9
39.85
39.8
Galaxies of A1068
159.97
160.125
160.28
160.434
RA

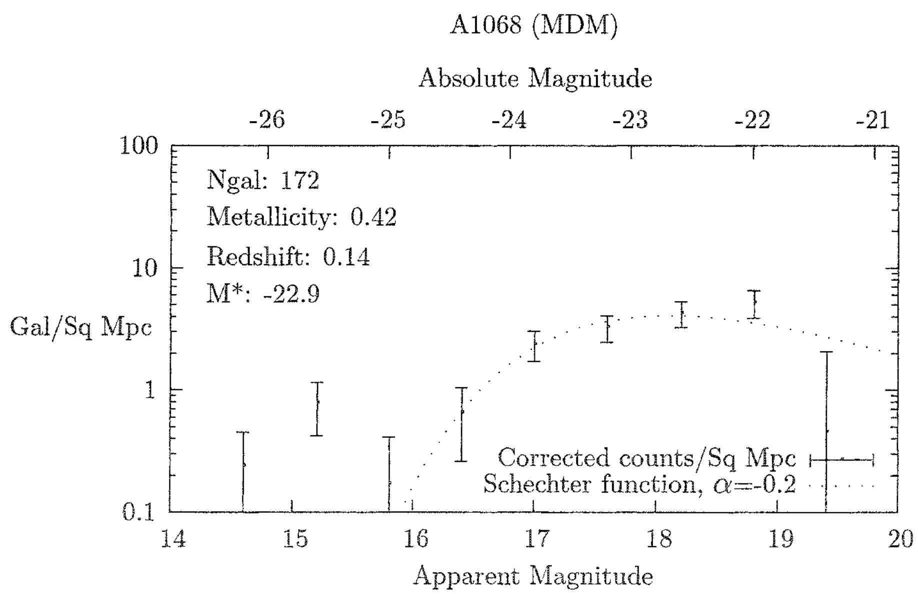
A1068 (MDM)
Absolute Magnitude
-26
-25
-24
-23
-22
-21
100
10
Gal/Sq Mpc
1
0.1
Ngal: 172
Metallicity: 0.42
Redshift: 0.14
M*: -22.9
Corrected counts/Sq Mpc
Schechter function, α=-0.2
14
15
16
17
18
19
20
Apparent Magnitude

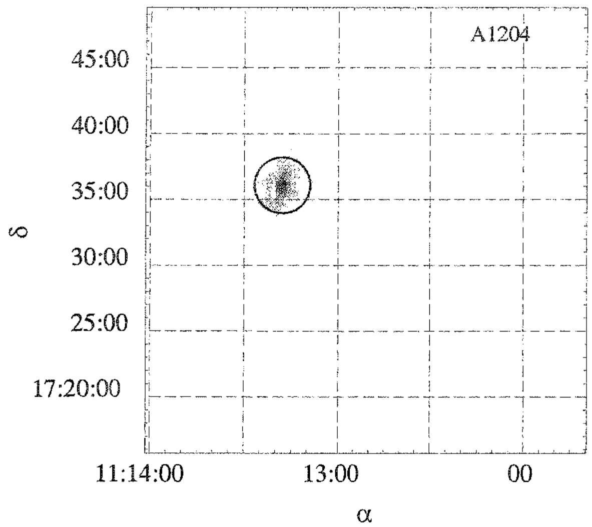
A1204
45:00
40:00
35:00
30:00
25:00
17:20:00
δ
11:14:00
13:00
00
α

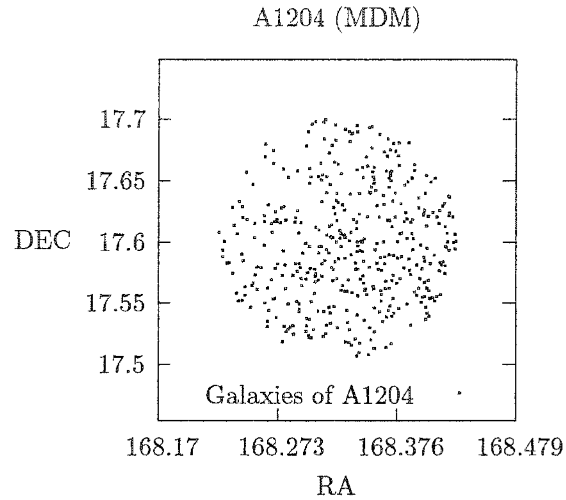
A1204 (MDM)
DEC
17.7
17.65
17.6
17.55
17.5
Galaxies of A1204
168.17
168.273
168.376
168.479
RA

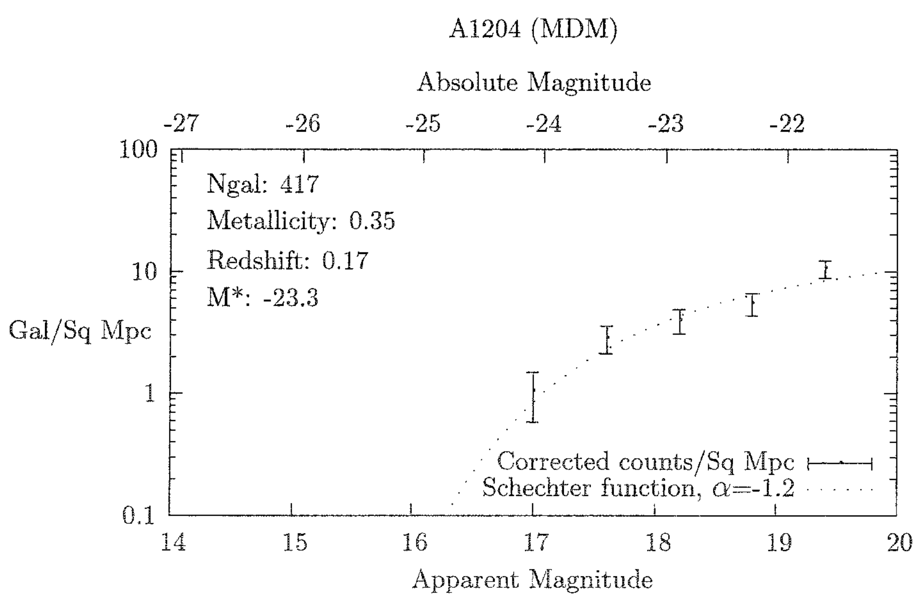
A1204 (MDM)
Absolute Magnitude
-27
-26
-25
-24
-23
-22
100
10
1
0.1
Gal/Sq Mpc
Ngal: 417
Metallicity: 0.35
Redshift: 0.17
M*: -23.3
Corrected counts/Sq Mpc
Schechter function, α=-1.2
14
15
16
17
18
19
20
Apparent Magnitude

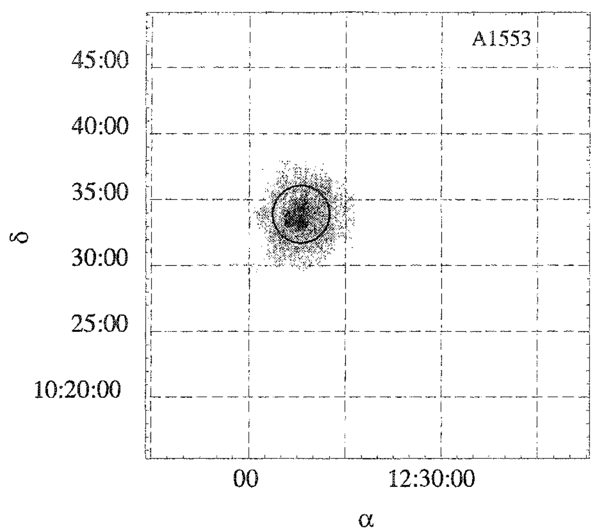
A1553
45:00
40:00
35:00
30:00
25:00
10:20:00
δ
00
12:30:00
α

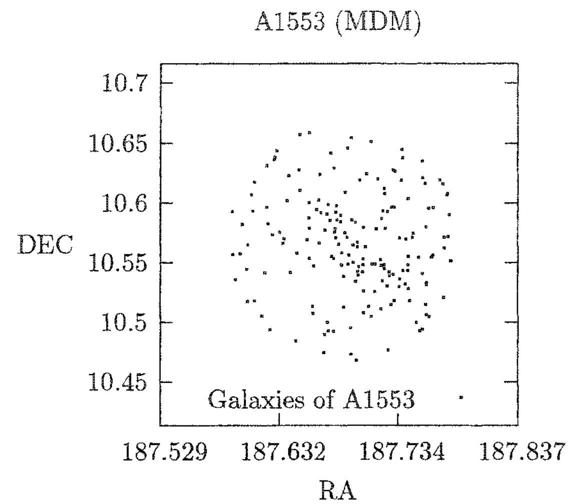
A1553 (MDM)
10.7
10.65
10.6
10.55
10.5
10.45
DEC
Galaxies of A1553
187.529
187.632
187.734
187.837
RA

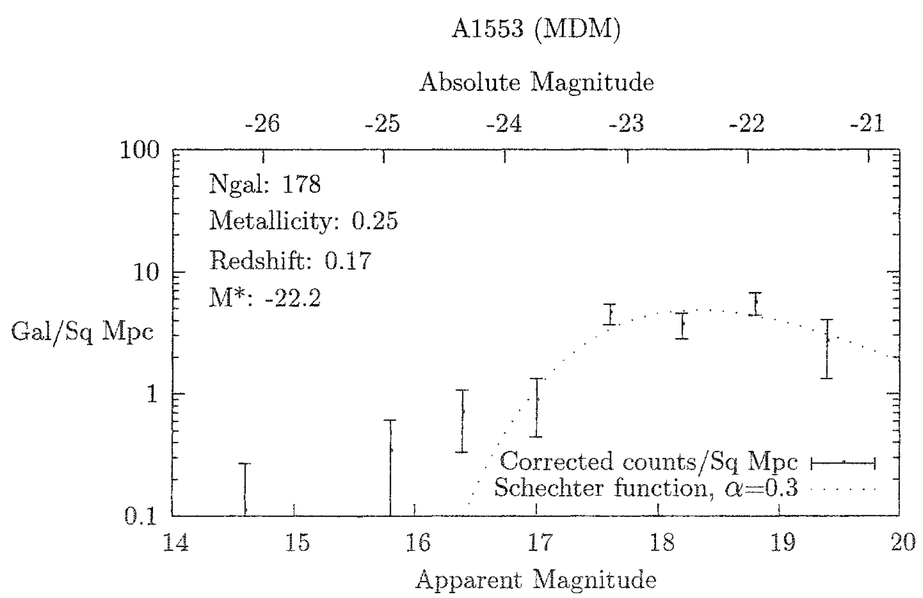
A1553 (MDM)
Absolute Magnitude
-26
-25
-24
-23
-22
-21
100
10
1
0.1
Gal/Sq Mpc
Ngal: 178
Metallicity: 0.25
Redshift: 0.17
M*: -22.2
Corrected counts/Sq Mpc
Schechter function, α=0.3
14
15
16
17
18
19
20
Apparent Magnitude

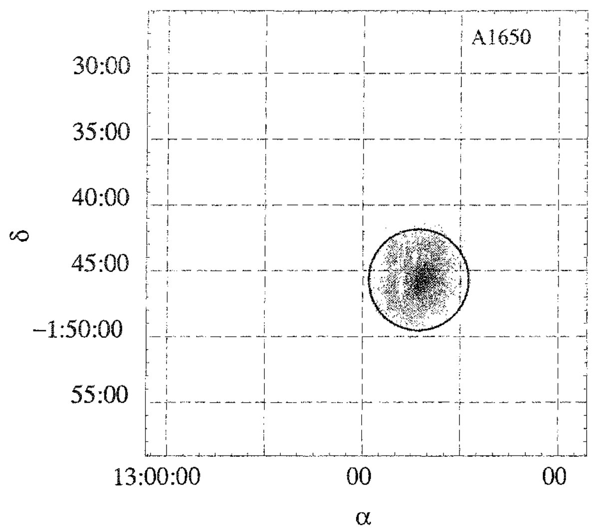
A1650
30:00
35:00
40:00
45:00
−1:50:00
55:00
δ
13:00:00
00
00
α

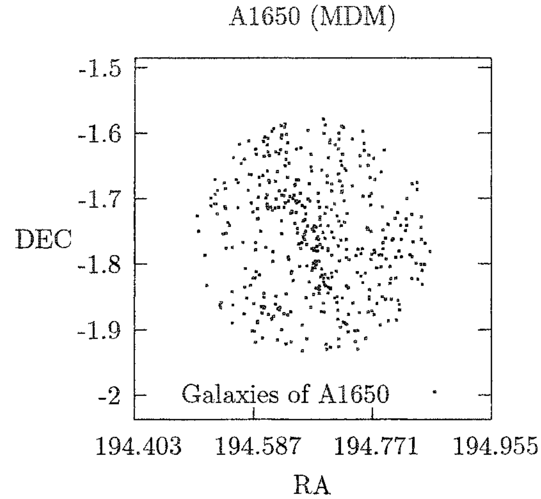
A1650 (MDM)
-1.5
-1.6
-1.7
-1.8
-1.9
-2
DEC
Galaxies of A1650
194.403
194.587
194.771
194.955
RA

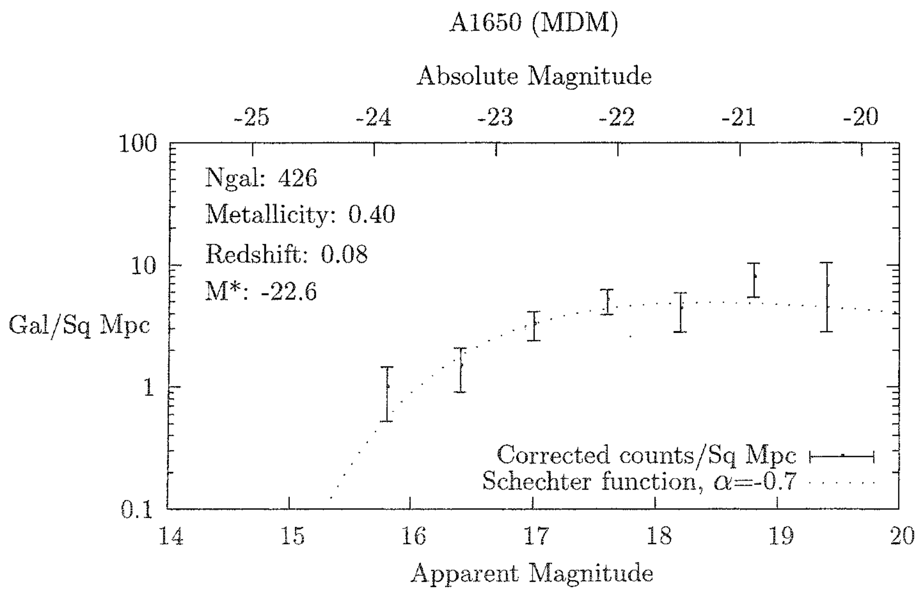
A1650 (MDM)
Absolute Magnitude
-25
-24
-23
-22
-21
-20
100
10
1
0.1
Gal/Sq Mpc
Ngal: 426
Metallicity: 0.40
Redshift: 0.08
M*: -22.6
Corrected counts/Sq Mpc
Schechter function, α=-0.7
14
15
16
17
18
19
20
Apparent Magnitude

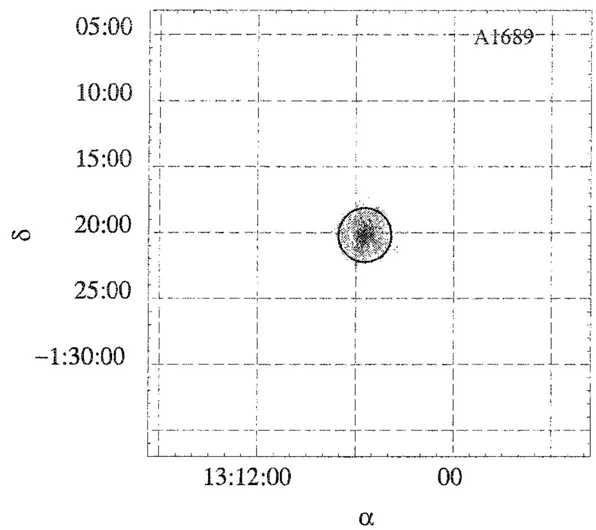

A1689
05:00
10:00
15:00
20:00
25:00
−1:30:00
δ
13:12:00
00
α

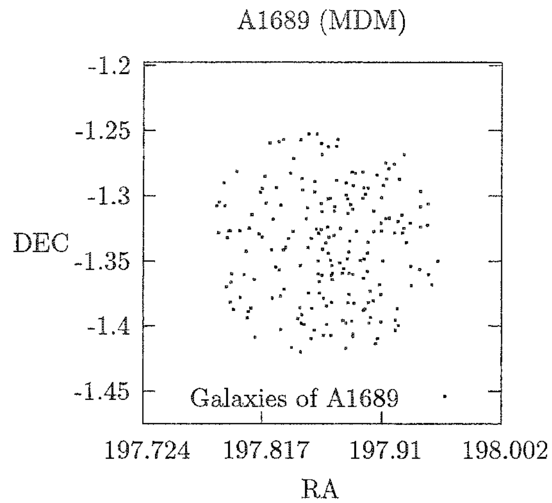

A1689 (MDM)
-1.2
-1.25
-1.3
-1.35
-1.4
-1.45
DEC
Galaxies of A1689
197.724
197.817
197.91
198.002
RA

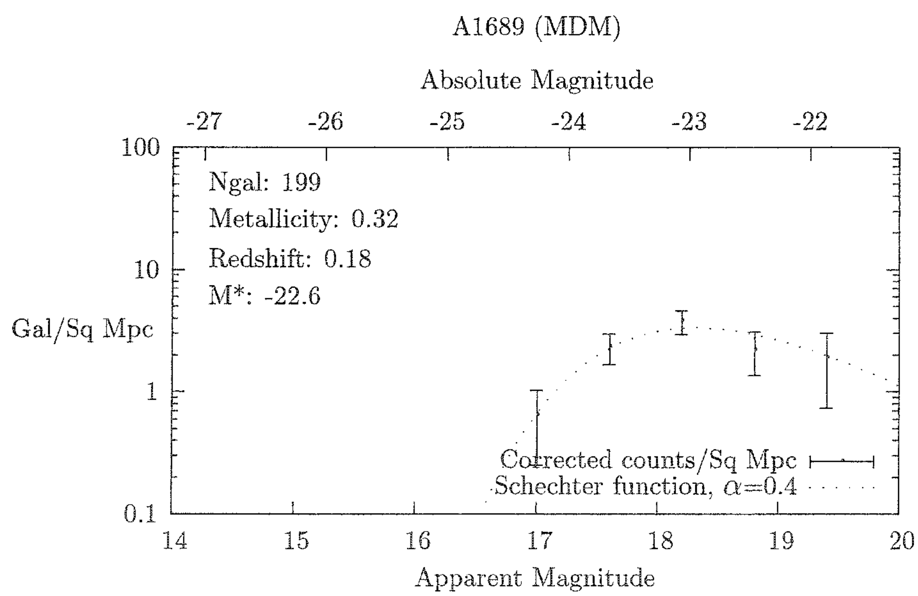

A1689 (MDM)
Absolute Magnitude
-27
-26
-25
-24
-23
-22
Ngal: 199
Metallicity: 0.32
Redshift: 0.18
M*: -22.6
100
10
1
0.1
Gal/Sq Mpc
Corrected counts/Sq Mpc
Schechter function, α=0.4
14
15
16
17
18
19
20
Apparent Magnitude

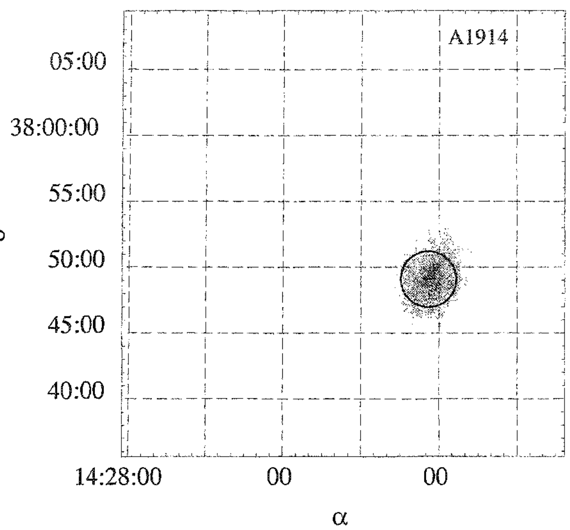
A1914
05:00
38:00:00
55:00
50:00
45:00
40:00
δ
14:28:00
00
00
α

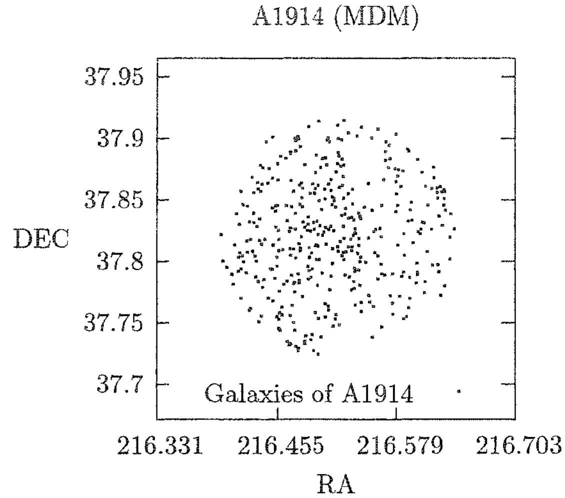
A1914 (MDM)
37.95
37.9
37.85
37.8
37.75
37.7
DEC
Galaxies of A1914
216.331
216.455
216.579
216.703
RA

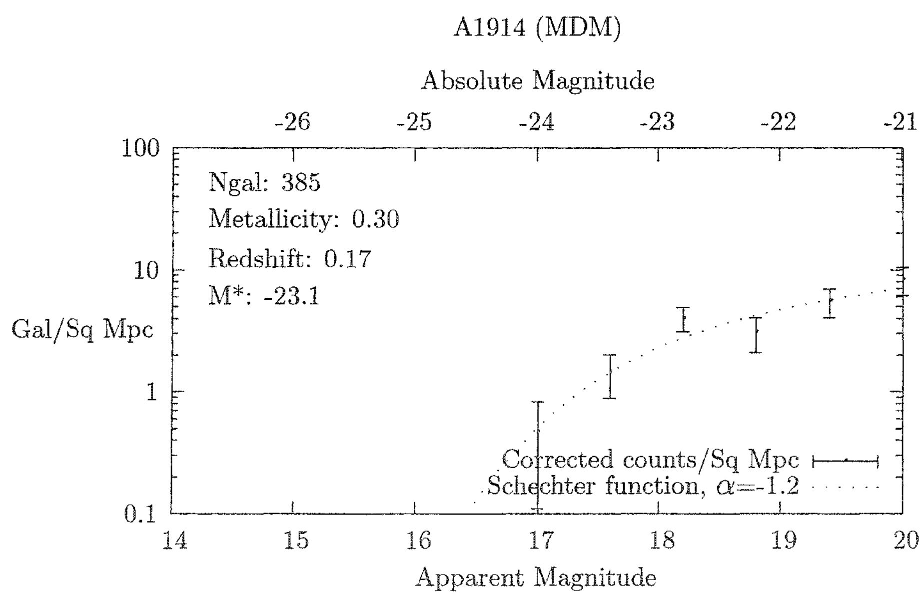
A1914 (MDM)
Absolute Magnitude
-26
-25
-24
-23
-22
-21
100
10
1
0.1
Gal/Sq Mpc
Ngal: 385
Metallicity: 0.30
Redshift: 0.17
M*: -23.1
Corrected counts/Sq Mpc
Schechter function, α=-1.2
14
15
16
17
18
19
20
Apparent Magnitude

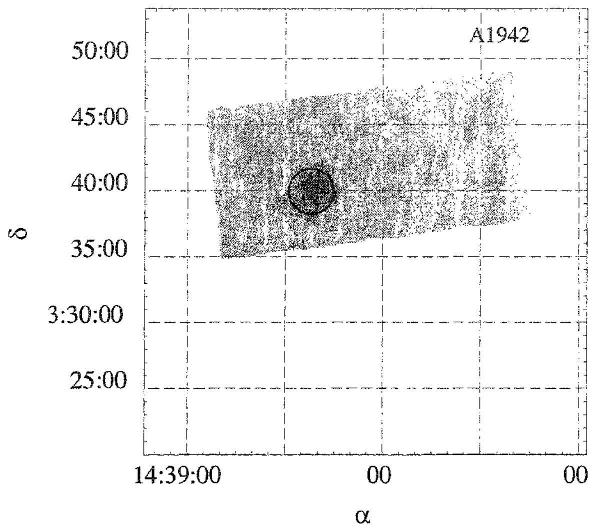
A1942
50:00
45:00
40:00
35:00
3:30:00
25:00
δ
14:39:00
00
00
α

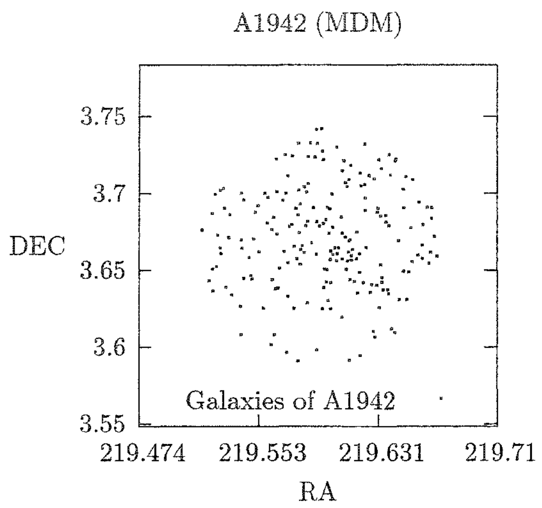
A1942 (MDM)
3.75
3.7
3.65
3.6
3.55
DEC
Galaxies of A1942
219.474
219.553
219.631
219.71
RA

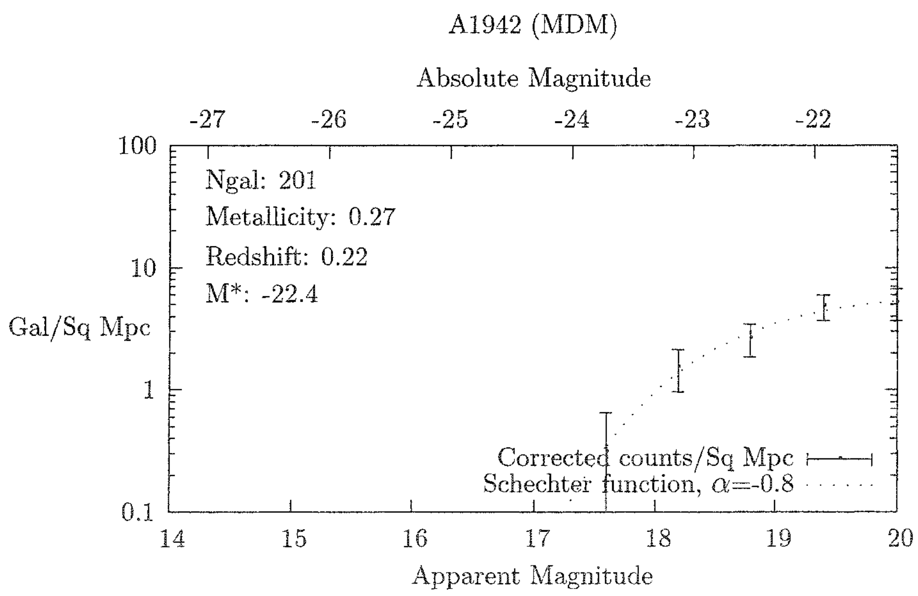
A1942 (MDM)
Absolute Magnitude
-27
-26
-25
-24
-23
-22
100
10
1
0.1
Gal/Sq Mpc
Ngal: 201
Metallicity: 0.27
Redshift: 0.22
M*: -22.4
Corrected counts/Sq Mpc
Schechter function, α=-0.8
14
15
16
17
18
19
20
Apparent Magnitude

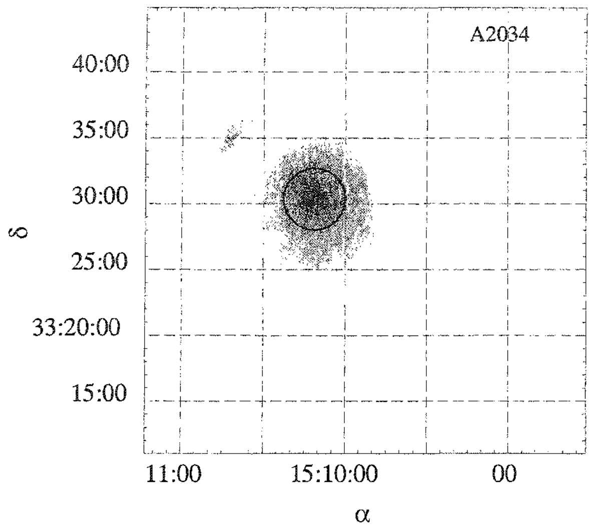
A2034
40:00
35:00
30:00
25:00
33:20:00
15:00
δ
11:00
15:10:00
00
α

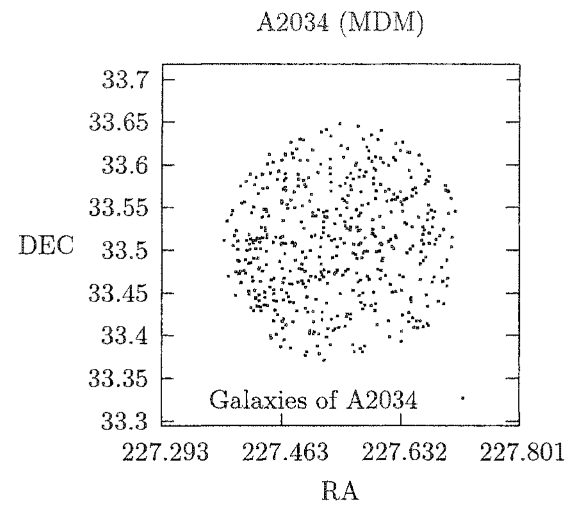
A2034 (MDM)
33.7
33.65
33.6
33.55
33.5
33.45
33.4
33.35
33.3
DEC
Galaxies of A2034
227.293
227.463
227.632
227.801
RA

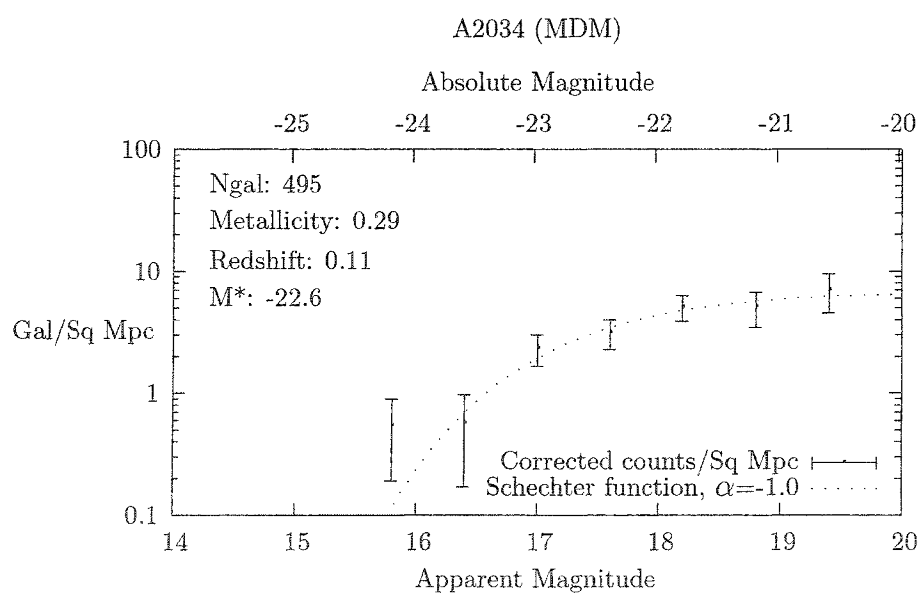
A2034 (MDM)
Absolute Magnitude
-25
-24
-23
-22
-21
-20
100
10
1
0.1
Gal/Sq Mpc
Ngal: 495
Metallicity: 0.29
Redshift: 0.11
M*: -22.6
Corrected counts/Sq Mpc
Schechter function, α=-1.0
14
15
16
17
18
19
20
Apparent Magnitude

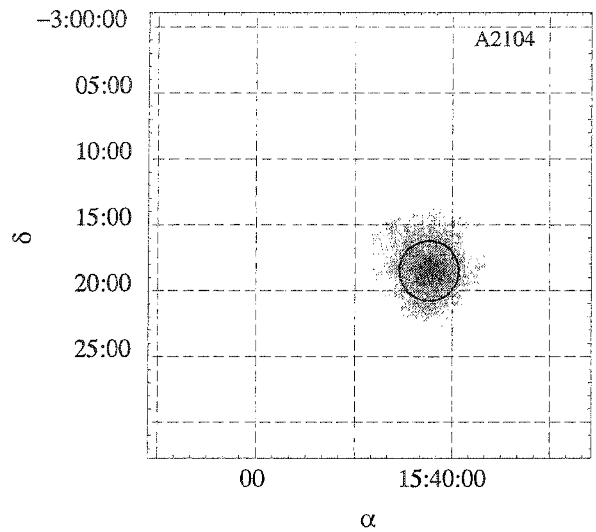
A2104
−3:00:00
05:00
10:00
15:00
20:00
25:00
δ
00
15:40:00
α

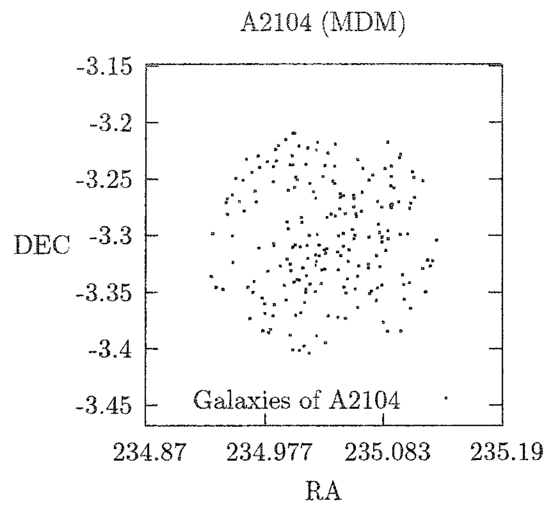
A2104 (MDM)
DEC
-3.15
-3.2
-3.25
-3.3
-3.35
-3.4
-3.45
Galaxies of A2104
234.87
234.977
235.083
235.19
RA

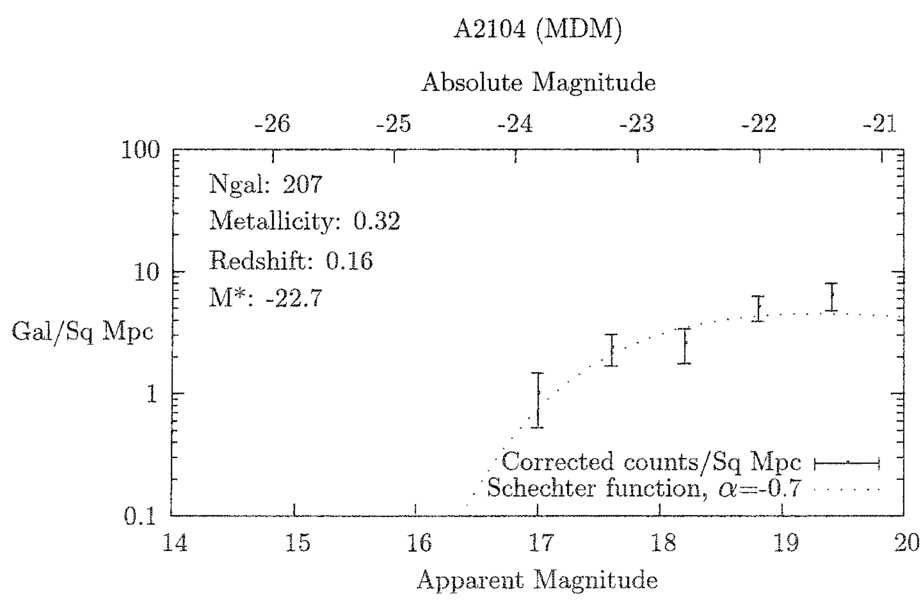
A2104 (MDM)
Absolute Magnitude
-26
-25
-24
-23
-22
-21
Ngal: 207
Metallicity: 0.32
Redshift: 0.16
M*: -22.7
Gal/Sq Mpc
100
10
1
0.1
Corrected counts/Sq Mpc
Schechter function, α=-0.7
14
15
16
17
18
19
20
Apparent Magnitude

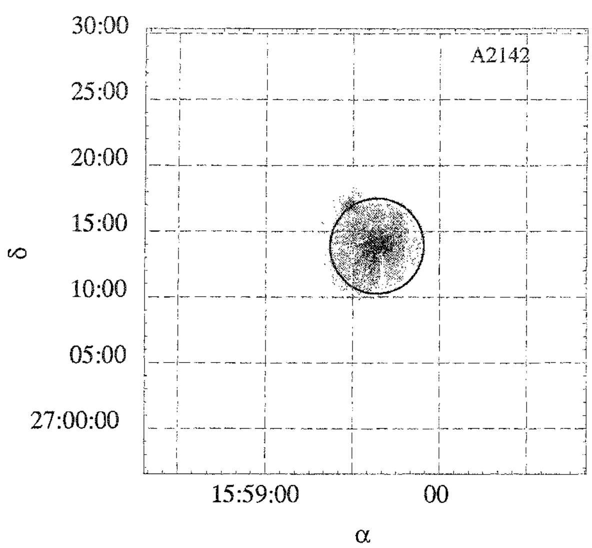
A2142
30:00
25:00
20:00
15:00
10:00
05:00
27:00:00
δ
15:59:00
00
α

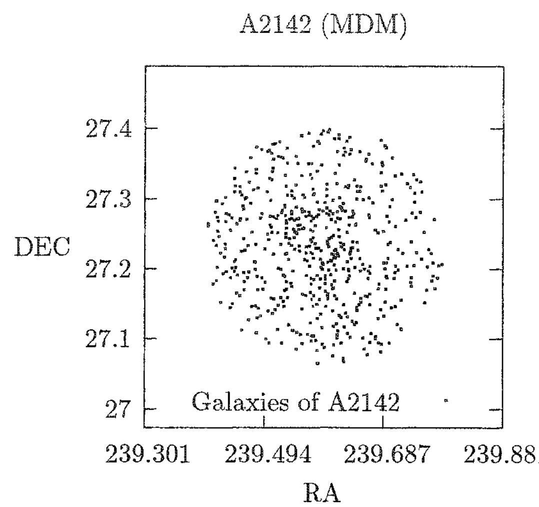
A2142 (MDM)
DEC
27.4
27.3
27.2
27.1
27
Galaxies of A2142
239.301
239.494
239.687
239.881
RA

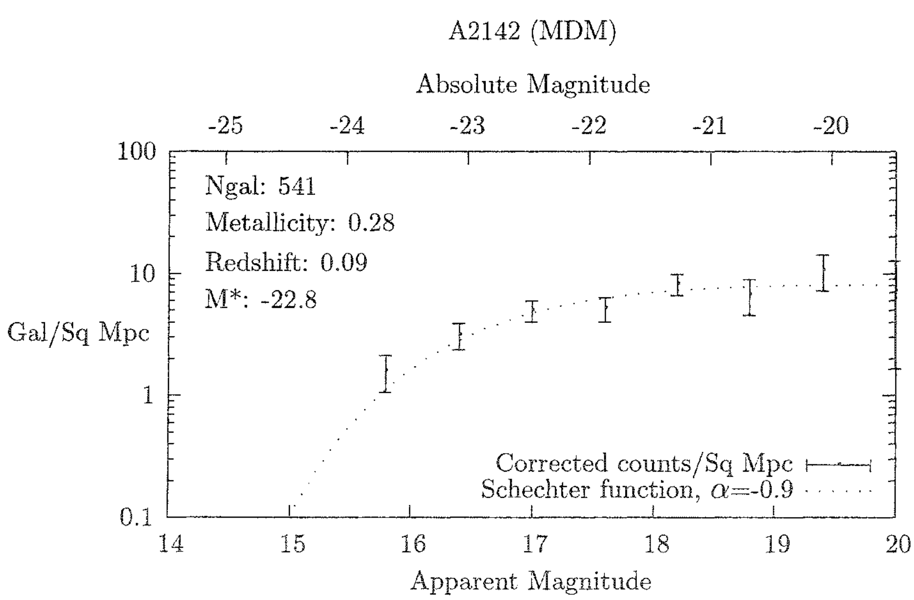
A2142 (MDM)
Absolute Magnitude
-25
-24
-23
-22
-21
-20
Ngal: 541
Metallicity: 0.28
Redshift: 0.09
M*: -22.8
Gal/Sq Mpc
100
10
1
0.1
Corrected counts/Sq Mpc
Schechter function, α=-0.9
14
15
16
17
18
19
20
Apparent Magnitude

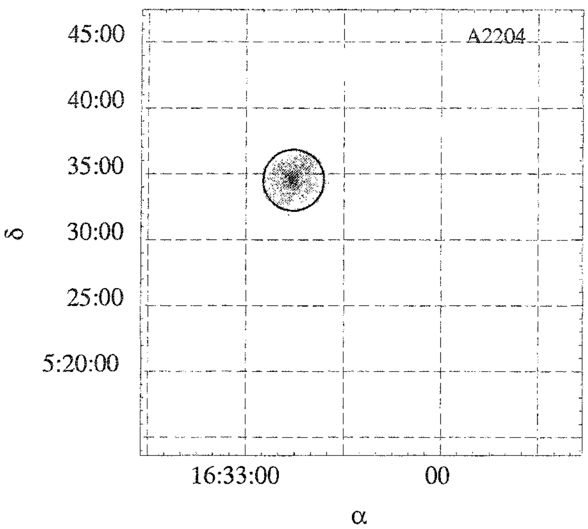
A2204
45:00
40:00
35:00
30:00
25:00
5:20:00
δ
16:33:00
00
α

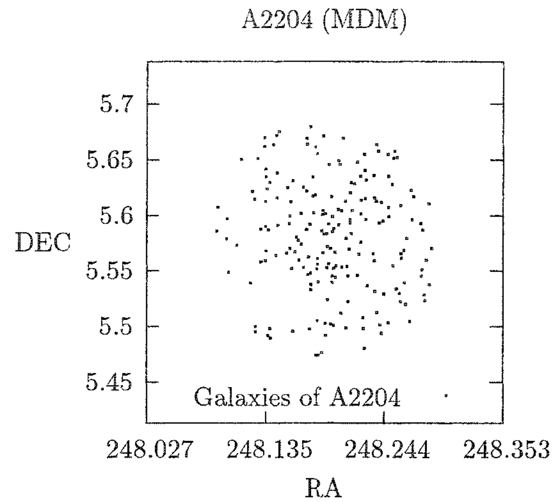
A2204 (MDM)
DEC
5.7
5.65
5.6
5.55
5.5
5.45
Galaxies of A2204
248.027
248.135
248.244
248.353
RA

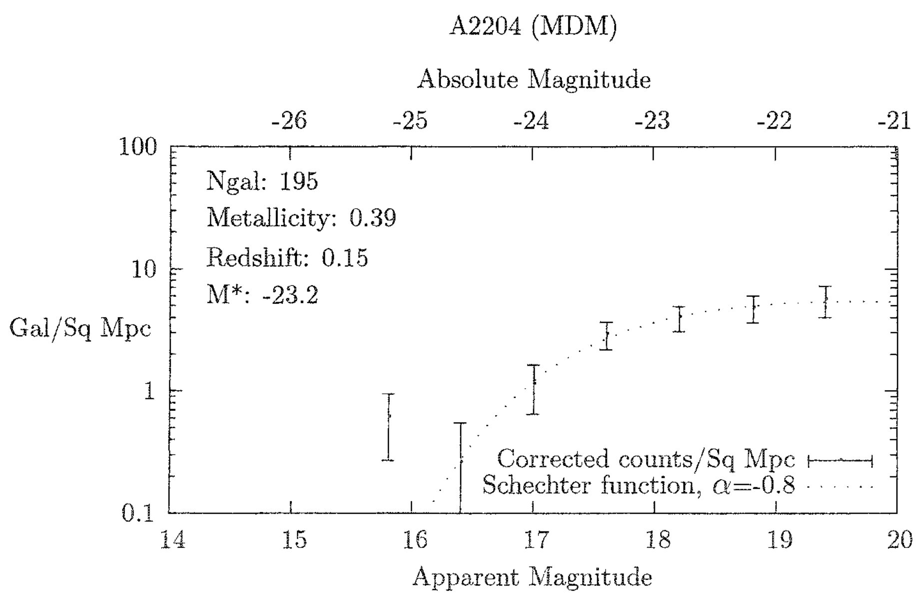
A2204 (MDM)
Absolute Magnitude
-26
-25
-24
-23
-22
-21
100
10
1
0.1
Gal/Sq Mpc
Ngal: 195
Metallicity: 0.39
Redshift: 0.15
M*: -23.2
Corrected counts/Sq Mpc
Schechter function, α=-0.8
14
15
16
17
18
19
20
Apparent Magnitude

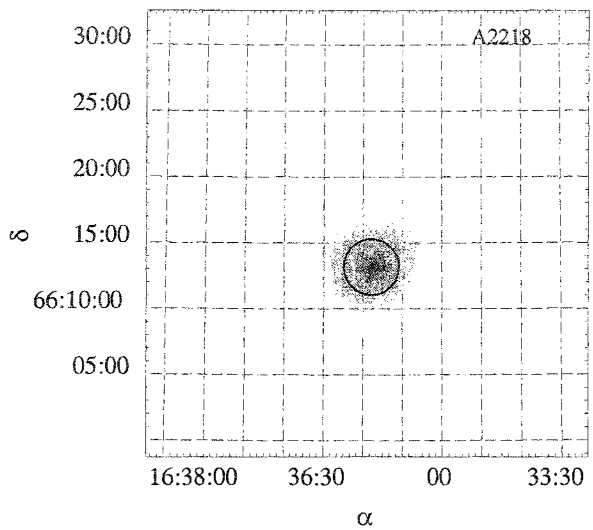

A2218
30:00
25:00
20:00
15:00
66:10:00
05:00
δ
16:38:00
36:30
00
33:30
α

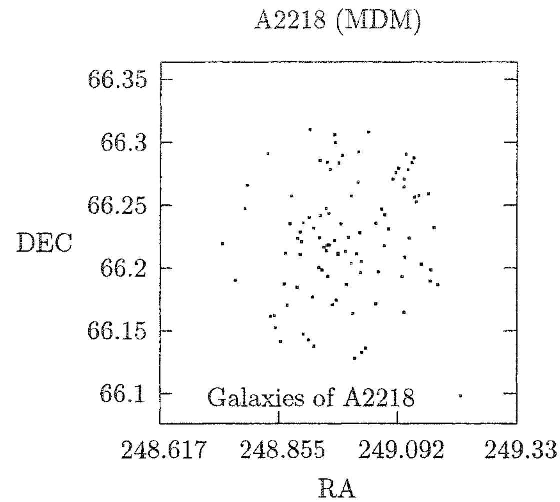

A2218 (MDM)
66.35
66.3
66.25
66.2
66.15
66.1
DEC
Galaxies of A2218
248.617
248.855
249.092
249.33
RA

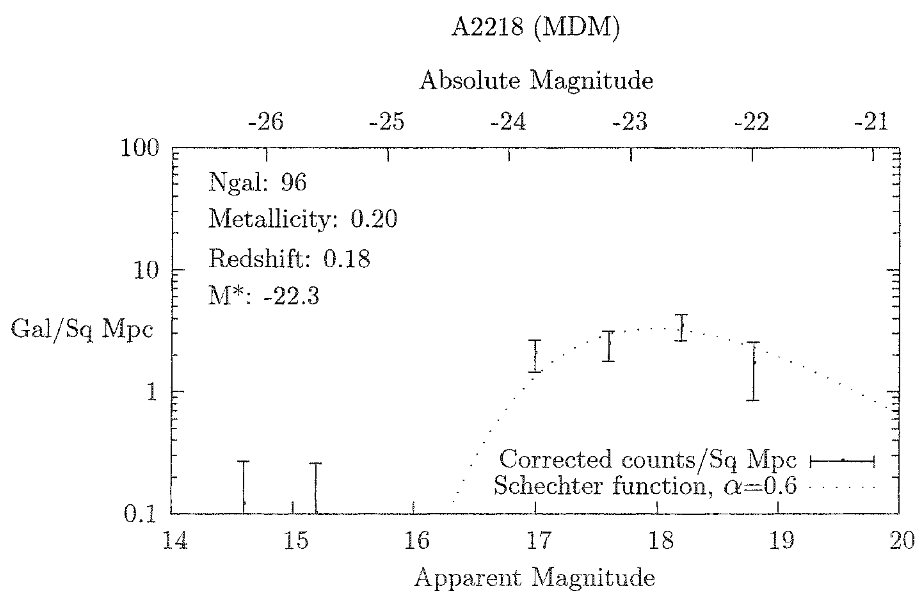

A2218 (MDM)
Absolute Magnitude
-26
-25
-24
-23
-22
-21
100
10
1
0.1
Gal/Sq Mpc
Ngal: 96
Metallicity: 0.20
Redshift: 0.18
M*: -22.3
Corrected counts/Sq Mpc
Schechter function, α=0.6
14
15
16
17
18
19
20
Apparent Magnitude

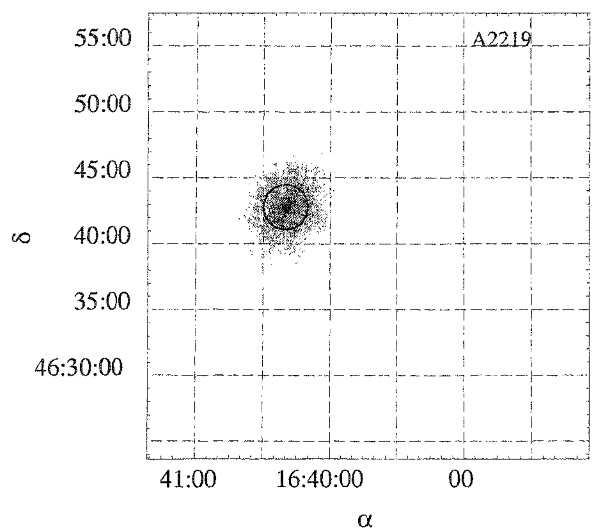
A2219
55:00
50:00
45:00
40:00
35:00
46:30:00
δ
41:00
16:40:00
00
α

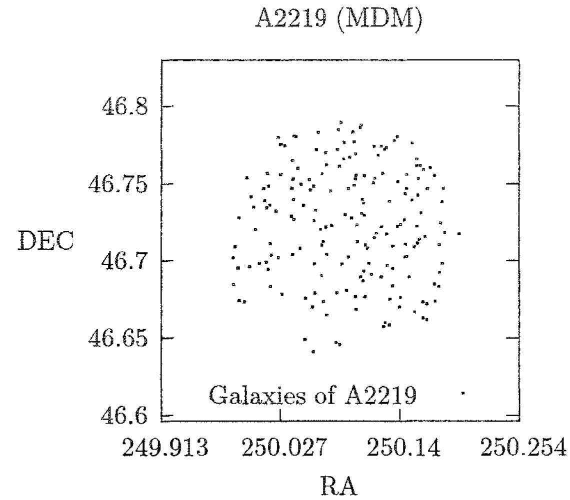
A2219 (MDM)
46.8
46.75
46.7
46.65
46.6
DEC
Galaxies of A2219
249.913
250.027
250.14
250.254
RA

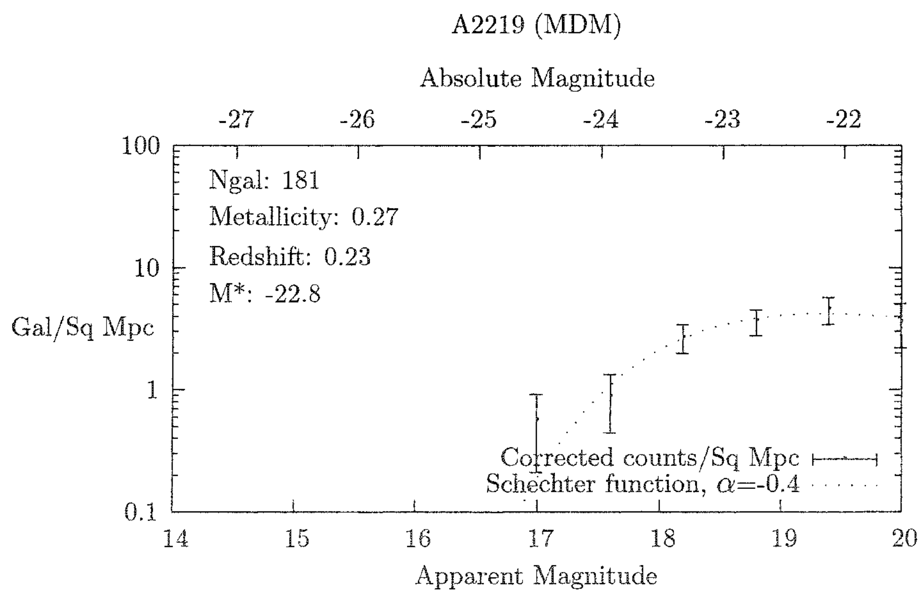
A2219 (MDM)
Absolute Magnitude
-27
-26
-25
-24
-23
-22
100
10
1
0.1
Gal/Sq Mpc
Ngal: 181
Metallicity: 0.27
Redshift: 0.23
M*: -22.8
Corrected counts/Sq Mpc
Schechter function, α=-0.4
14
15
16
17
18
19
20
Apparent Magnitude

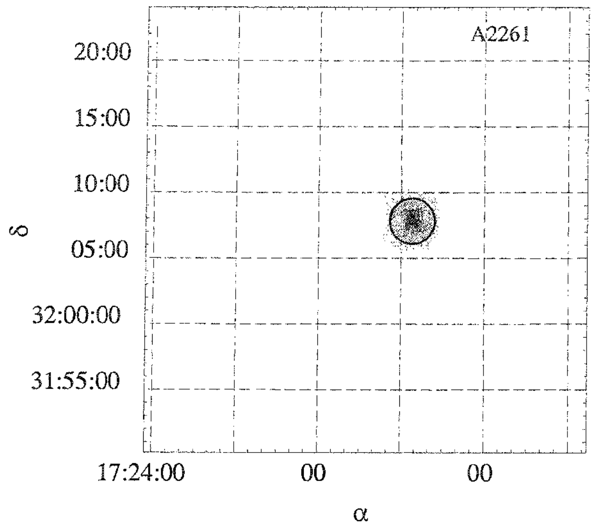

A2261 (MDM)

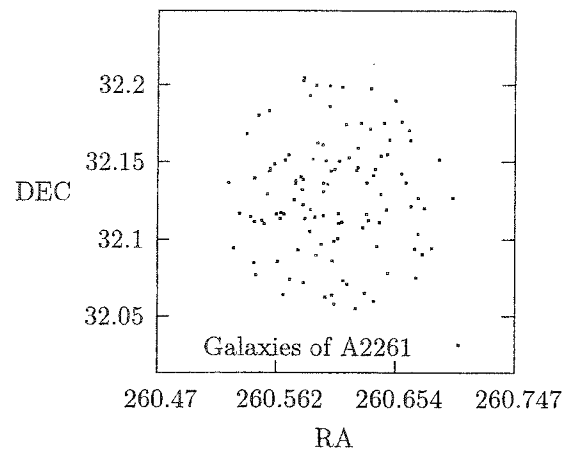

A2261 (MDM)

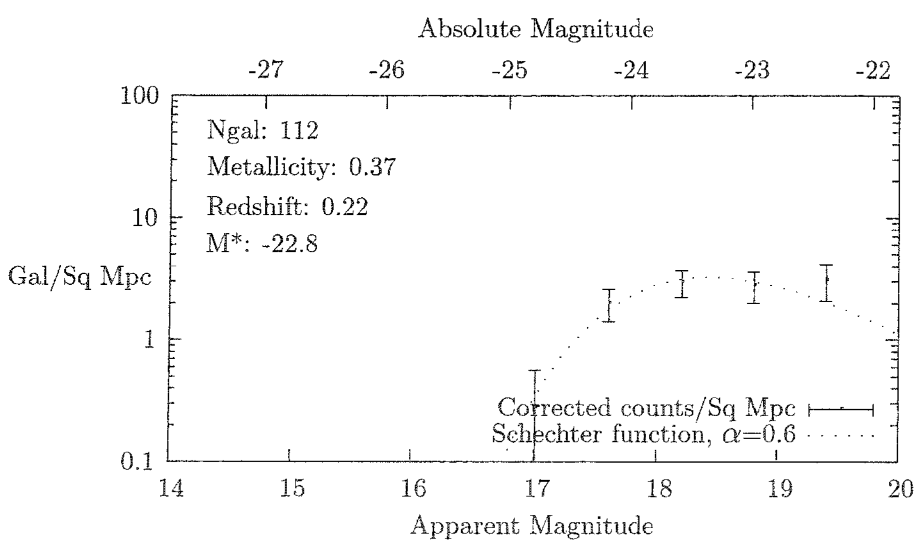

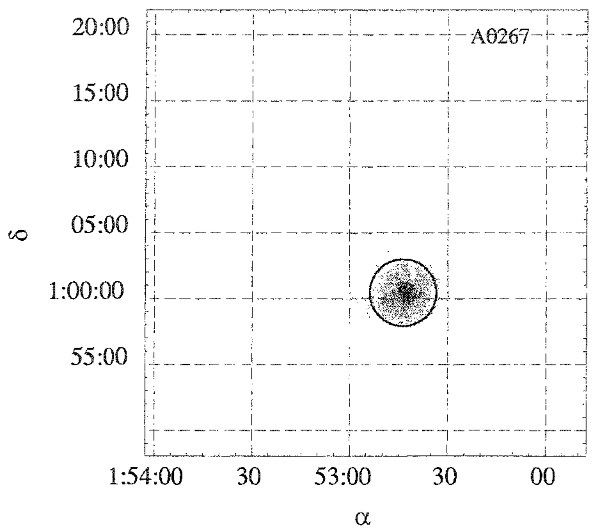

A0267 (Sloan)

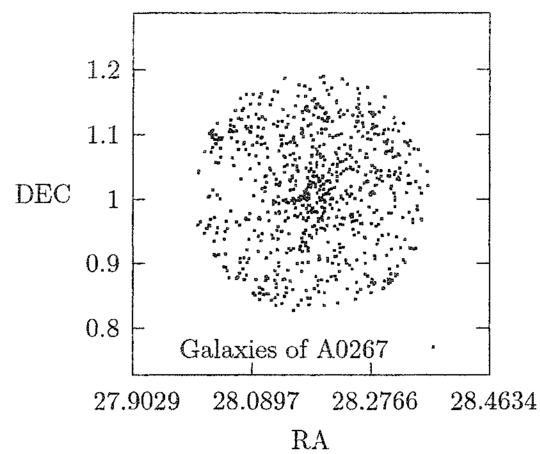

A0267 (Sloan)

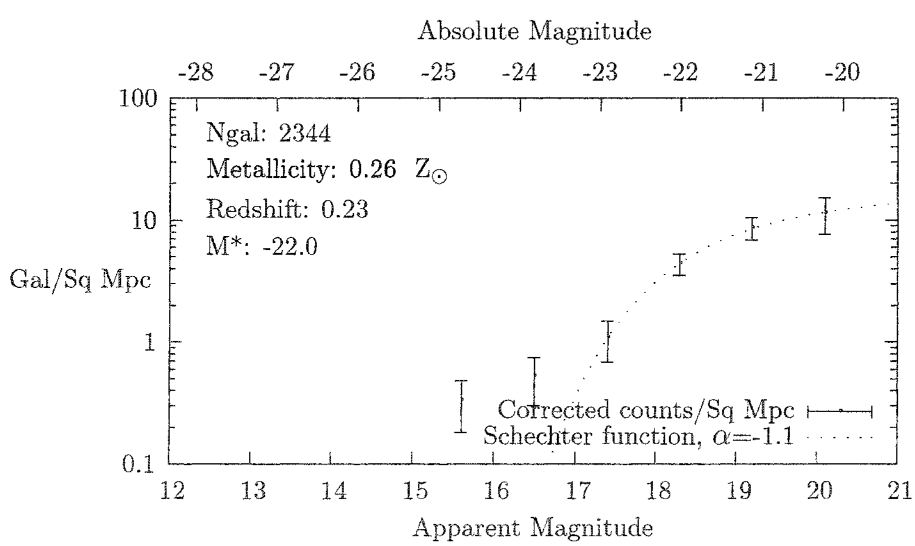

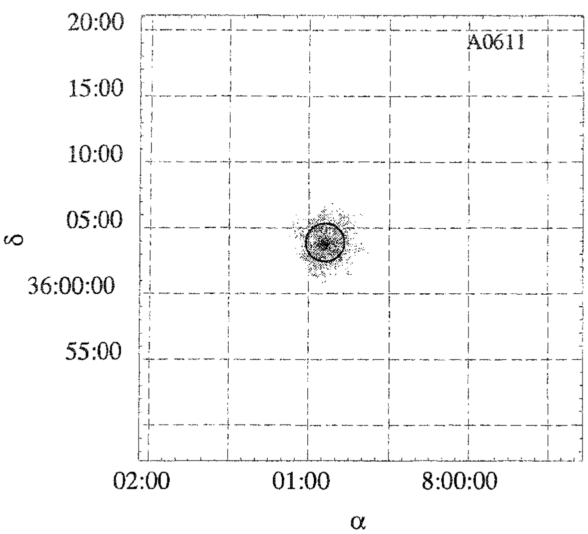
A0611
20:00
15:00
10:00
05:00
36:00:00
55:00
δ
02:00
01:00
8:00:00
α

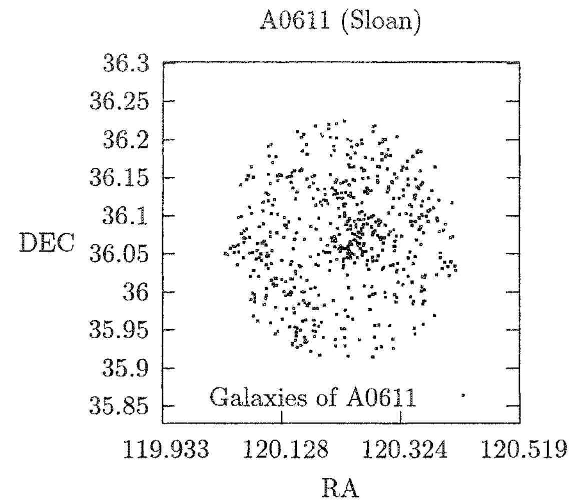
A0611 (Sloan)
DEC
RA
Galaxies of A0611
36.3
36.25
36.2
36.15
36.1
36.05
36
35.95
35.9
35.85
119.933
120.128
120.324
120.519

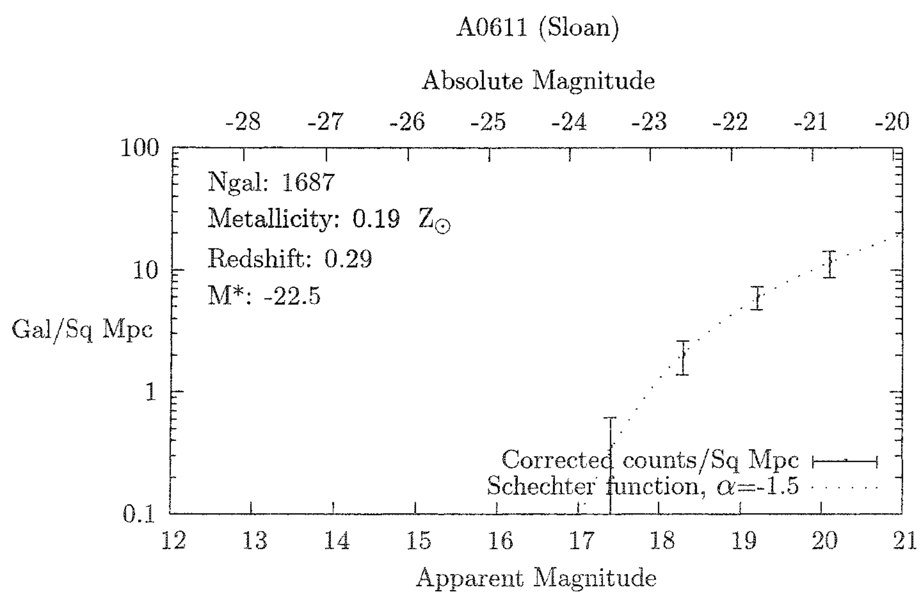
A0611 (Sloan)
Absolute Magnitude
Ngal: 1687
Metallicity: 0.19 Z⊙
Redshift: 0.29
M*: -22.5
Gal/Sq Mpc
Corrected counts/Sq Mpc
Schechter function, α=-1.5
Apparent Magnitude

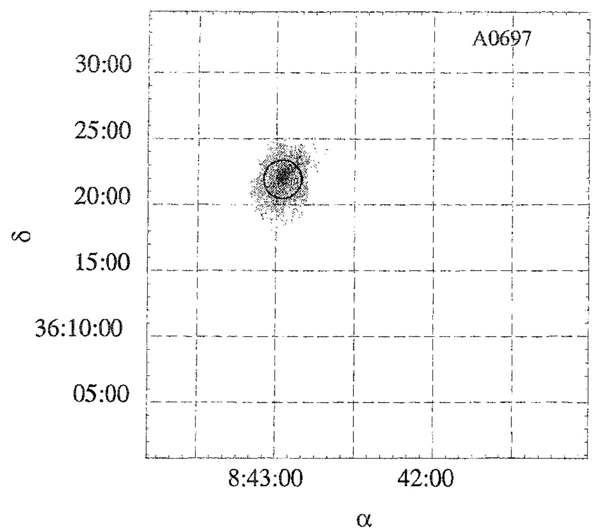
A0697
30:00
25:00
20:00
15:00
36:10:00
05:00
δ
8:43:00
42:00
α

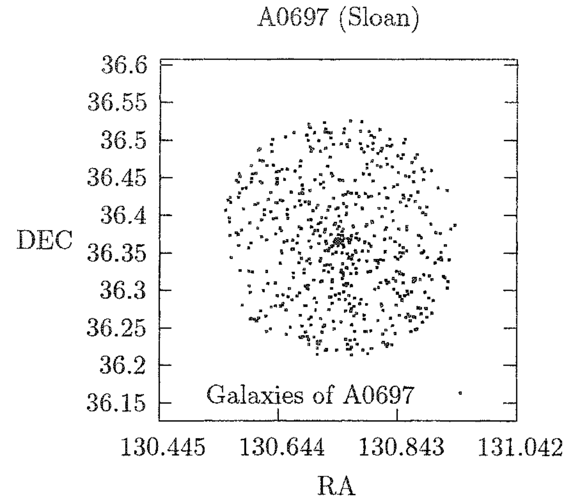
A0697 (Sloan)
DEC
36.6
36.55
36.5
36.45
36.4
36.35
36.3
36.25
36.2
36.15
Galaxies of A0697
130.445
130.644
130.843
131.042
RA

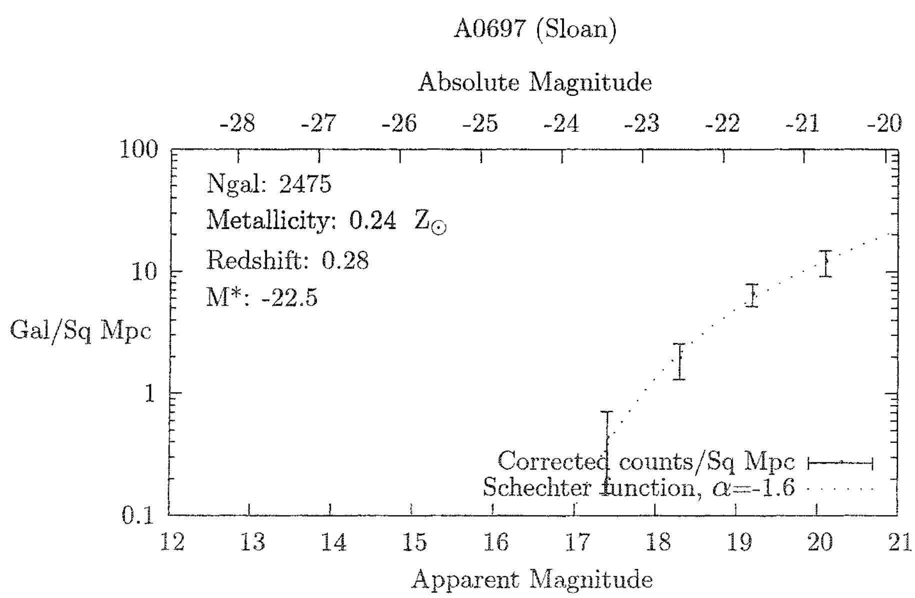
A0697 (Sloan)
Absolute Magnitude
-28
-27
-26
-25
-24
-23
-22
-21
-20
Ngal: 2475
Metallicity: 0.24 Z⊙
Redshift: 0.28
M*: -22.5
Gal/Sq Mpc
100
10
1
0.1
Corrected counts/Sq Mpc
Schechter function, α=-1.6
12
13
14
15
16
17
18
19
20
21
Apparent Magnitude

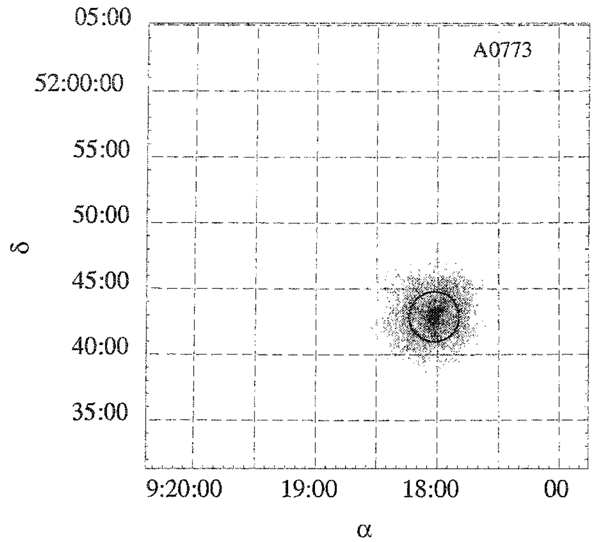
A0773
05:00
52:00:00
55:00
50:00
45:00
40:00
35:00
δ
9:20:00
19:00
18:00
00
α

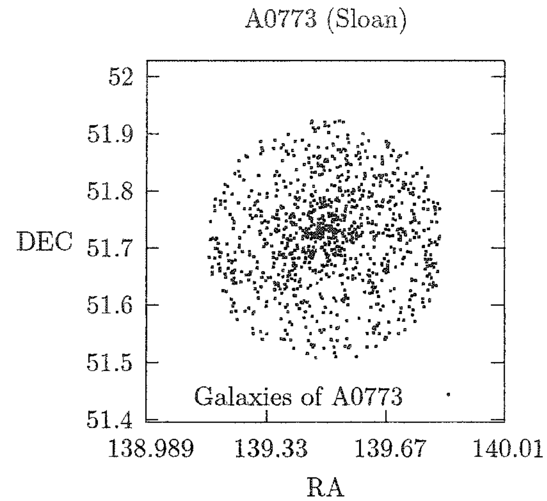
A0773 (Sloan)
DEC
52
51.9
51.8
51.7
51.6
51.5
51.4
138.989
139.33
139.67
140.01
RA
Galaxies of A0773

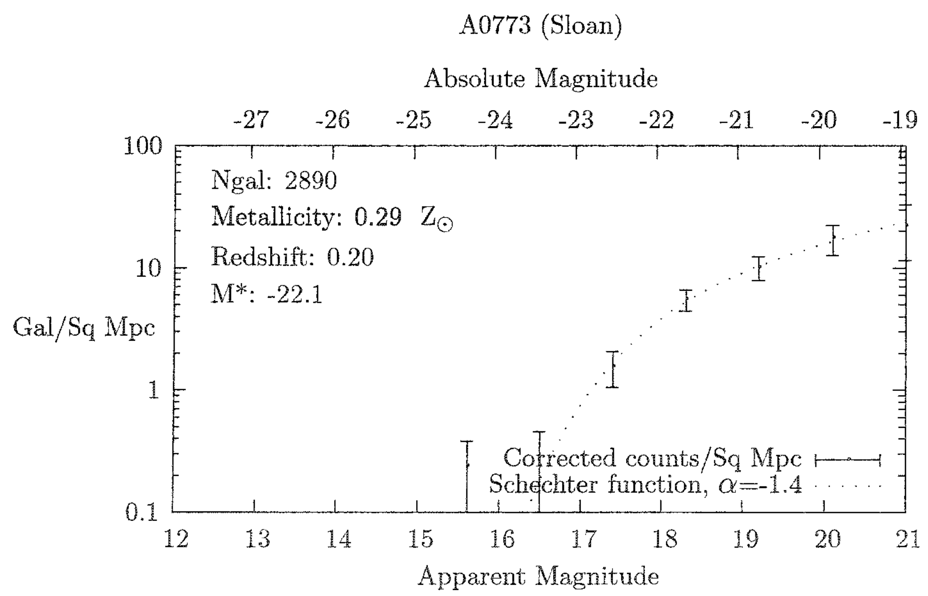
A0773 (Sloan)
Absolute Magnitude
-27 -26 -25 -24 -23 -22 -21 -20 -19
100
10
1
0.1
Gal/Sq Mpc
Ngal: 2890
Metallicity: 0.29 Z⊙
Redshift: 0.20
M*: -22.1
Corrected counts/Sq Mpc
Schechter function, α=-1.4
12 13 14 15 16 17 18 19 20 21
Apparent Magnitude

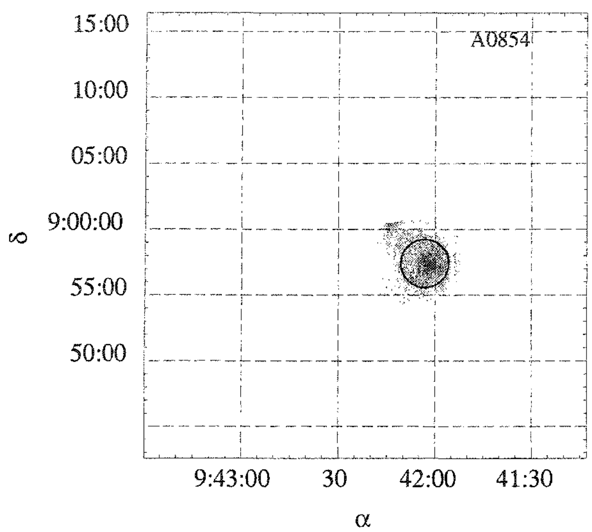
A0854
15:00
10:00
05:00
9:00:00
55:00
50:00
δ
9:43:00
30
42:00
41:30
α

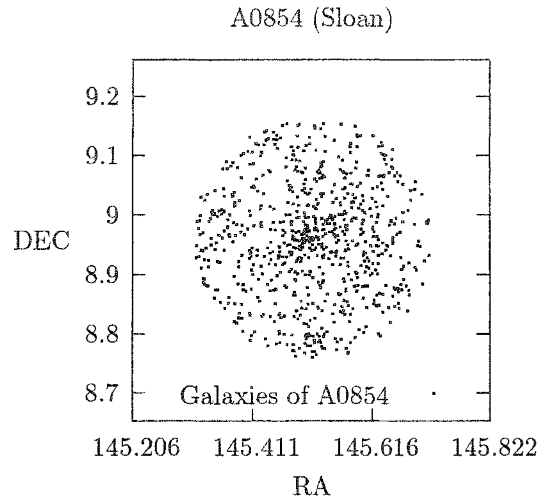
A0854 (Sloan)
DEC
9.2
9.1
9
8.9
8.8
8.7
Galaxies of A0854
145.206
145.411
145.616
145.822
RA

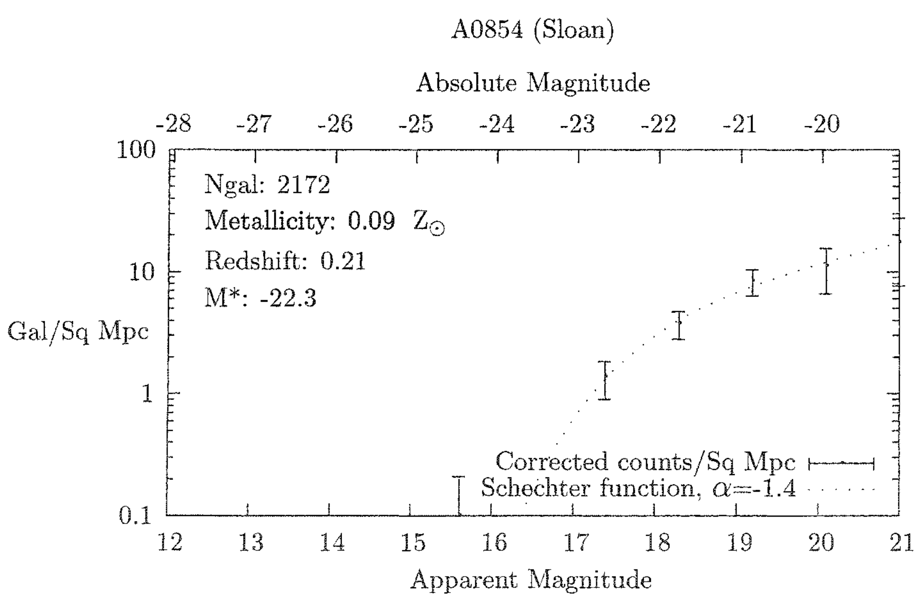
A0854 (Sloan)
Absolute Magnitude
-28
-27
-26
-25
-24
-23
-22
-21
-20
100
10
1
0.1
Gal/Sq Mpc
Ngal: 2172
Metallicity: 0.09 Z⊙
Redshift: 0.21
M*: -22.3
Corrected counts/Sq Mpc
Schechter function, α=-1.4
12
13
14
15
16
17
18
19
20
21
Apparent Magnitude

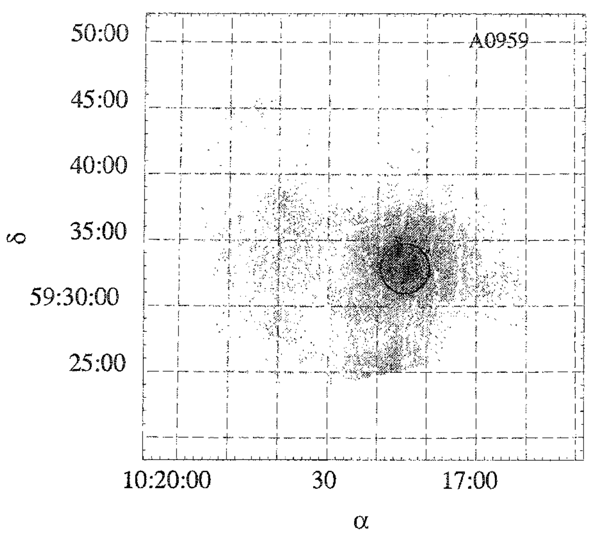

A0959
50:00
45:00
40:00
35:00
59:30:00
25:00
δ
10:20:00
30
17:00
α

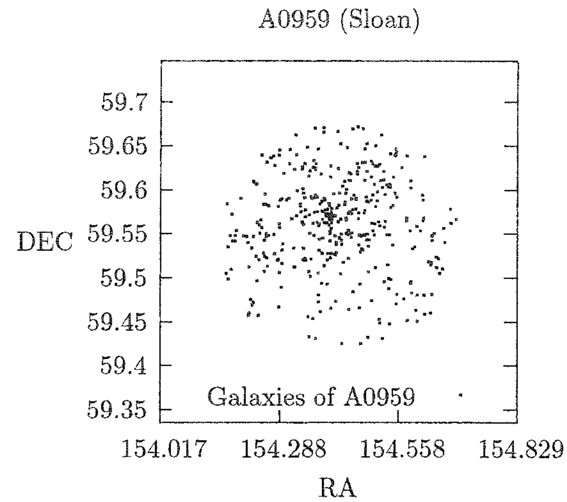

A0959 (Sloan)
DEC
59.7
59.65
59.6
59.55
59.5
59.45
59.4
59.35
Galaxies of A0959
154.017
154.288
154.558
154.829
RA

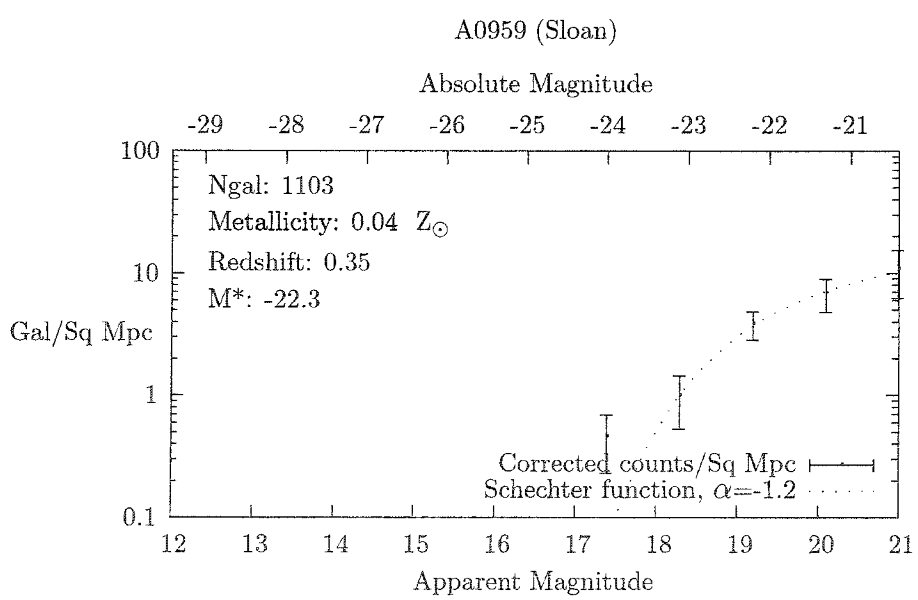

A0959 (Sloan)
Absolute Magnitude
-29
-28
-27
-26
-25
-24
-23
-22
-21
Ngal: 1103
Metallicity: 0.04 Z⊙
Redshift: 0.35
M*: -22.3
Gal/Sq Mpc
100
10
1
0.1
Corrected counts/Sq Mpc
Schechter function, α=-1.2
12
13
14
15
16
17
18
19
20
21
Apparent Magnitude

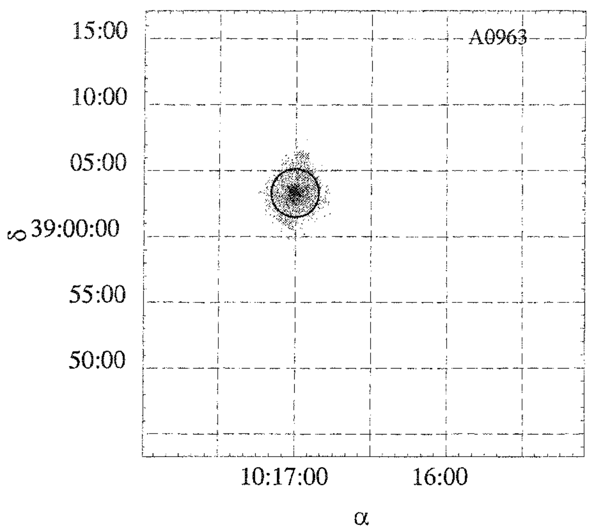
A0963
15:00
10:00
05:00
δ 39:00:00
55:00
50:00
10:17:00
16:00
α

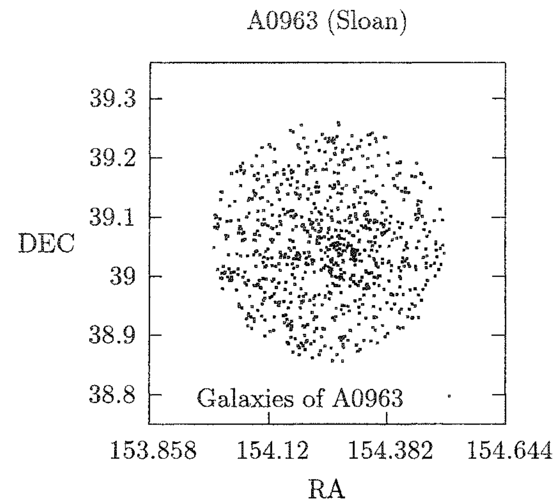
A0963 (Sloan)
DEC
39.3
39.2
39.1
39
38.9
38.8
Galaxies of A0963
153.858
154.12
154.382
154.644
RA

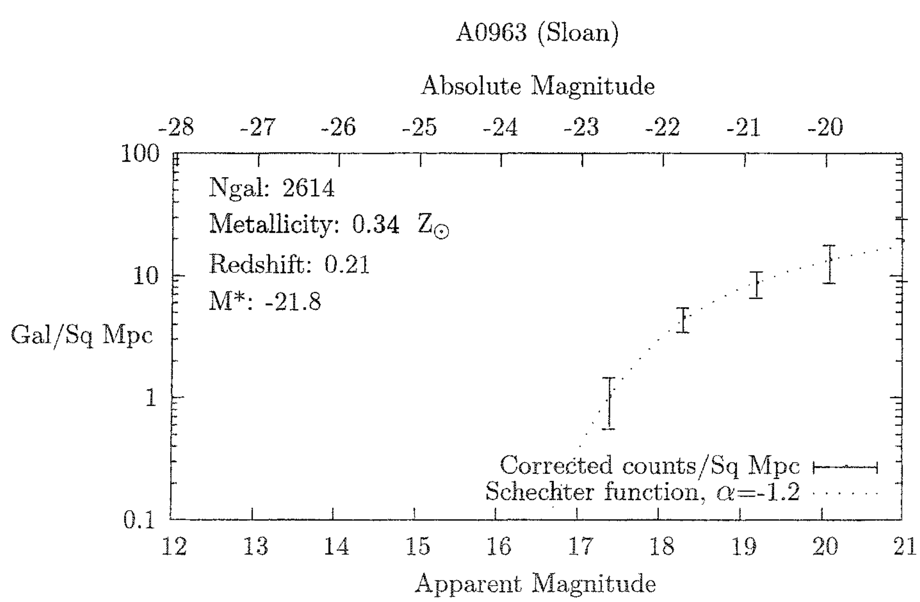
A0963 (Sloan)
Absolute Magnitude
-28 -27 -26 -25 -24 -23 -22 -21 -20
Ngal: 2614
Metallicity: 0.34 Z⊙
Redshift: 0.21
M*: -21.8
Gal/Sq Mpc
100
10
1
0.1
Corrected counts/Sq Mpc
Schechter function, α=-1.2
12 13 14 15 16 17 18 19 20 21
Apparent Magnitude

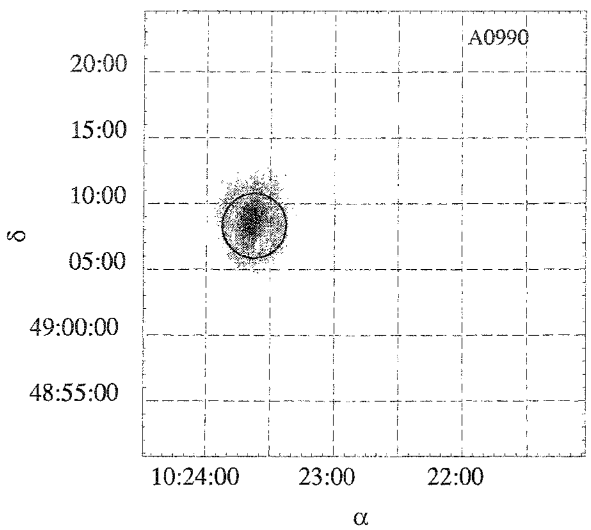
A0990
20:00
15:00
10:00
05:00
49:00:00
48:55:00
δ
10:24:00
23:00
22:00
α

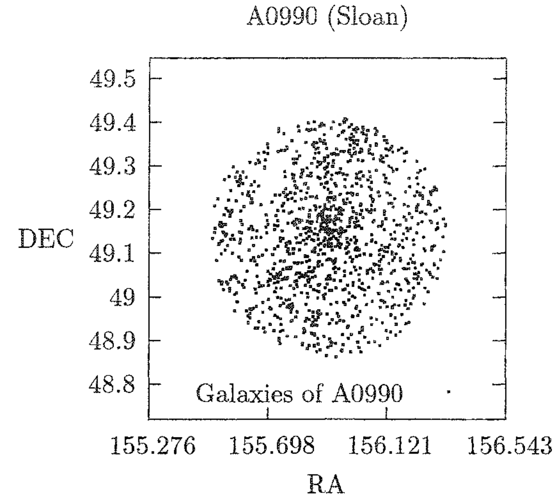
A0990 (Sloan)
49.5
49.4
49.3
49.2
49.1
49
48.9
48.8
DEC
Galaxies of A0990
155.276
155.698
156.121
156.543
RA

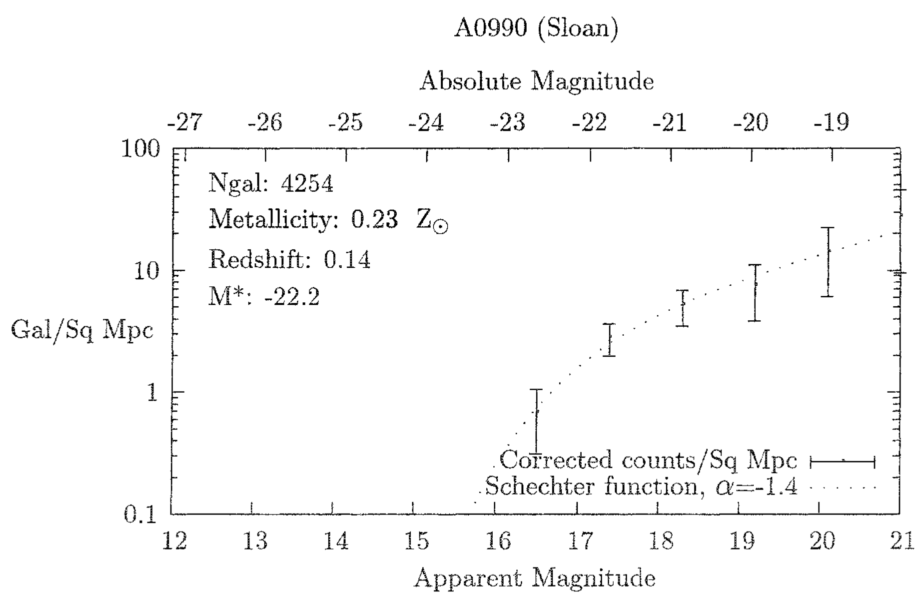
A0990 (Sloan)
Absolute Magnitude
-27 -26 -25 -24 -23 -22 -21 -20 -19
Ngal: 4254
Metallicity: 0.23 Z⊙
Redshift: 0.14
M*: -22.2
100
10
1
0.1
Gal/Sq Mpc
Corrected counts/Sq Mpc
Schechter function, α=-1.4
12 13 14 15 16 17 18 19 20 21
Apparent Magnitude

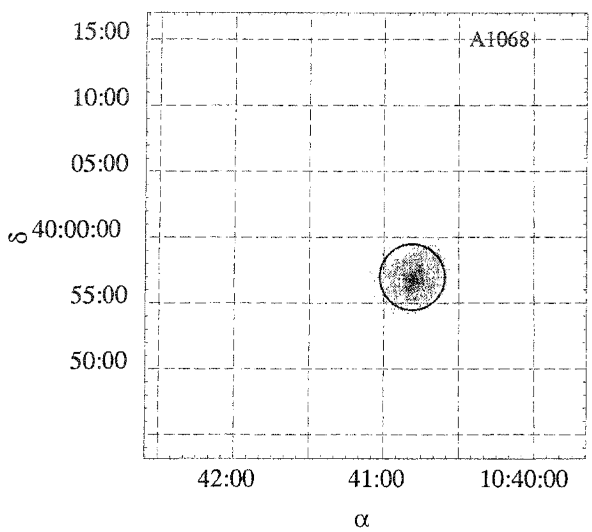
A1068
15:00
10:00
05:00
δ 40:00:00
55:00
50:00
42:00
41:00
10:40:00
α

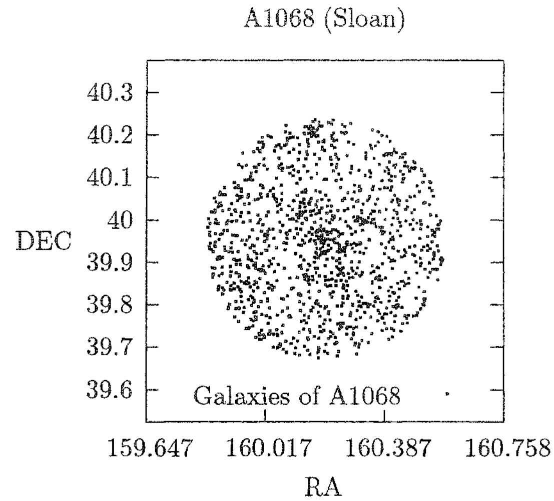
A1068 (Sloan)
40.3
40.2
40.1
40
39.9
39.8
39.7
39.6
DEC
Galaxies of A1068
159.647
160.017
160.387
160.758
RA

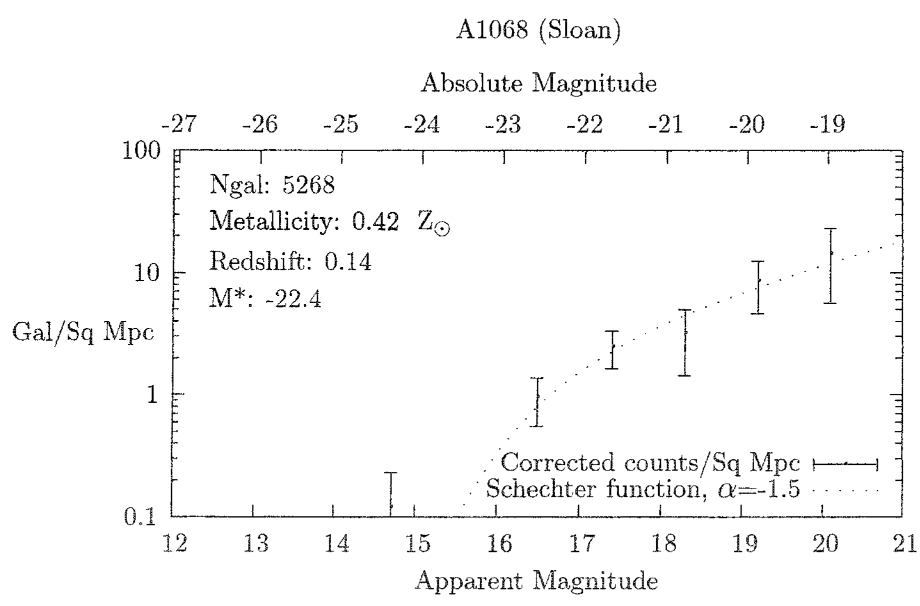
A1068 (Sloan)
Absolute Magnitude
-27
-26
-25
-24
-23
-22
-21
-20
-19
100
10
1
0.1
Gal/Sq Mpc
Ngal: 5268
Metallicity: 0.42 Z⊙
Redshift: 0.14
M*: -22.4
Corrected counts/Sq Mpc
Schechter function, α=-1.5
12
13
14
15
16
17
18
19
20
21
Apparent Magnitude

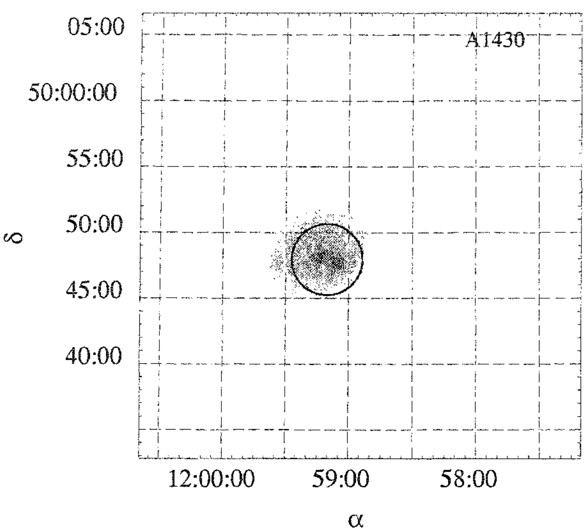
A1430
05:00
50:00:00
55:00
50:00
45:00
40:00
δ
12:00:00
59:00
58:00
α

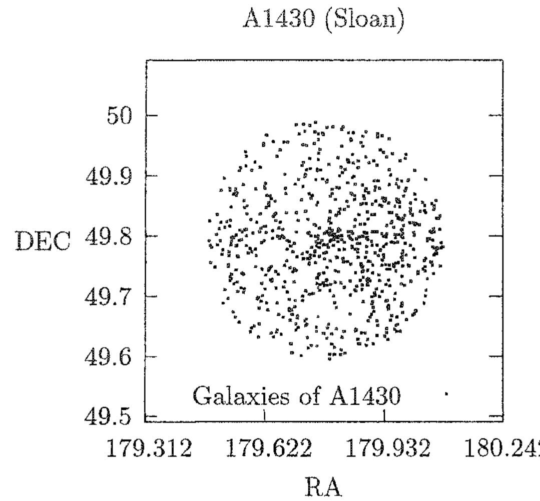
A1430 (Sloan)
DEC
RA
Galaxies of A1430
50
49.9
49.8
49.7
49.6
49.5
179.312
179.622
179.932
180.242

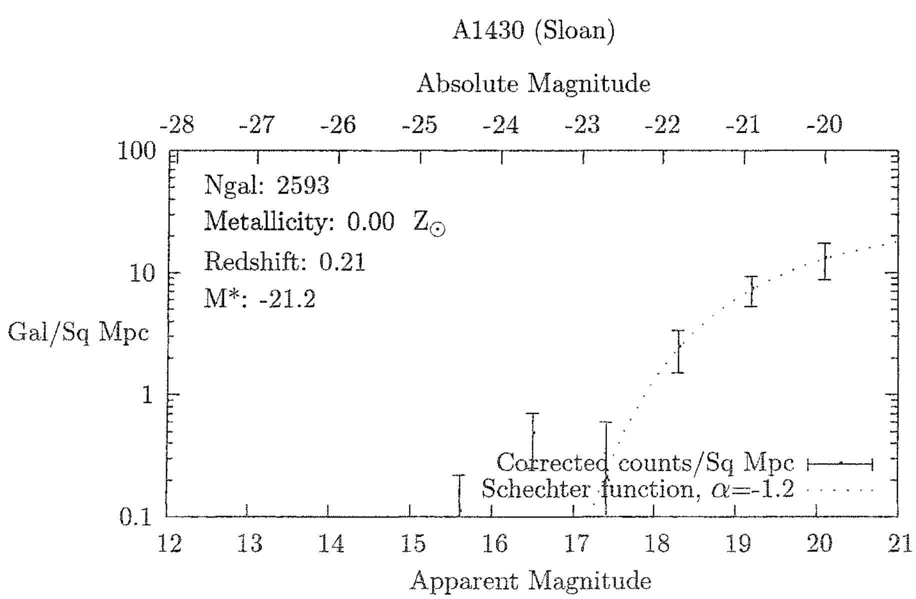
A1430 (Sloan)
Absolute Magnitude
Ngal: 2593
Metallicity: 0.00 Z⊙
Redshift: 0.21
M*: -21.2
Gal/Sq Mpc
Corrected counts/Sq Mpc
Schechter function, α=-1.2
Apparent Magnitude

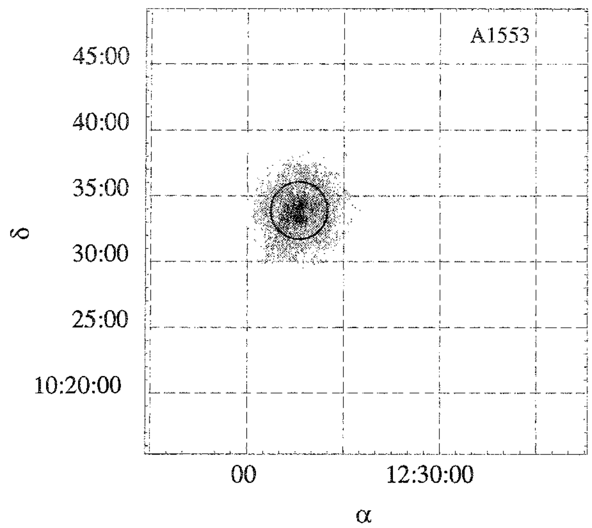

A1553
45:00
40:00
35:00
30:00
25:00
10:20:00
δ
00
12:30:00
α

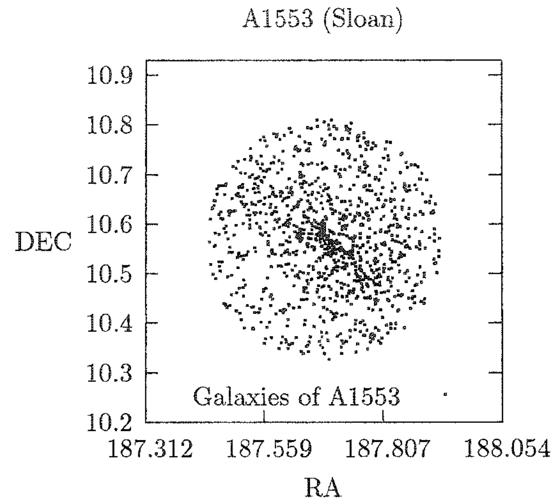

A1553 (Sloan)
10.9
10.8
10.7
10.6
10.5
10.4
10.3
10.2
DEC
Galaxies of A1553
187.312
187.559
187.807
188.054
RA

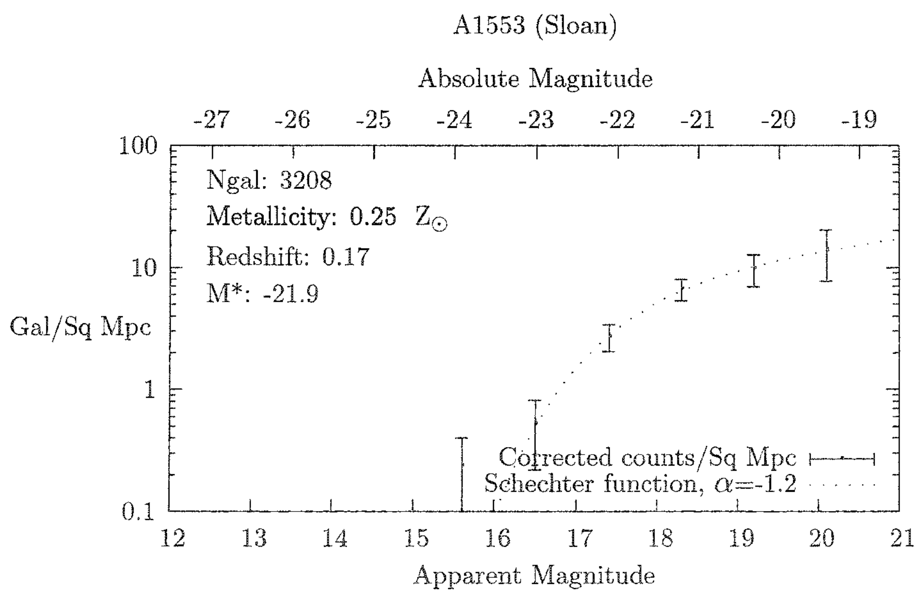

A1553 (Sloan)
Absolute Magnitude
-27
-26
-25
-24
-23
-22
-21
-20
-19
Ngal: 3208
Metallicity: 0.25 Z⊙
Redshift: 0.17
M*: -21.9
100
10
1
0.1
Gal/Sq Mpc
Corrected counts/Sq Mpc
Schechter function, α=-1.2
12
13
14
15
16
17
18
19
20
21
Apparent Magnitude

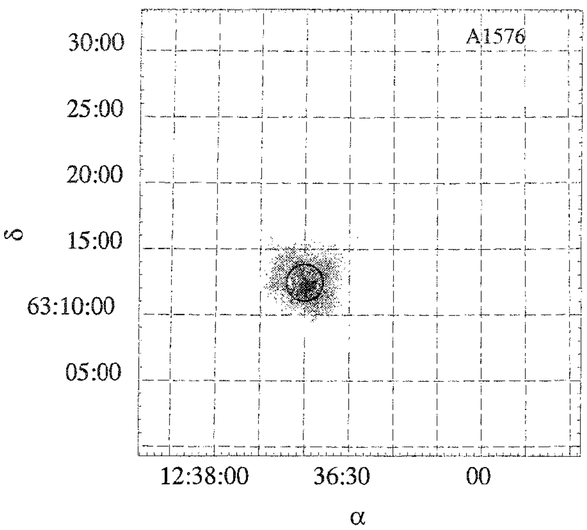
A1576
30:00
25:00
20:00
15:00
63:10:00
05:00
δ
12:38:00
36:30
00
α

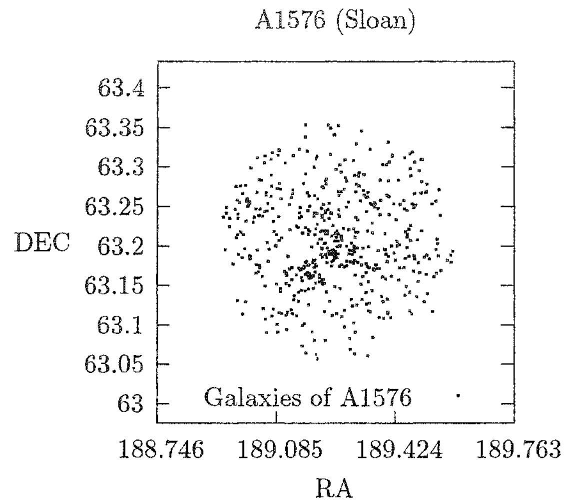
A1576 (Sloan)
63.4
63.35
63.3
63.25
63.2
63.15
63.1
63.05
63
DEC
Galaxies of A1576
188.746
189.085
189.424
189.763
RA

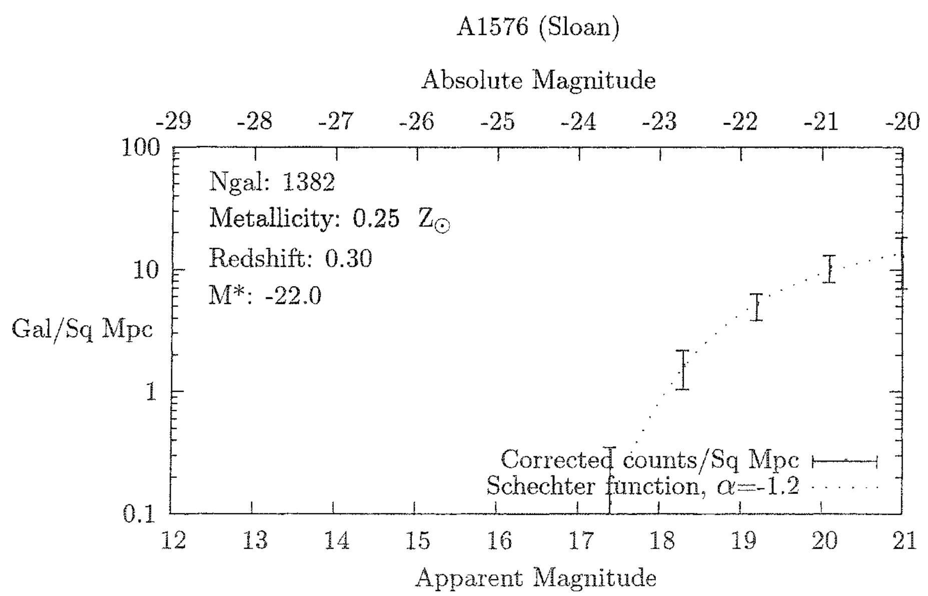
A1576 (Sloan)
Absolute Magnitude
-29
-28
-27
-26
-25
-24
-23
-22
-21
-20
100
10
1
0.1
Gal/Sq Mpc
Ngal: 1382
Metallicity: 0.25 Z⊙
Redshift: 0.30
M*: -22.0
Corrected counts/Sq Mpc
Schechter function, α=-1.2
12
13
14
15
16
17
18
19
20
21
Apparent Magnitude

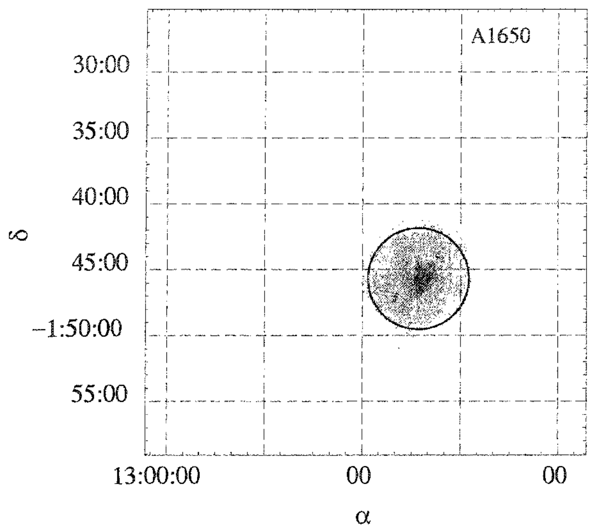
A1650
30:00
35:00
40:00
45:00
−1:50:00
55:00
δ
13:00:00
00
00
α

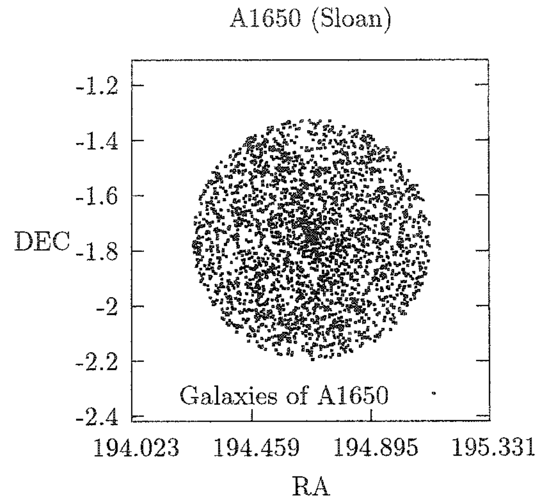
A1650 (Sloan)
-1.2
-1.4
-1.6
DEC -1.8
-2
-2.2
-2.4
Galaxies of A1650
194.023
194.459
194.895
195.331
RA

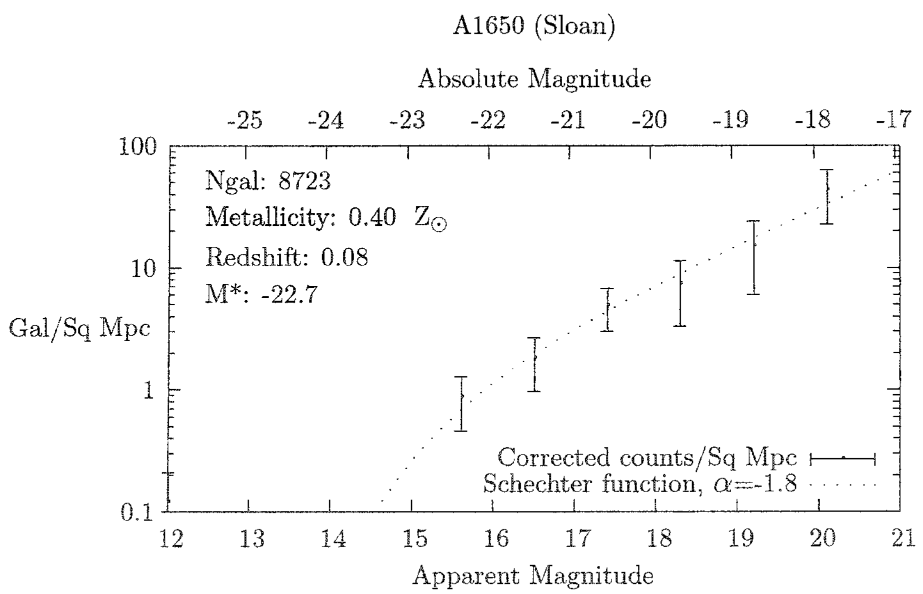
A1650 (Sloan)
Absolute Magnitude
-25 -24 -23 -22 -21 -20 -19 -18 -17
Ngal: 8723
Metallicity: 0.40 Z⊙
Redshift: 0.08
M*: -22.7
100
10
Gal/Sq Mpc
1
0.1
Corrected counts/Sq Mpc
Schechter function, α=-1.8
12 13 14 15 16 17 18 19 20 21
Apparent Magnitude

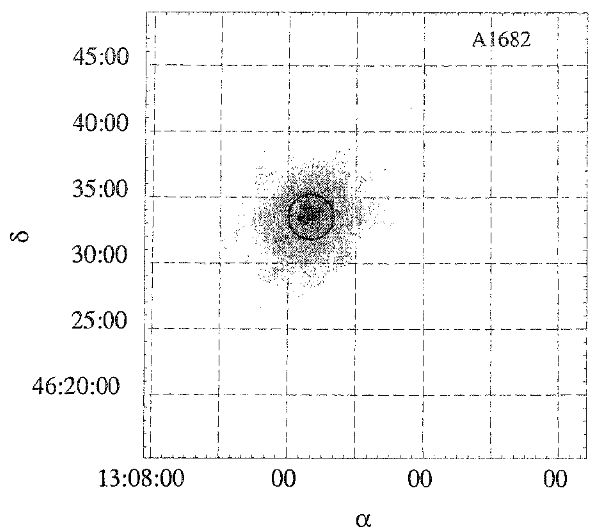
A1682
45:00
40:00
35:00
30:00
25:00
46:20:00
13:08:00
00
00
00
α
δ

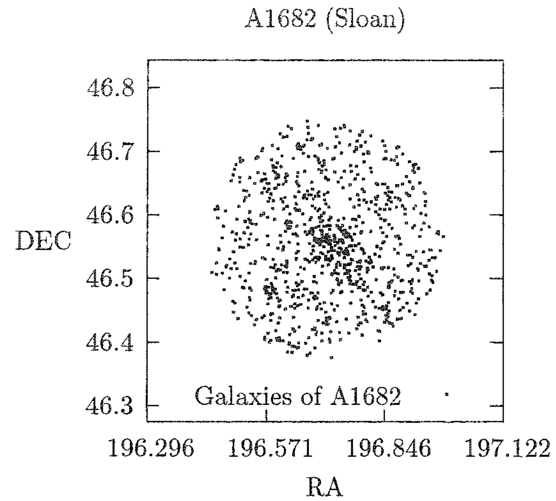
A1682 (Sloan)
46.8
46.7
46.6
46.5
46.4
46.3
DEC
Galaxies of A1682
196.296
196.571
196.846
197.122
RA

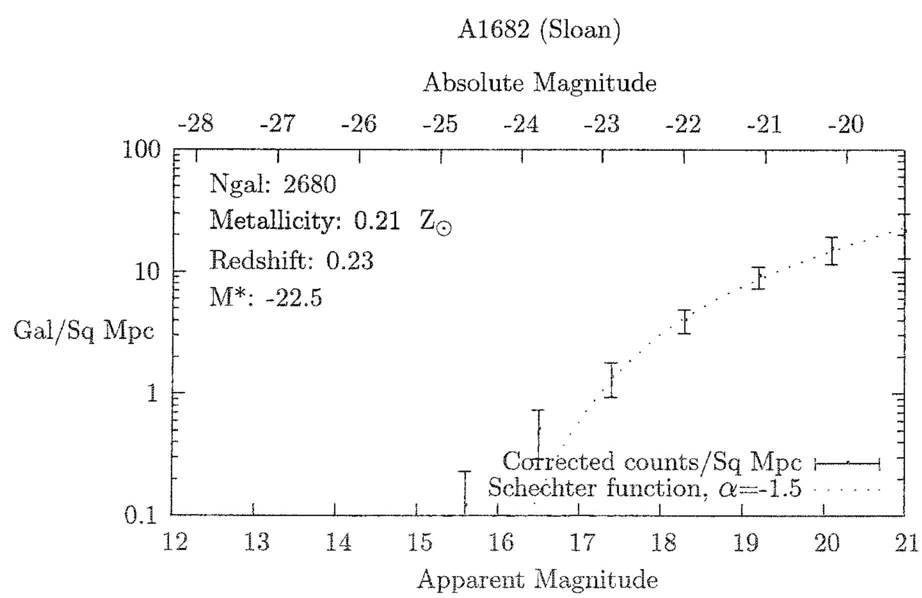
A1682 (Sloan)
Absolute Magnitude
-28 -27 -26 -25 -24 -23 -22 -21 -20
Ngal: 2680
Metallicity: 0.21 Z⊙
Redshift: 0.23
M*: -22.5
Gal/Sq Mpc
100
10
1
0.1
Corrected counts/Sq Mpc
Schechter function, α=-1.5
12 13 14 15 16 17 18 19 20 21
Apparent Magnitude

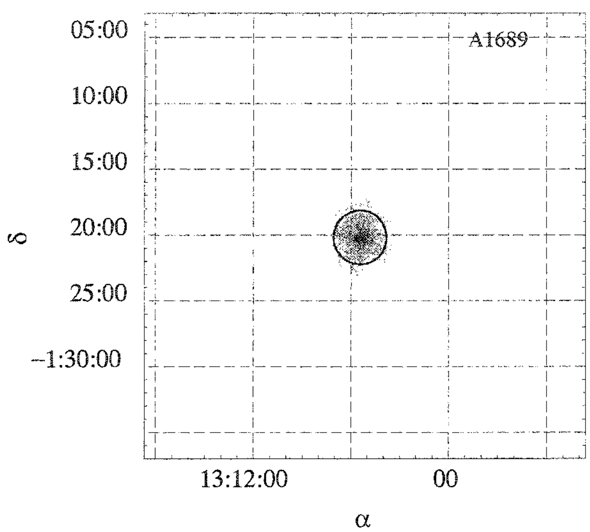
A1689
05:00
10:00
15:00
20:00
25:00
−1:30:00
δ
13:12:00
00
α

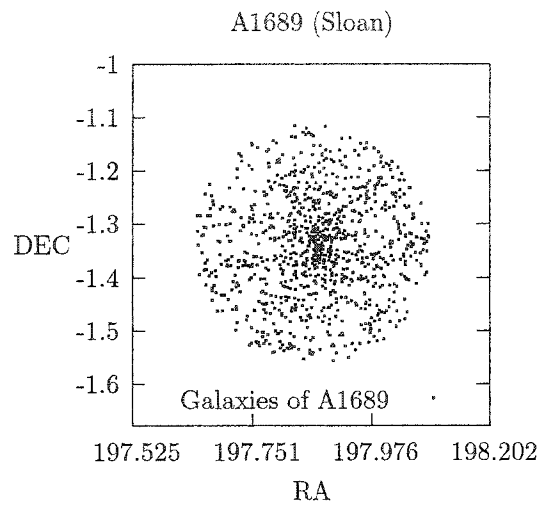
A1689 (Sloan)
-1
-1.1
-1.2
-1.3
-1.4
-1.5
-1.6
DEC
Galaxies of A1689
197.525
197.751
197.976
198.202
RA

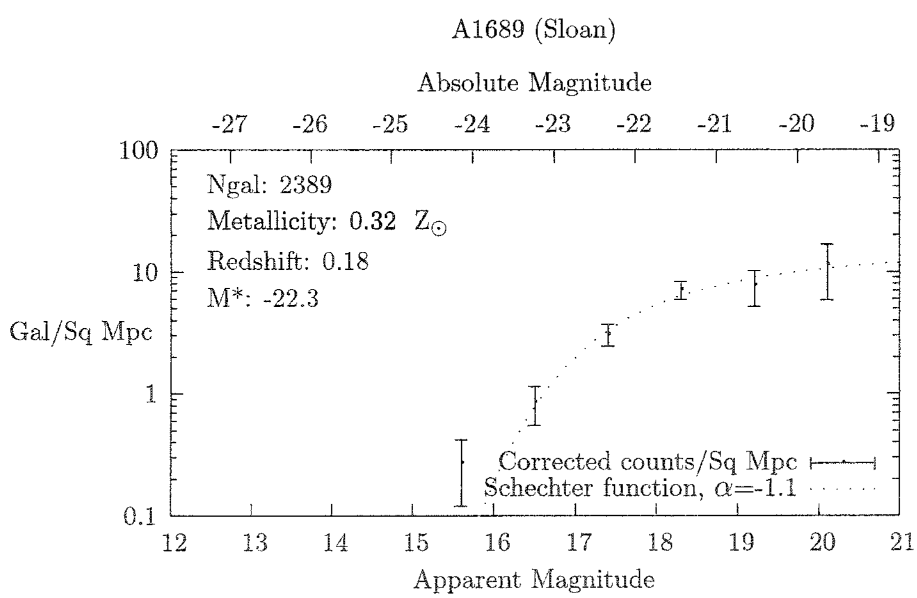
A1689 (Sloan)
Absolute Magnitude
-27 -26 -25 -24 -23 -22 -21 -20 -19
Ngal: 2389
Metallicity: 0.32 Z⊙
Redshift: 0.18
M*: -22.3
100
10
1
0.1
Gal/Sq Mpc
Corrected counts/Sq Mpc
Schechter function, α=-1.1
12 13 14 15 16 17 18 19 20 21
Apparent Magnitude

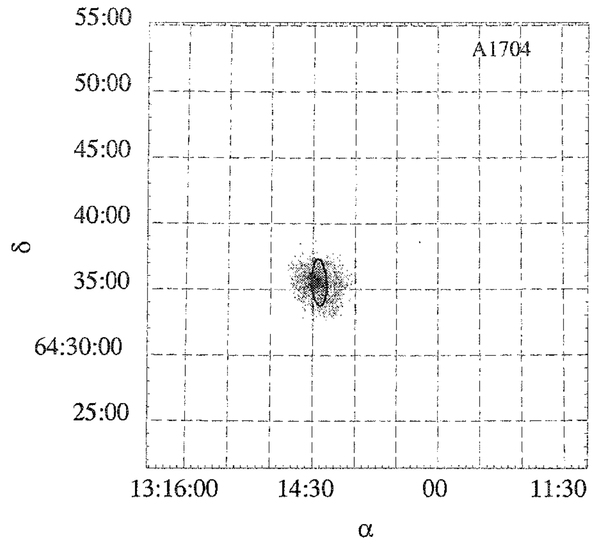
A1704
55:00
50:00
45:00
40:00
35:00
64:30:00
25:00
δ
13:16:00
14:30
00
11:30
α

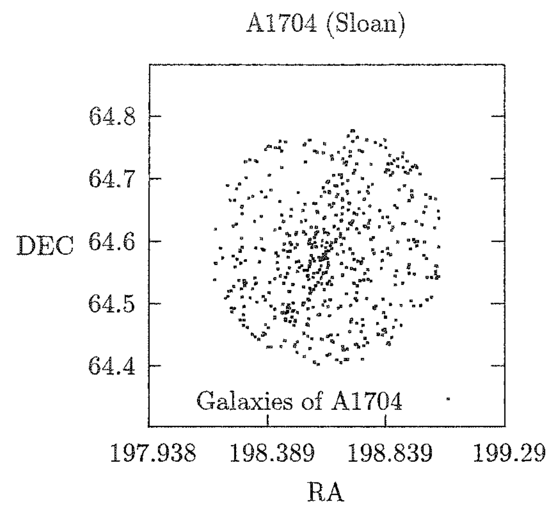
A1704 (Sloan)
DEC
64.8
64.7
64.6
64.5
64.4
Galaxies of A1704
197.938
198.389
198.839
199.29
RA

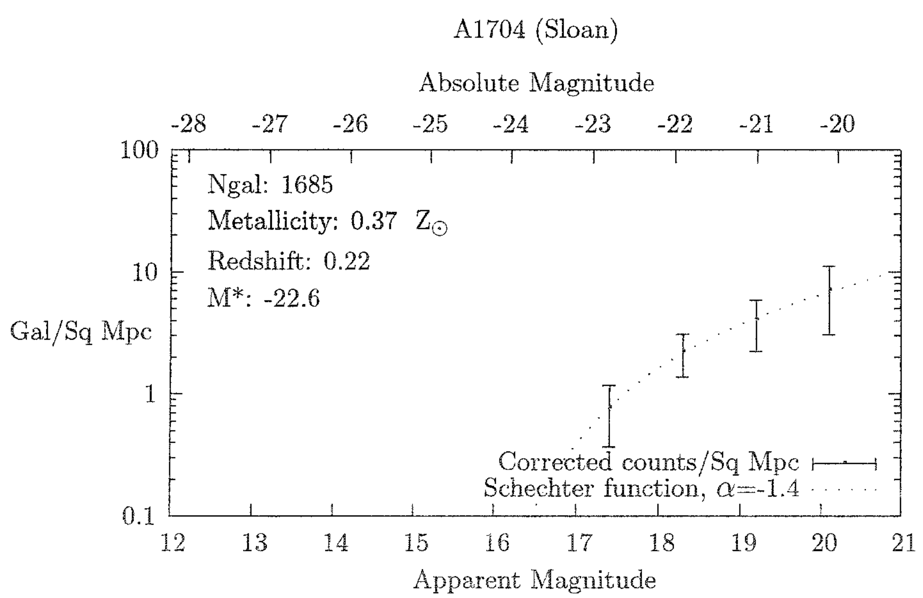
A1704 (Sloan)
Absolute Magnitude
-28 -27 -26 -25 -24 -23 -22 -21 -20
Ngal: 1685
Metallicity: 0.37 Z⊙
Redshift: 0.22
M*: -22.6
Gal/Sq Mpc
100
10
1
0.1
Corrected counts/Sq Mpc
Schechter function, α=-1.4
12 13 14 15 16 17 18 19 20 21
Apparent Magnitude

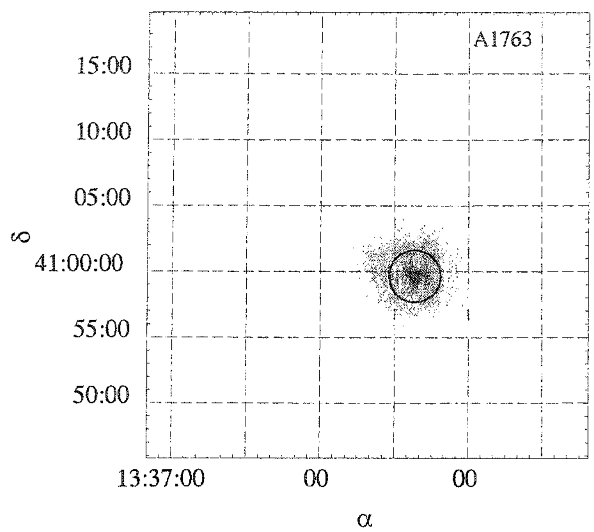
A1763
15:00
10:00
05:00
δ
41:00:00
55:00
50:00
13:37:00
00
00
α

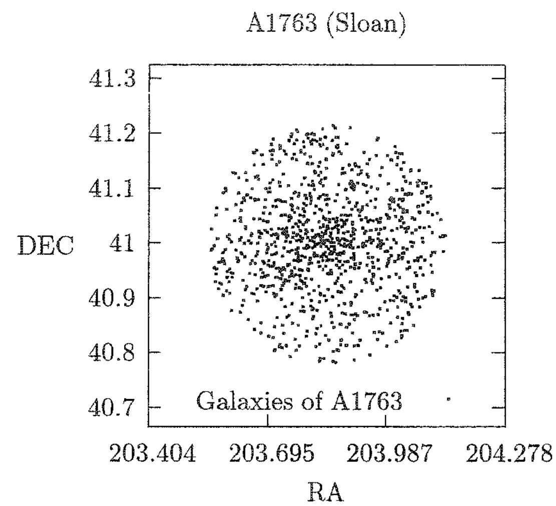
A1763 (Sloan)
41.3
41.2
41.1
DEC
41
40.9
40.8
40.7
Galaxies of A1763
203.404
203.695
203.987
204.278
RA

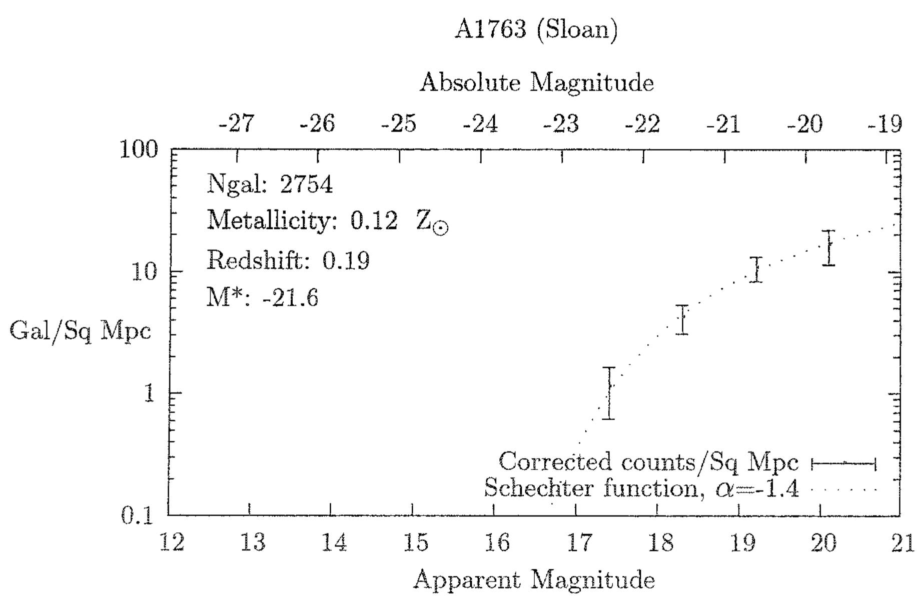
A1763 (Sloan)
Absolute Magnitude
-27
-26
-25
-24
-23
-22
-21
-20
-19
100
10
1
0.1
Gal/Sq Mpc
Ngal: 2754
Metallicity: 0.12 Z⊙
Redshift: 0.19
M*: -21.6
Corrected counts/Sq Mpc
Schechter function, α=-1.4
12
13
14
15
16
17
18
19
20
21
Apparent Magnitude

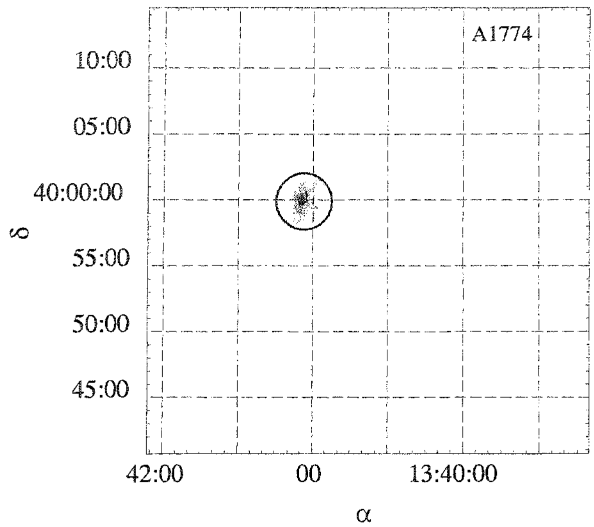
A1774
10:00
05:00
40:00:00
55:00
50:00
45:00
δ
42:00
00
13:40:00
α

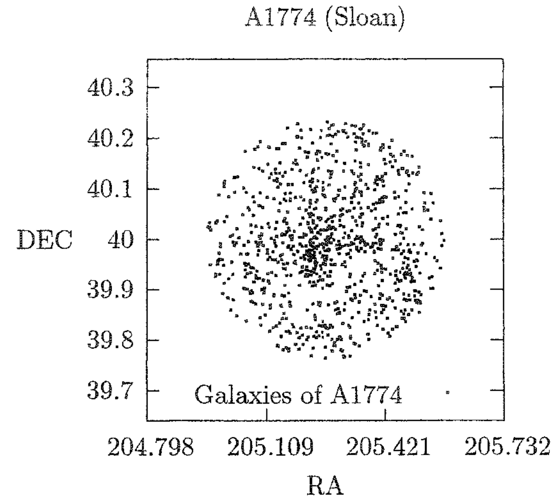
A1774 (Sloan)
40.3
40.2
40.1
40
39.9
39.8
39.7
DEC
Galaxies of A1774
204.798
205.109
205.421
205.732
RA

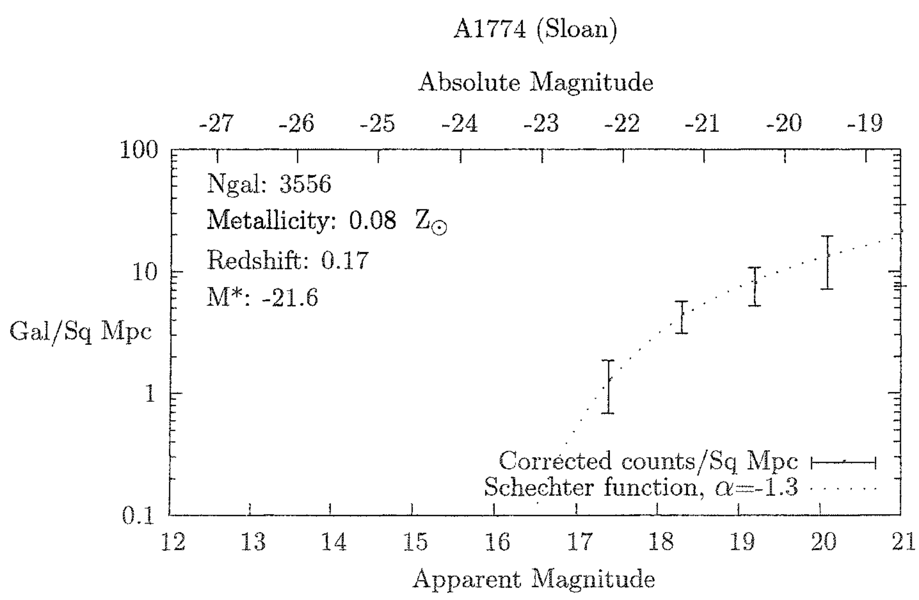
A1774 (Sloan)
Absolute Magnitude
-27
-26
-25
-24
-23
-22
-21
-20
-19
100
10
1
0.1
Gal/Sq Mpc
Ngal: 3556
Metallicity: 0.08 Z⊙
Redshift: 0.17
M*: -21.6
Corrected counts/Sq Mpc
Schechter function, α=-1.3
12
13
14
15
16
17
18
19
20
21
Apparent Magnitude

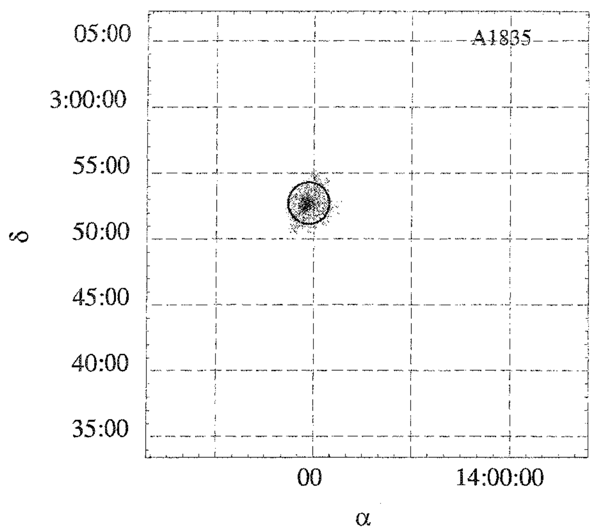

A1835
05:00
3:00:00
55:00
50:00
45:00
40:00
35:00
δ
00
14:00:00
α

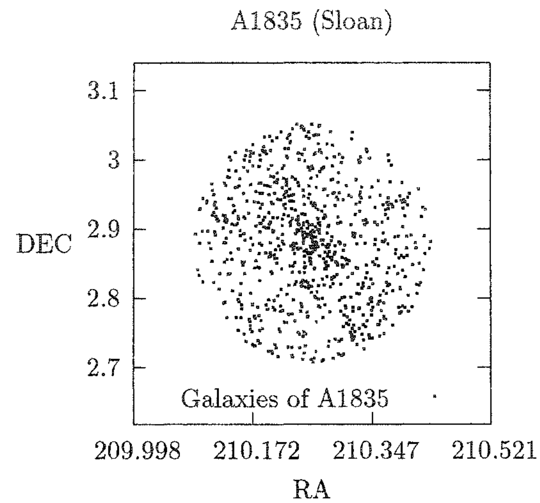

A1835 (Sloan)
3.1
3
2.9
2.8
2.7
DEC
Galaxies of A1835
209.998
210.172
210.347
210.521
RA

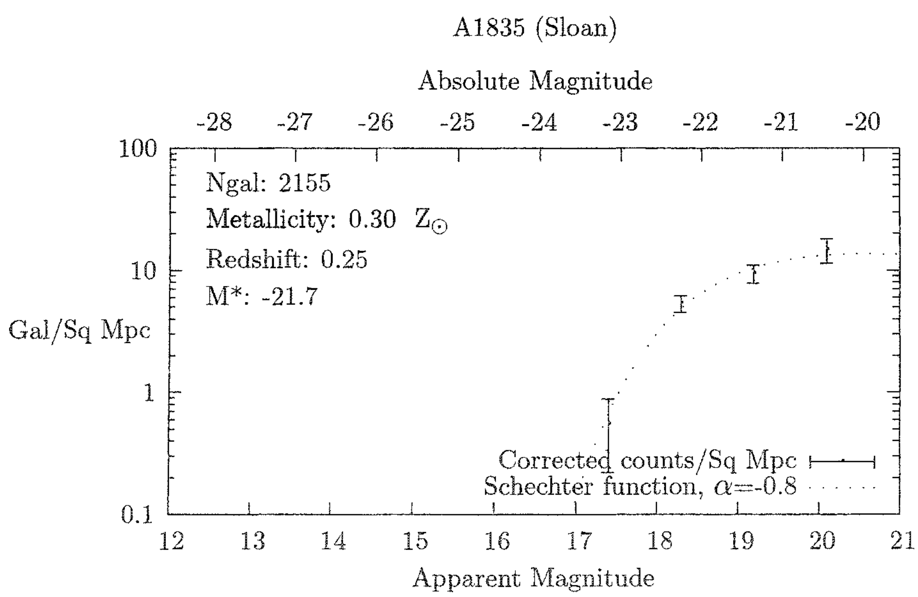

A1835 (Sloan)
Absolute Magnitude
-28
-27
-26
-25
-24
-23
-22
-21
-20
100
10
1
0.1
Gal/Sq Mpc
Ngal: 2155
Metallicity: 0.30 Z☉
Redshift: 0.25
M*: -21.7
Corrected counts/Sq Mpc
Schechter function, α=-0.8
12
13
14
15
16
17
18
19
20
21
Apparent Magnitude

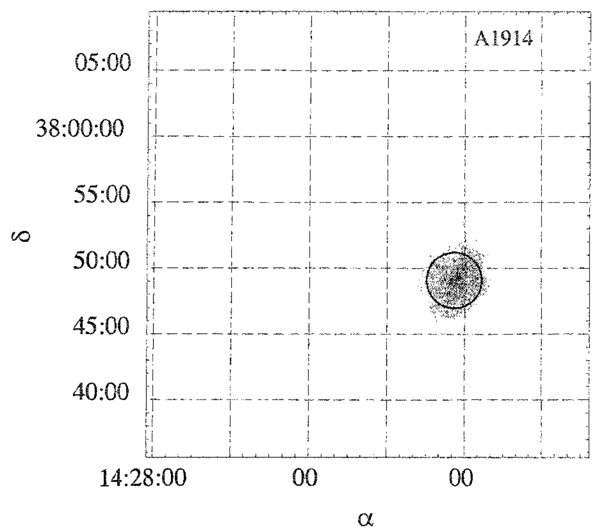
A1914
05:00
38:00:00
55:00
50:00
45:00
40:00
δ
14:28:00
00
00
α

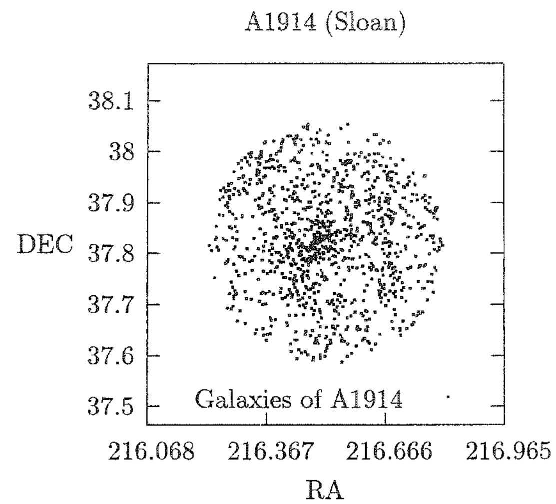
A1914 (Sloan)
38.1
38
37.9
37.8
37.7
37.6
37.5
DEC
Galaxies of A1914
216.068
216.367
216.666
216.965
RA

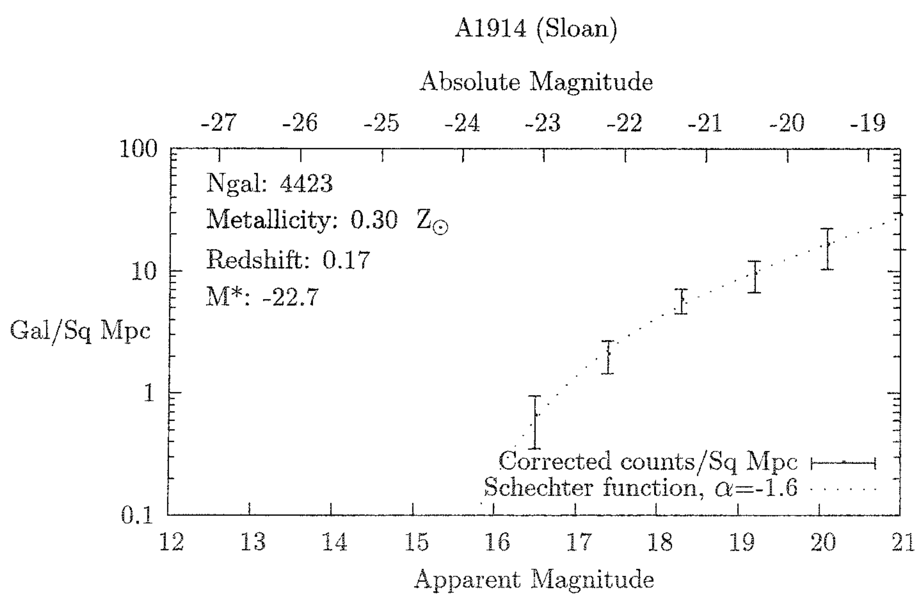
A1914 (Sloan)
Absolute Magnitude
-27
-26
-25
-24
-23
-22
-21
-20
-19
100
10
1
0.1
Gal/Sq Mpc
Ngal: 4423
Metallicity: 0.30 Z⊙
Redshift: 0.17
M*: -22.7
Corrected counts/Sq Mpc
Schechter function, α=-1.6
12
13
14
15
16
17
18
19
20
21
Apparent Magnitude

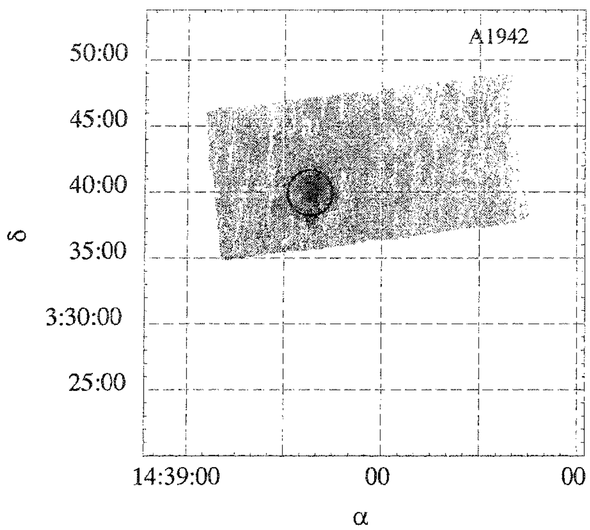
A1942
50:00
45:00
40:00
35:00
3:30:00
25:00
δ
14:39:00
00
00
α

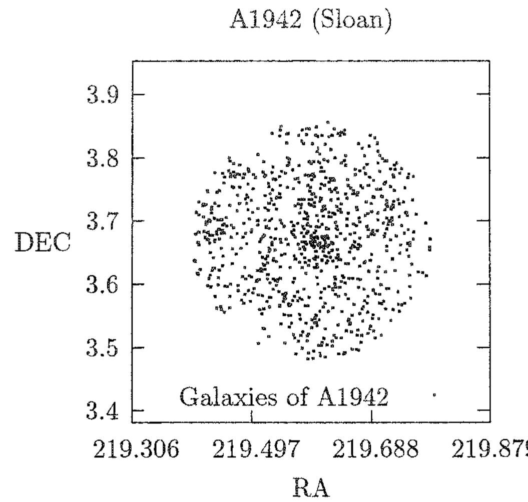
A1942 (Sloan)
3.9
3.8
3.7
3.6
3.5
3.4
DEC
Galaxies of A1942
219.306
219.497
219.688
219.879
RA

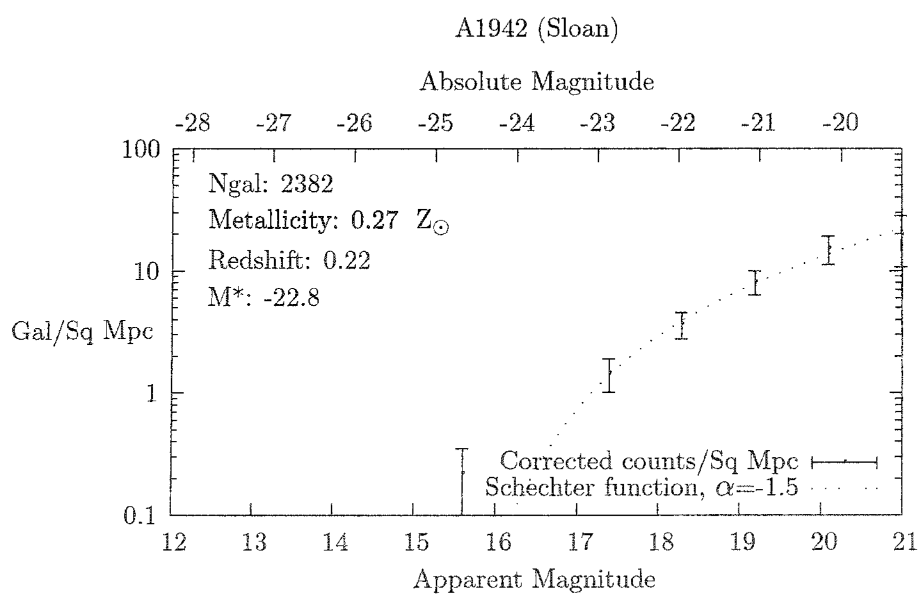
A1942 (Sloan)
Absolute Magnitude
-28
-27
-26
-25
-24
-23
-22
-21
-20
100
10
1
0.1
Gal/Sq Mpc
Ngal: 2382
Metallicity: 0.27 Z⊙
Redshift: 0.22
M*: -22.8
Corrected counts/Sq Mpc
Schechter function, α=-1.5
12
13
14
15
16
17
18
19
20
21
Apparent Magnitude

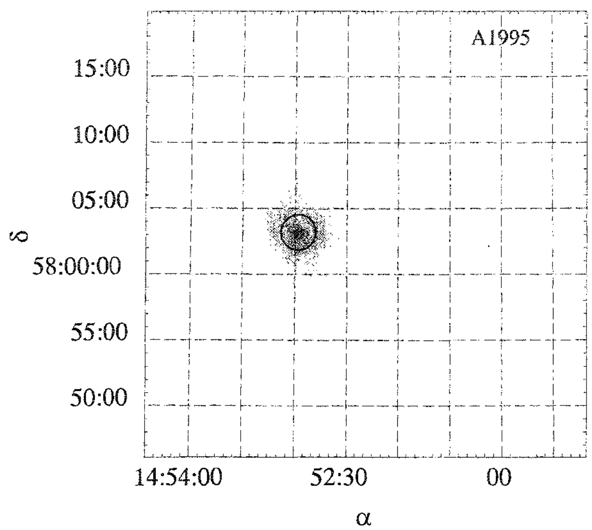
A1995
15:00
10:00
05:00
δ
58:00:00
55:00
50:00
14:54:00
52:30
00
α

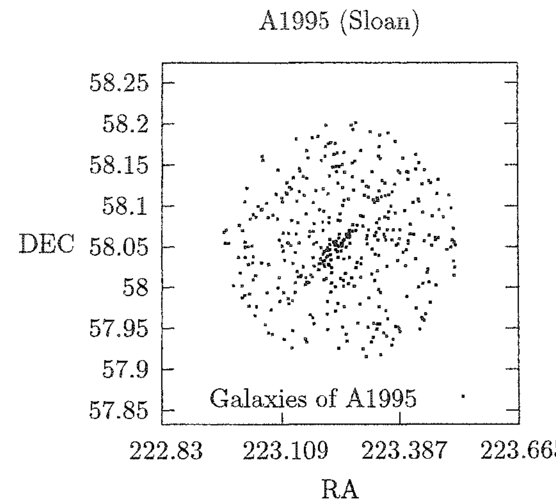
A1995 (Sloan)
58.25
58.2
58.15
58.1
DEC 58.05
58
57.95
57.9
57.85
Galaxies of A1995
222.83
223.109
223.387
223.665
RA

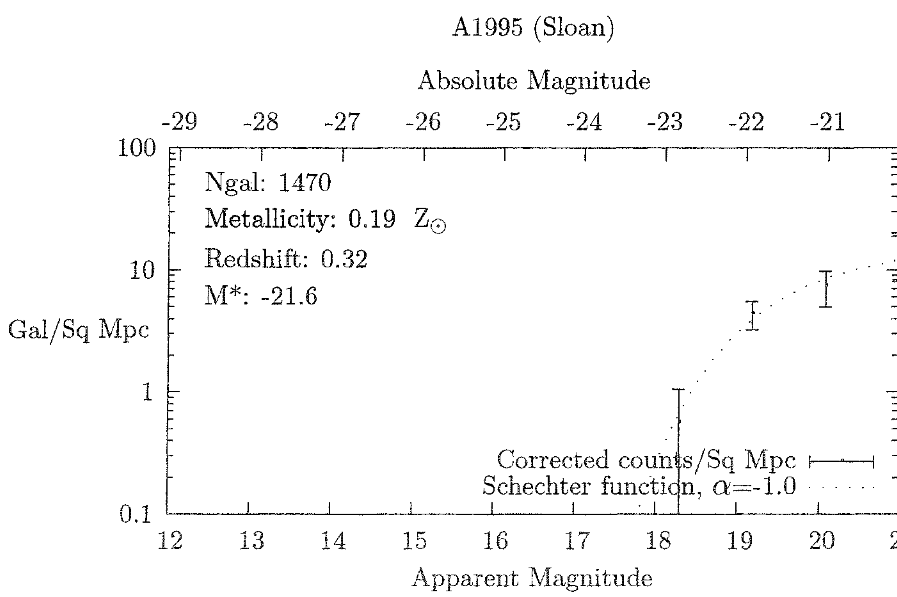
A1995 (Sloan)
Absolute Magnitude
-29 -28 -27 -26 -25 -24 -23 -22 -21
100
10
1
0.1
Gal/Sq Mpc
Ngal: 1470
Metallicity: 0.19 Z⊙
Redshift: 0.32
M*: -21.6
Corrected counts/Sq Mpc
Schechter function, α=-1.0
12 13 14 15 16 17 18 19 20 21
Apparent Magnitude

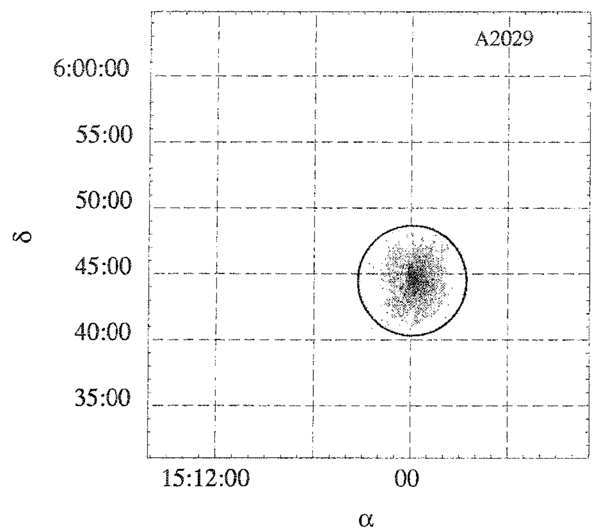
A2029
6:00:00
55:00
50:00
45:00
40:00
35:00
δ
15:12:00
00
α

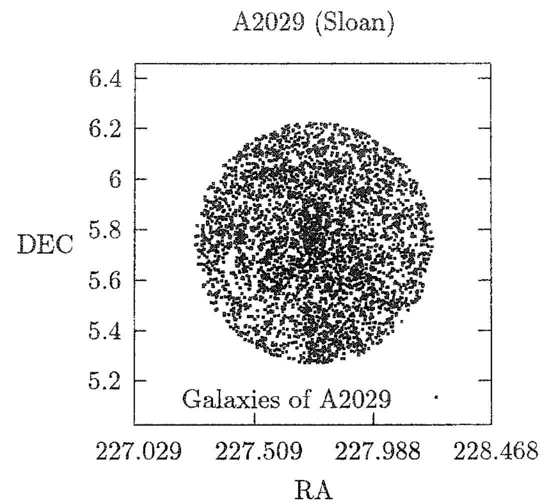
A2029 (Sloan)
6.4
6.2
6
5.8
5.6
5.4
5.2
DEC
Galaxies of A2029
227.029
227.509
227.988
228.468
RA

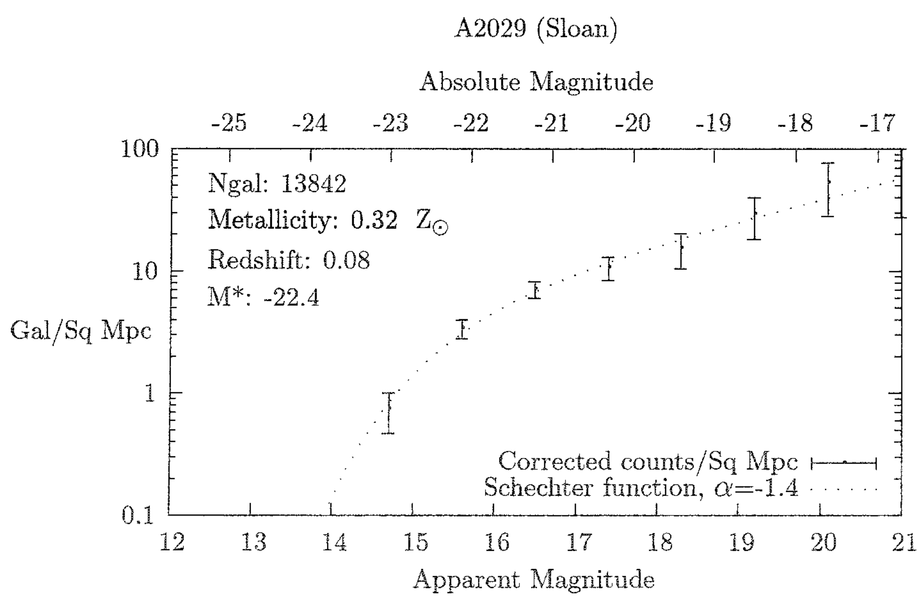
A2029 (Sloan)
Absolute Magnitude
-25 -24 -23 -22 -21 -20 -19 -18 -17
Ngal: 13842
Metallicity: 0.32 Z☉
Redshift: 0.08
M*: -22.4
100
10
1
0.1
Gal/Sq Mpc
Corrected counts/Sq Mpc
Schechter function, α=-1.4
12 13 14 15 16 17 18 19 20 21
Apparent Magnitude

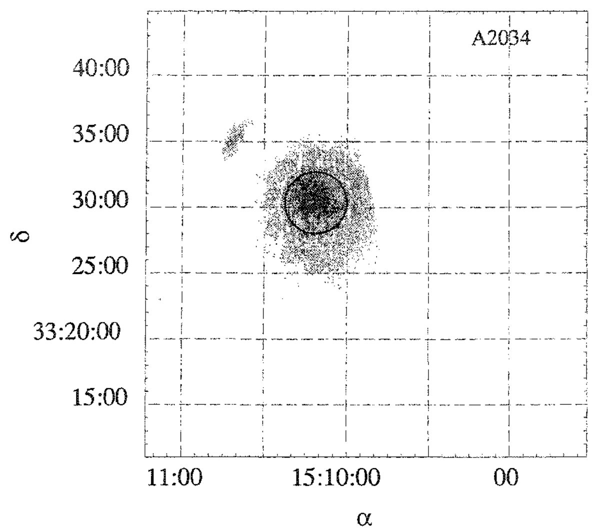
A2034
40:00
35:00
30:00
25:00
33:20:00
15:00
δ
11:00
15:10:00
00
α

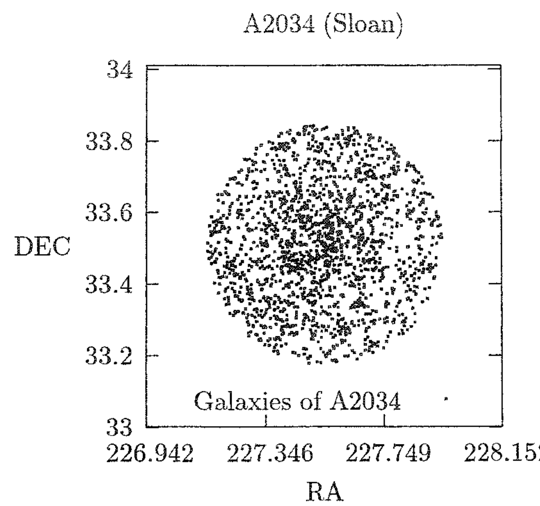
A2034 (Sloan)
34
33.8
33.6
33.4
33.2
33
DEC
Galaxies of A2034
226.942
227.346
227.749
228.152
RA

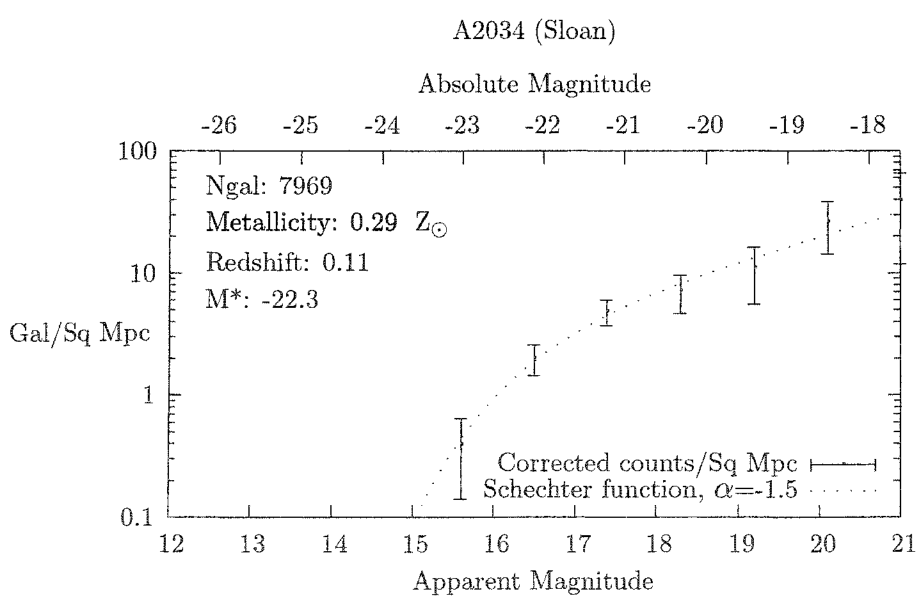
A2034 (Sloan)
Absolute Magnitude
-26
-25
-24
-23
-22
-21
-20
-19
-18
100
10
1
0.1
Gal/Sq Mpc
Ngal: 7969
Metallicity: 0.29 $Z_\odot$
Redshift: 0.11
M*: -22.3
Corrected counts/Sq Mpc
Schechter function, α=-1.5
12
13
14
15
16
17
18
19
20
21
Apparent Magnitude

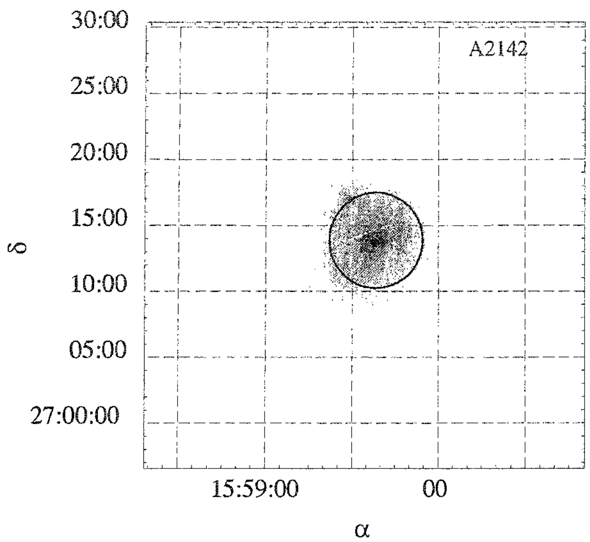
A2142
30:00
25:00
20:00
15:00
10:00
05:00
27:00:00
δ
15:59:00
00
α

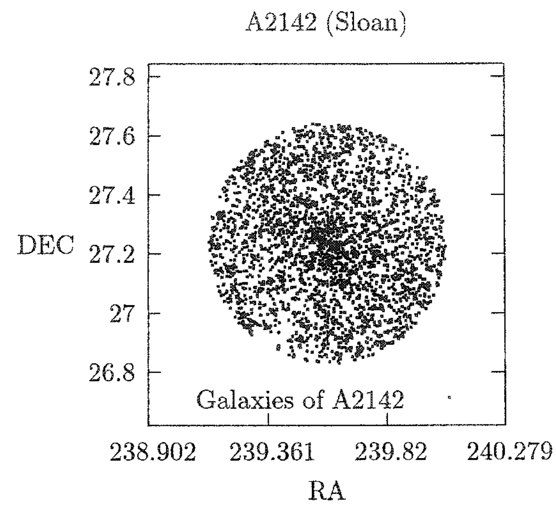
A2142 (Sloan)
DEC
27.8
27.6
27.4
27.2
27
26.8
Galaxies of A2142
238.902
239.361
239.82
240.279
RA

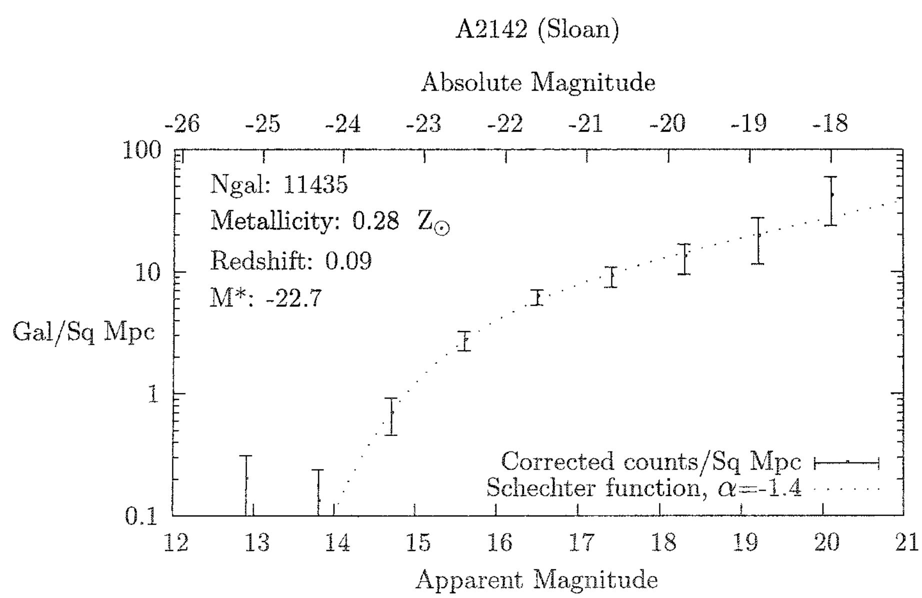
A2142 (Sloan)
Absolute Magnitude
-26
-25
-24
-23
-22
-21
-20
-19
-18
Ngal: 11435
Metallicity: 0.28 $Z_\odot$
Redshift: 0.09
M*: -22.7
Gal/Sq Mpc
100
10
1
0.1
Corrected counts/Sq Mpc
Schechter function, α=-1.4
12
13
14
15
16
17
18
19
20
21
Apparent Magnitude

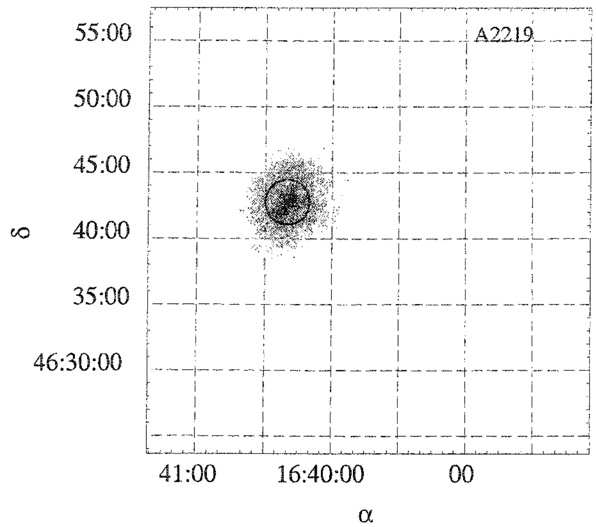
A2219
55:00
50:00
45:00
40:00
35:00
46:30:00
δ
41:00
16:40:00
00
α

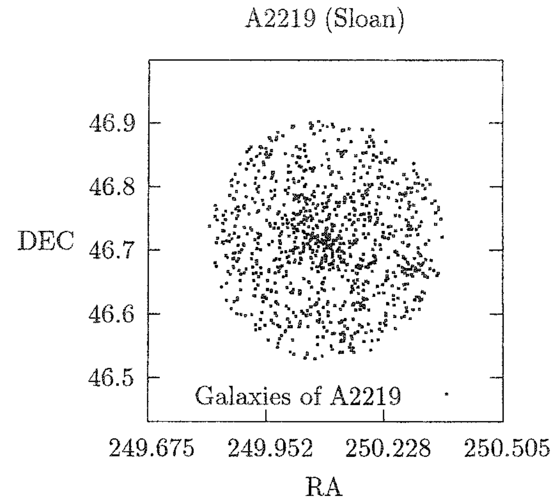
A2219 (Sloan)
46.9
46.8
46.7
46.6
46.5
DEC
Galaxies of A2219
249.675
249.952
250.228
250.505
RA

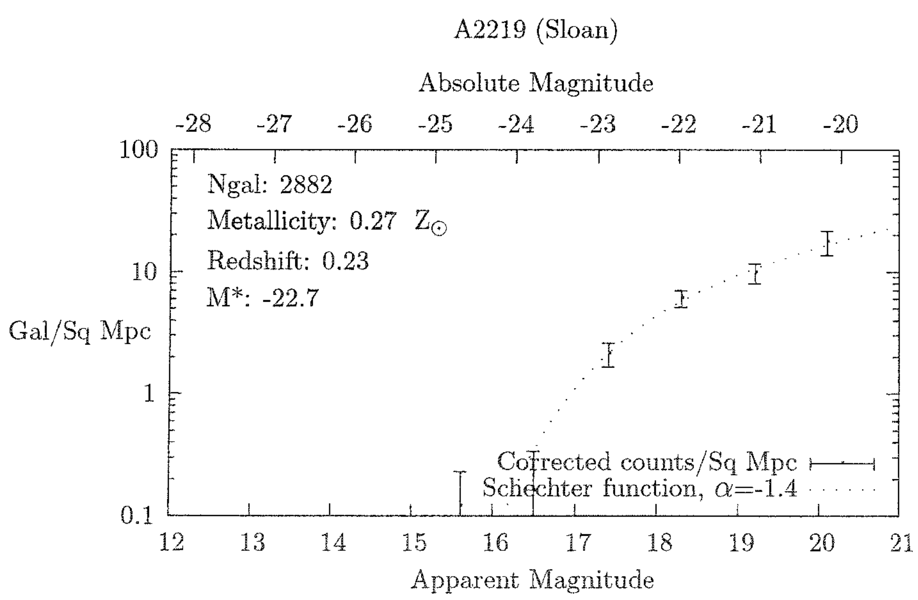
A2219 (Sloan)
Absolute Magnitude
-28
-27
-26
-25
-24
-23
-22
-21
-20
100
10
1
0.1
Gal/Sq Mpc
Ngal: 2882
Metallicity: 0.27 Z⊙
Redshift: 0.23
M*: -22.7
Corrected counts/Sq Mpc
Schechter function, α=-1.4
12
13
14
15
16
17
18
19
20
21
Apparent Magnitude

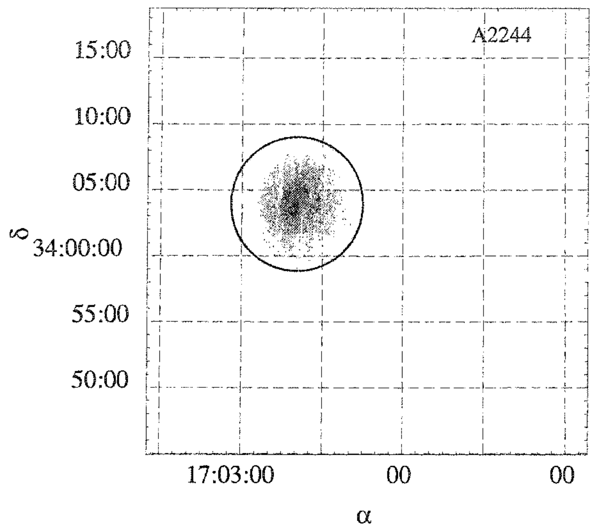
A2244
15:00
10:00
05:00
34:00:00
55:00
50:00
δ
17:03:00
00
00
α

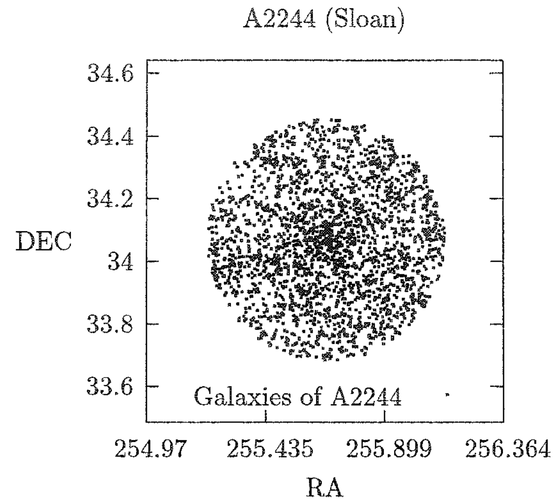
A2244 (Sloan)
34.6
34.4
34.2
34
33.8
33.6
DEC
Galaxies of A2244
254.97
255.435
255.899
256.364
RA

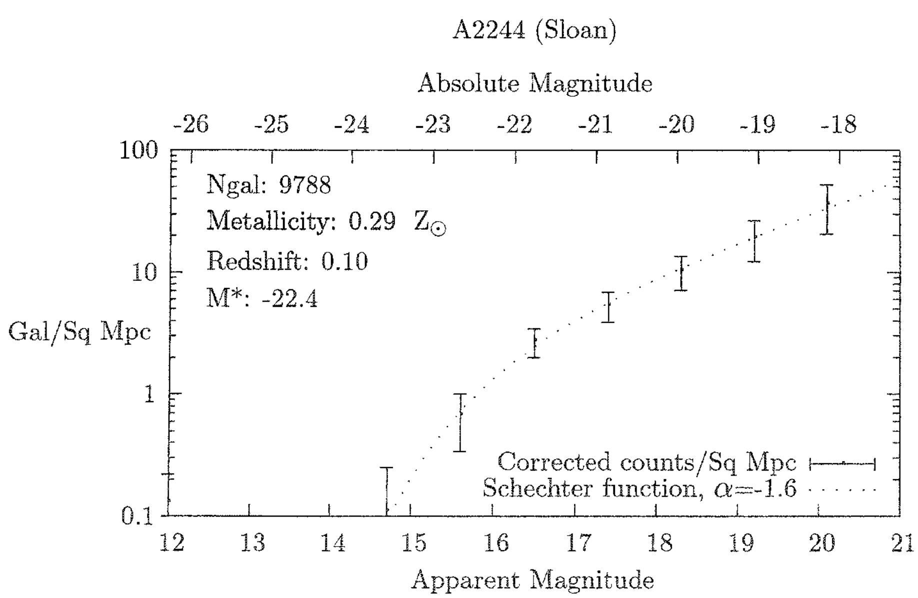
A2244 (Sloan)
Absolute Magnitude
-26
-25
-24
-23
-22
-21
-20
-19
-18
100
10
1
0.1
Gal/Sq Mpc
Ngal: 9788
Metallicity: 0.29 Z⊙
Redshift: 0.10
M*: -22.4
Corrected counts/Sq Mpc
Schechter function, α=-1.6
12
13
14
15
16
17
18
19
20
21
Apparent Magnitude

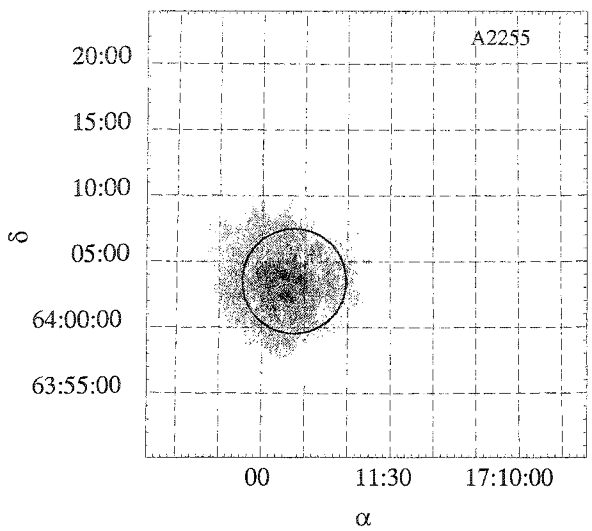
A2255
20:00
15:00
10:00
δ
05:00
64:00:00
63:55:00
00
11:30
17:10:00
α

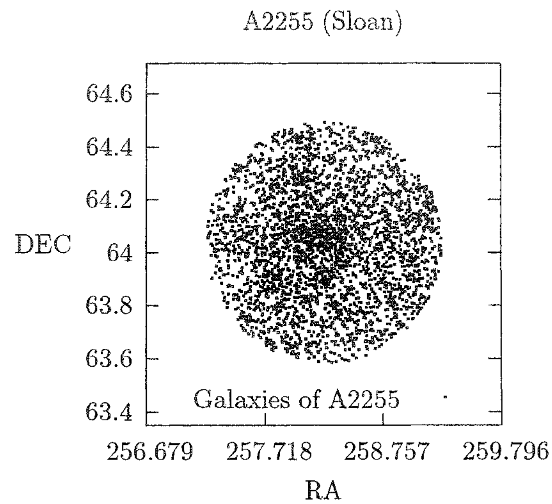
A2255 (Sloan)
64.6
64.4
64.2
DEC
64
63.8
63.6
63.4
Galaxies of A2255
256.679
257.718
258.757
259.796
RA

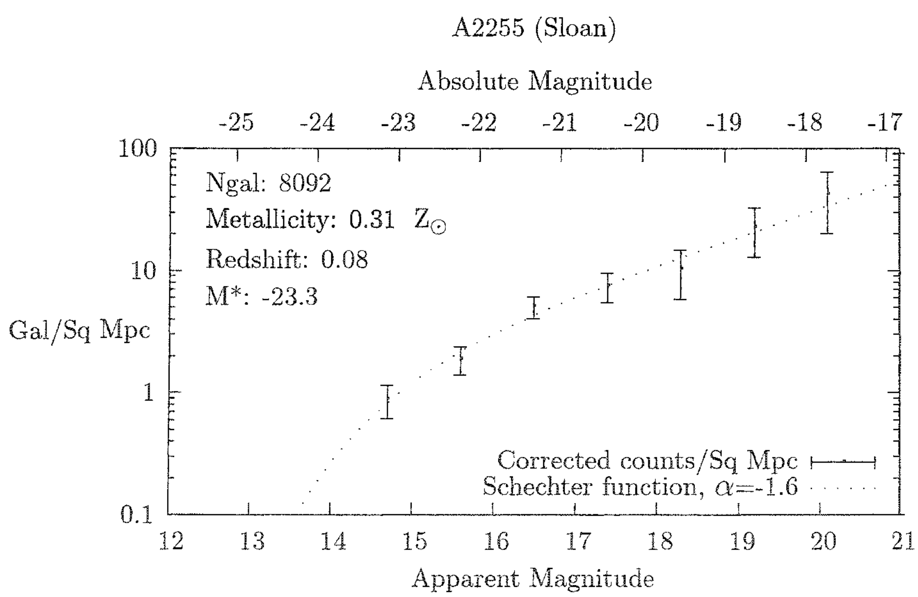
A2255 (Sloan)
Absolute Magnitude
-25
-24
-23
-22
-21
-20
-19
-18
-17
100
10
1
0.1
Gal/Sq Mpc
Ngal: 8092
Metallicity: 0.31 Z⊙
Redshift: 0.08
M*: -23.3
Corrected counts/Sq Mpc
Schechter function, α=-1.6
12
13
14
15
16
17
18
19
20
21
Apparent Magnitude

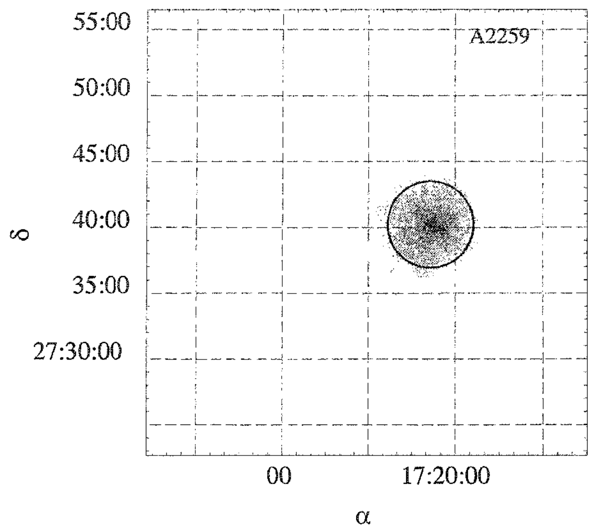
55:00
50:00
45:00
40:00
35:00
27:30:00
A2259
δ
00
17:20:00
α

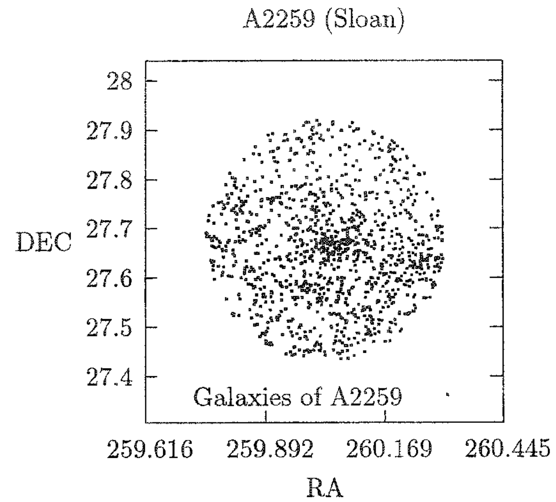
A2259 (Sloan)
DEC
28
27.9
27.8
27.7
27.6
27.5
27.4
Galaxies of A2259
259.616
259.892
260.169
260.445
RA

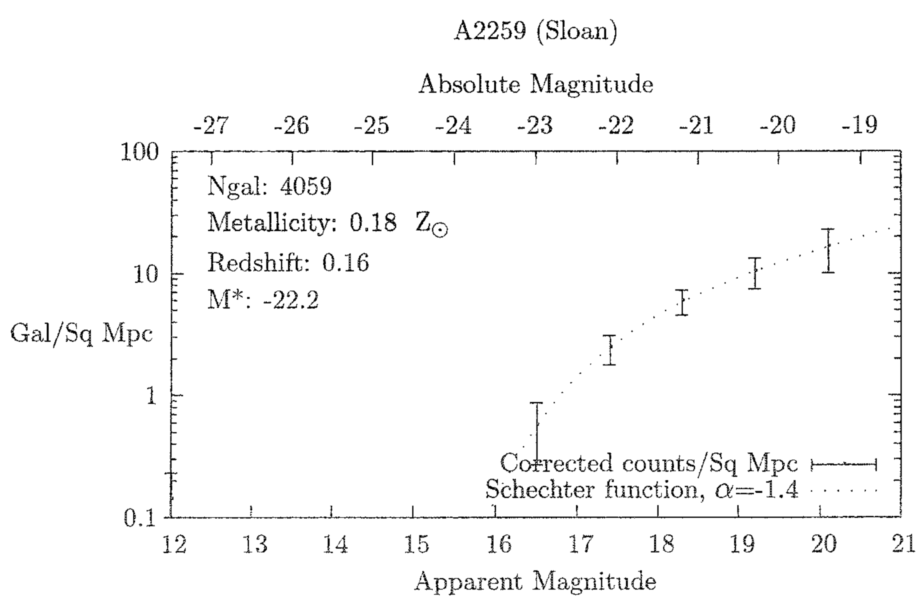
A2259 (Sloan)
Absolute Magnitude
-27
-26
-25
-24
-23
-22
-21
-20
-19
Ngal: 4059
Metallicity: 0.18 Z⊙
Redshift: 0.16
M*: -22.2
Gal/Sq Mpc
100
10
1
0.1
Corrected counts/Sq Mpc
Schechter function, α=-1.4
12
13
14
15
16
17
18
19
20
21
Apparent Magnitude

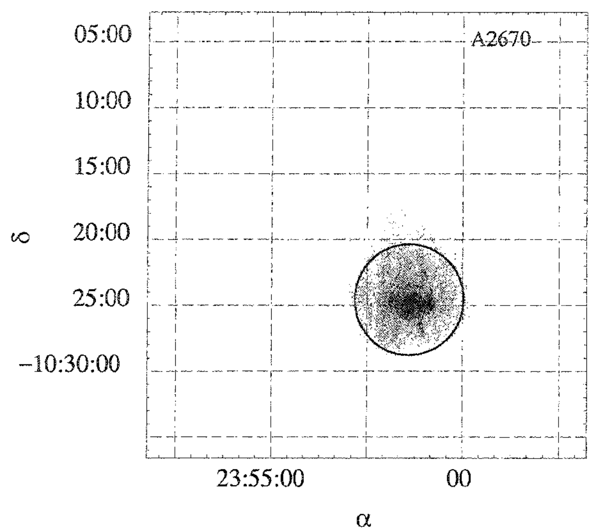
A2670
05:00
10:00
15:00
20:00
25:00
−10:30:00
δ
23:55:00
00
α

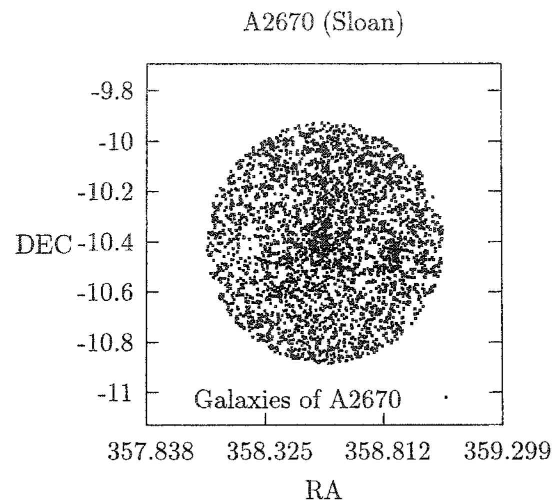
A2670 (Sloan)
DEC
-9.8
-10
-10.2
-10.4
-10.6
-10.8
-11
Galaxies of A2670
357.838
358.325
358.812
359.299
RA

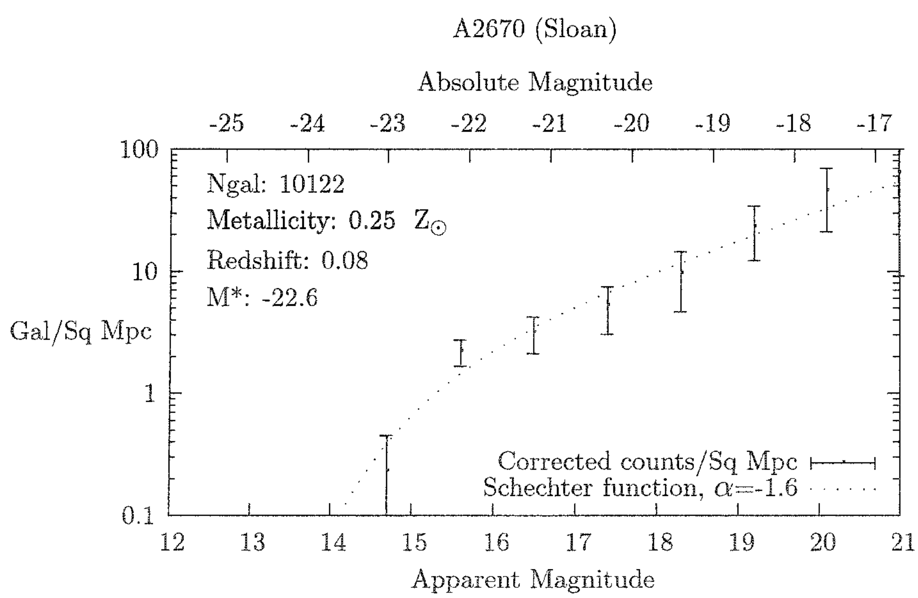
A2670 (Sloan)
Absolute Magnitude
-25
-24
-23
-22
-21
-20
-19
-18
-17
Ngal: 10122
Metallicity: 0.25 Z⊙
Redshift: 0.08
M*: -22.6
Gal/Sq Mpc
100
10
1
0.1
Corrected counts/Sq Mpc
Schechter function, α=-1.6
12
13
14
15
16
17
18
19
20
21
Apparent Magnitude

CHAPTER 9

RESULTS AND CONCLUSIONS

In this chapter we present results from the luminosity function of all the clusters in our sample. We also graph M_r^*, α, and the redshifts versus the X-ray metallicities of the ICM for the clusters.

9.1 ICM Metallicity and the Cluster Luminosity Functions

The metallicity of the intra-cluster medium is measured using bremsstrahlung X-rays from the cluster centers. This metallicity is more than what is expected in a primordial gas. This suggests that the ICM is enriched with metals from the ISM of the cluster galaxies. If this is true, a connection between the ICM metallicity and optical parameters of the galaxies can be expected. In efforts to parameterize the optical data from the clusters, we have generated luminosity functions of a sample of clusters with a wide metallicity range. The luminosity functions are used to compute a characteristic magnitude (M_r^*) and the faint-end slope for each cluster. This is done by fitting Schechter function of the form

$$n(M)dM = k\ N^*\ e^{k(\alpha+1)(M^*-M)-e^{k\ (M^*-M)}}dM,$$

to the cluster luminosity functions. The parameters are as described in chapter 8.

Results are presented in Table 5 and Table 6. The columns contain the following data:

Column (1).—Abell number.

Column (2).—Redshift from Horner (2001) confirmed with Rood (1999).

Column (3).—ICM metallicity from Horner (2001) and White (2000).

Column (4).—90% confidence interval for metallicity.

Column (5).—Characteristic absolute magnitude from the cluster luminosity functions.

Column (6).—α, representing the faint-end slope of the cluster luminosity functions.

Column (7).—χ^2/ν for the Schechter function fits to the luminosity functions. ν is the degrees of freedom.

Table 5 Results from MDM data

Cluster (1)	z (2)	$Z(\mathrm{Z}_\odot)$ (3)	90 %cl (4)	M^* (5)	α (6)	χ^2/ν (7)
A0963	0.21	0.34	0.26 - 0.42	-22.7 $\pm$ 0.1	0.00 $\pm$ 0.14	0.11
A0990	0.14	0.23	0.18 - 0.27	-22.9 $\pm$ 0.5	-0.30 $\pm$ 0.47	2.21
A1068	0.14	0.42	0.36 - 0.48	-22.9 $\pm$ 0.5	-0.20 $\pm$ 0.63	1.77
A1204	0.17	0.35	0.28 - 0.43	-23.3 $\pm$ 0.4	-1.20 $\pm$ 0.25	0.99
A1553	0.17	0.25	0.18 - 0.32	-22.2 $\pm$ 0.6	0.30 $\pm$ 0.94	2.41
A1650	0.08	0.40	0.37 - 0.43	-22.6 $\pm$ 0.4	-0.70 $\pm$ 0.45	0.58
A1689	0.18	0.32	0.28 - 0.37	-22.6 $\pm$ 0.4	0.40 $\pm$ 0.64	0.90
A1914	0.17	0.30	0.24 - 0.36	-23.1 $\pm$ 0.6	-1.20 $\pm$ 0.37	0.96
A1942	0.22	0.27	0.12 - 0.44	-22.4 $\pm$ 0.3	-0.80 $\pm$ 0.31	0.19
A2034	0.11	0.29	0.23 - 0.34	-22.6 $\pm$ 0.3	-1.00 $\pm$ 0.24	0.31
A2104	0.16	0.32	0.26 - 0.38	-22.7 $\pm$ 0.5	-0.70 $\pm$ 0.49	1.31
A2142	0.09	0.28	0.23 - 0.33	-22.8 $\pm$ 0.3	-0.90 $\pm$ 0.20	0.87
A2204	0.15	0.39	0.34 - 0.44	-23.2 $\pm$ 0.2	-0.80 $\pm$ 0.17	0.09
A2218	0.18	0.20	0.14 - 0.25	-22.3 $\pm$ 0.9	0.60 $\pm$ 2.17	2.76
A2219	0.23	0.27	0.19 - 0.34	-22.8 $\pm$ 0.5	-0.40 $\pm$ 0.42	0.18
A2261	0.22	0.37	0.29 - 0.45	-22.8 $\pm$ 0.3	0.60 $\pm$ 0.61	0.77

Table 6 Results from SDSS data

Cluster (1)	z (2)	$Z(\mathrm{Z}_\odot)$ (3)	90 %cl (4)	M^* (5)	α (6)	χ^2/ν (7)
A0267	0.23	0.26	0.17 - 0.34	-22.0 ± 0.1	-1.10 ± 0.06	0.02
A0611	0.29	0.19	0.12 - 0.27	-22.5 ± 0.2	-1.50 ± 0.10	0.04
A0697	0.28	0.24	0.17 - 0.31	-22.5 ± 0.5	-1.60 ± 0.28	0.32
A0773	0.20	0.29	0.20 - 0.38	-22.1 ± 0.1	-1.40 ± 0.07	0.09
A0854	0.21	0.09	0.00 - 0.19	-22.3 ± 0.3	-1.40 ± 0.13	0.13
A0959	0.35	0.04	0.00 - 0.19	-22.3 ± 0.2	-1.20 ± 0.12	0.04
A0963	0.21	0.34	0.26 - 0.42	-21.8 ± 0.1	-1.20 ± 0.05	0.02
A0990	0.14	0.23	0.18 - 0.27	-22.2 ± 0.3	-1.40 ± 0.13	0.15
A1068	0.14	0.42	0.36 - 0.48	-22.4 ± 0.5	-1.50 ± 0.22	0.35
A1430	0.21	0.00	0.00 - 0.08	-21.2 ± 0.1	-1.20 ± 0.05	0.00
A1553	0.17	0.25	0.18 - 0.32	-21.9 ± 0.1	-1.20 ± 0.06	0.03
A1576	0.30	0.25	0.14 - 0.36	-22.0 ± 0.3	-1.20 ± 0.20	0.14
A1650	0.08	0.40	0.37 - 0.43	-22.7 ± 0.5	-1.80 ± 0.11	0.21
A1682	0.23	0.21	0.10 - 0.32	-22.5 ± 0.2	-1.50 ± 0.08	0.10
A1689	0.18	0.32	0.28 - 0.37	-22.3 ± 0.3	-1.10 ± 0.19	0.39
A1704	0.22	0.37	0.26 - 0.49	-22.6 ± 0.2	-1.40 ± 0.10	0.01
A1763	0.19	0.12	0.05 - 0.19	-21.6 ± 0.2	-1.40 ± 0.15	0.12
A1774	0.17	0.08	0.02 - 0.14	-21.6 ± 0.1	-1.30 ± 0.06	0.03
A1835	0.25	0.30	0.24 - 0.37	-21.7 ± 0.4	-0.80 ± 0.40	1.05
A1914	0.17	0.30	0.24 - 0.36	-22.7 ± 0.2	-1.60 ± 0.08	0.12
A1942	0.22	0.27	0.12 - 0.44	-22.8 ± 0.4	-1.50 ± 0.12	0.19
A1995	0.32	0.19	0.01 - 0.36	-21.6 ± 0.5	-1.00 ± 0.47	0.52
A2029	0.08	0.32	0.29 - 0.35	-22.4 ± 0.2	-1.40 ± 0.07	0.29
A2034	0.11	0.29	0.23 - 0.34	-22.3 ± 0.3	-1.50 ± 0.10	0.22
A2142	0.09	0.28	0.23 - 0.33	-22.7 ± 0.2	-1.40 ± 0.07	0.24
A2219	0.23	0.27	0.19 - 0.34	-22.7 ± 0.4	-1.40 ± 0.19	0.34
A2244	0.10	0.29	0.25 - 0.33	-22.4 ± 0.2	-1.60 ± 0.07	0.09
A2255	0.08	0.31	0.26 - 0.35	-23.3 ± 0.4	-1.60 ± 0.08	0.30
A2259	0.16	0.18	0.12 - 0.24	-22.2 ± 0.0	-1.40 ± 0.02	0.00
A2670	0.08	0.25	0.18 - 0.33	-22.6 ± 0.6	-1.60 ± 0.15	0.68

Figure 27 and 28 show the plots of metallicity versus M_r^*, the "knee" of the luminosity functions, for MDM and SDSS data respectively. The figures show a weak trend of increasing brightness for M_r^* for clusters with increasing metallicity. Since the sizes of the error-bars are relatively large, there is no strong support for the trend. The best fits are used as indicators for a possible trend.

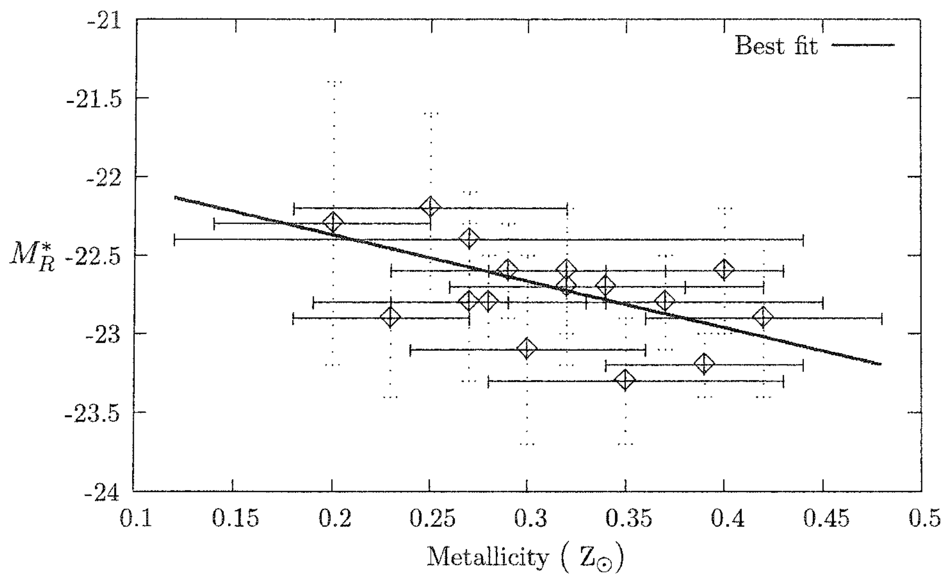

Figure 27 M_r^* versus Metallicity (MDM data)

When the data are binned around the median value of metallicity range (0.31 $Z_\odot$ for MDM and 0.26 $Z_\odot$ for SDSS), and compared with low metallicity clusters, on an average, the higher metallicity clusters are found to be 0.2 magnitudes brighter for MDM data and 0.4 magnitudes brighter for SDSS data.

The parameters derived from the luminosity functions, M_r^* are α, depend on the availability of the data at the faint end of the functions. For distant clusters the amount of data at the faint end of the luminosity functions is not sufficient to compute the faint-end slope of the functions with certainty. The faint-end slope also plays a role in determining the value for M_r^*, which is illustrated in Figure 29.

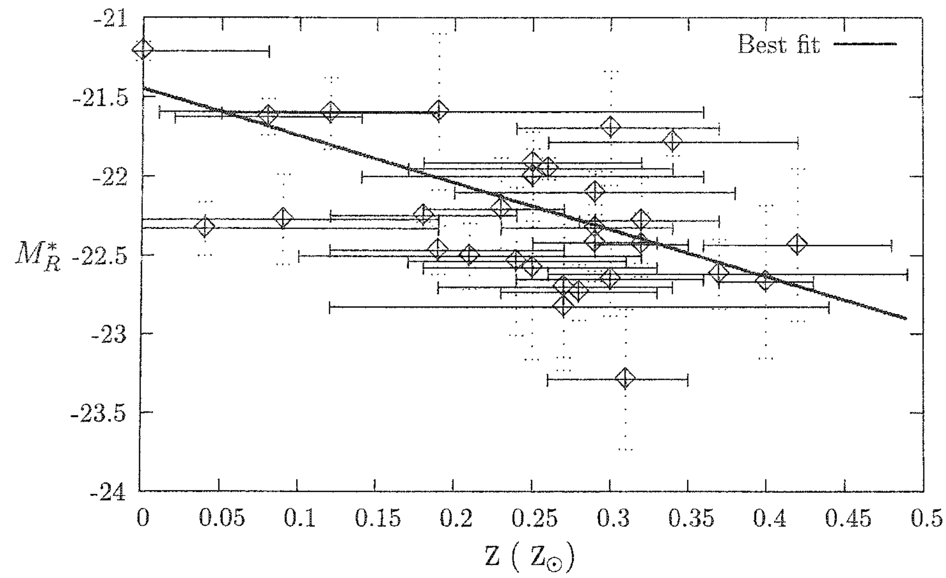

Figure 28 M_r^* versus Metallicity (SDSS data)

Therefore, uncertainty in measuring α induces uncertainty in the measurement of M_r^*. If only nearby clusters are used, α and M_r^* can be determined with improved certainty. For SDSS data, cluster with redshift $\leq$ 0.2 provide us with data for the faint-end slope at least up to 3 magnitudes beyond M_r^*. This results in better measurements of α and hence M_r^*. Figure 30 is a plot of metallicity versus M_r^* for cluster with redshift $\leq$ 0.2 for SDSS data. Some of the MDM observations were done on non-photometric nights. This depleted the number of galaxies towards the faint-end of the luminosity functions. Therefore, a redshift constraint on MDM data does not lead to better measurements of M_r^*. With redshift constraint on the SDSS data, when the data are binned around the median value of new metallicity range (0.29 $Z_\odot$), and compared with low metallicity clusters, on an average, the higher metallicity clusters are found to be 0.5 magnitudes brighter. This is a small improvement in the contrast between M_r^* for low-metallicity clusters and M_r^* for high-metallicity clusters.

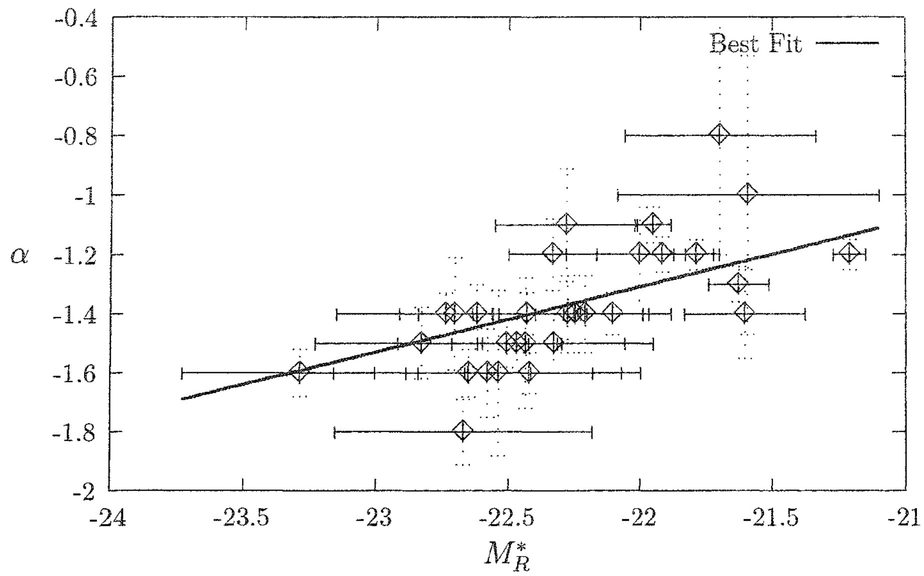

Figure 29 M_r^* versus α (SDSS)

Figure 31 is a plot of α versus metallicity. A week trend can be expected due to the trends between α and M_r^* (Figure 29) and, M_r^* and metallicity (Figure 30). As discussed in the introduction, it has been suggested that decreasing galactic mass can lead to increasing outflow of metals from the galaxies due to that fact that lower-mass (faint) galaxies have shallower potential wells. If such a correlation exists, a relation between number of faint galaxies and ICM metallicity can be expected. Bigger values of $|\alpha|$ correspond to greater number of faint galaxies. Figure 31 is in qualitative agreement with this. This result, if confirmed with improved data, implies that supernovae outflows could be one of the dominant mechanisms for ICM enrichment. Bigger values of $|\alpha|$ also corresponds to greater densities. Greater densities make ram pressure stripping and galaxy-galaxy interactions more likely. Therefore, the results also support these mechanisms.

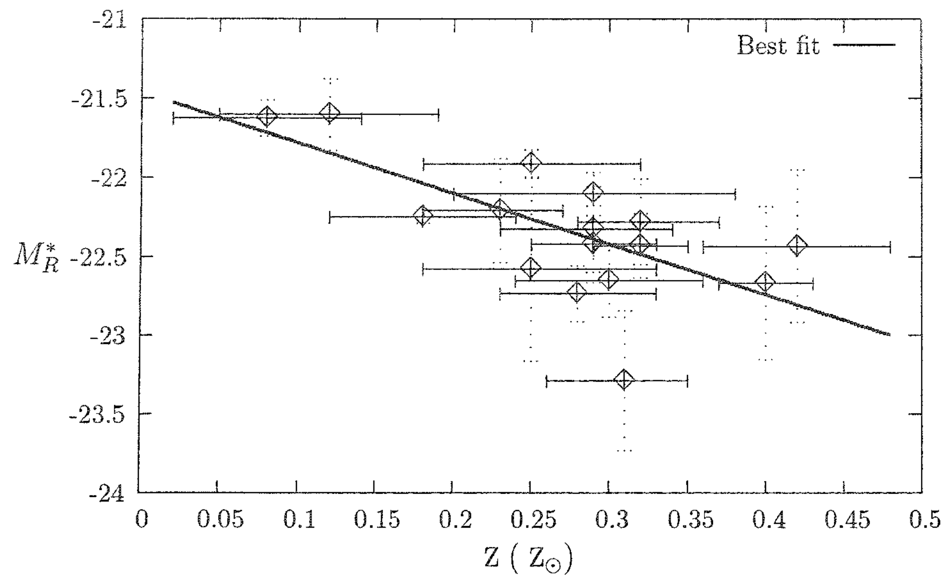

Figure 30 M_r^* versus Metallicity for nearby clusters (SDSS archive)

9.2 ICM Metallicity and Redshift

As discussed in the introduction, if ram-pressure stripping is a dominant mechanism for transferring metallicity to the ICM from the ISM, clusters that are further away would have had less events of such transfer. This is because it would take time for cluster galaxies to plunge through the primordial ICM. If this is the case, a relation between redshift and ICM metallicity can be expected. Figure 32 is a plot of ICM metallicity in solar units versus redshift. The results are in agreement with Mushotzky & Loewenstein (1997) and Horner (2001) showing no correlation of metallicity with redshift. Better metallicity measurements are needed to reach a definitive conclusion.

9.3 Future Work

This project provides marginal evidence of a connection between the metallicity of the intra-cluster and the galaxies within the clusters. The errors in the metallicity and M_r^* measurements make it difficult to claim with certainty that there is a

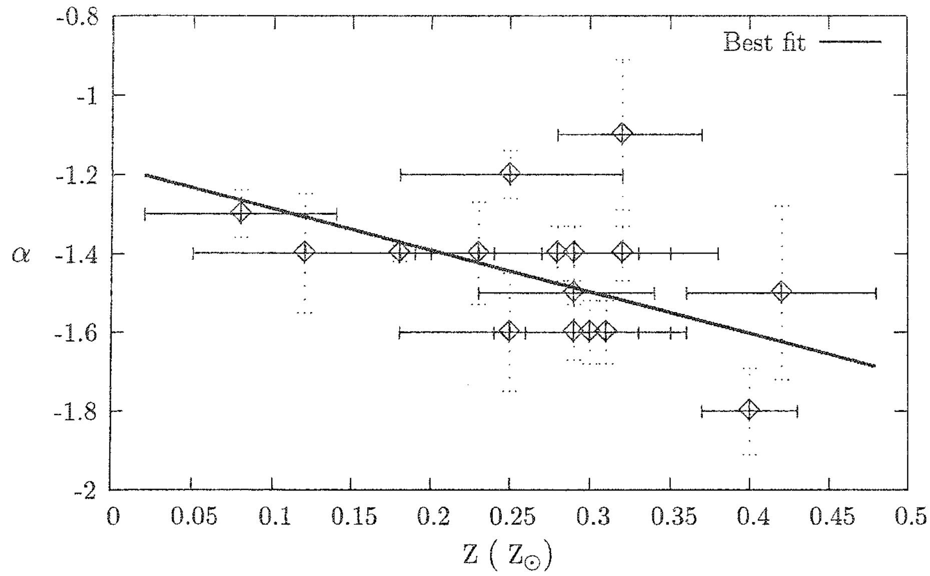

Figure 31 α versus Metallicity for nearby clusters (SDSS archive)

connection.

The metallicity error-bars are from the model fitting to the X-ray spectra that come from the ASCA telescope. The spectral resolution ($E/\Delta E$) of ASCA is 50 at 6 keV. New generation X-ray telescope Chandra, has spectral resolution of of 60-1000 for an energy range of 0.5 -10 keV. Therefore, Chandra can provide metallicity measurements with much smaller errors.

The ICM metallicity varies from region to region in a given cluster (De Grandi & Molendi 2001; White 2000). The metallicity used for this project is found using all the X-ray light received from the clusters. This smoothes out any gradient in the metallicity that could exist. It also induces spread in the spectral line resulting into larger errors in metallicity measurements. The spatial resolution of the Chandra telescope is less than 1″ compared to 20% photons within 1′ for ASCA. Such higher resolution of can provide better measurements for the metallicity gradients.

The error in M_r^* measurements are from the Schechter function fits to the luminosity functions. χ^2/ν values for our fits are small providing us with $\sim$ 10%

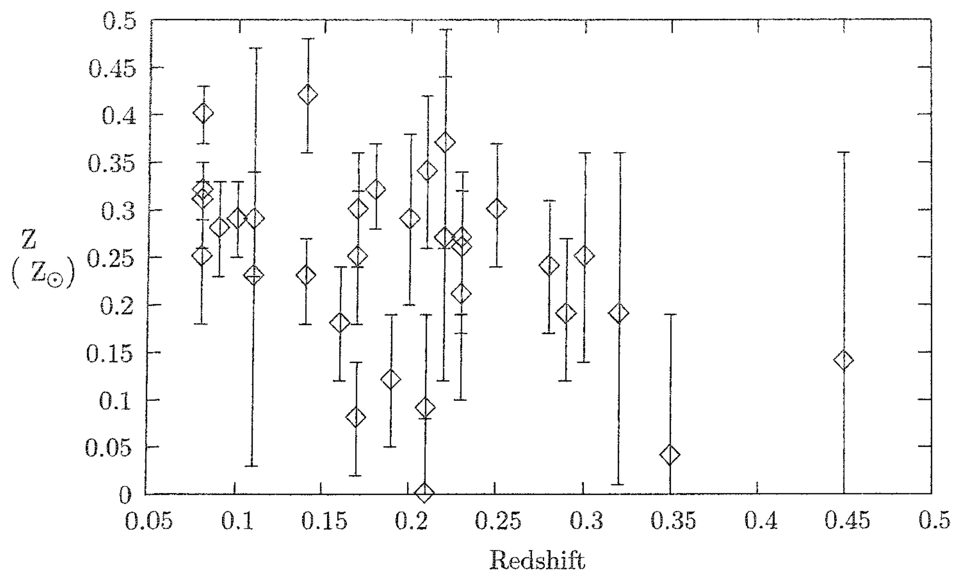

Figure 32 Total Metallicity versus Redshift

probability of getting smaller χ^2/ν values. Therefore, the errors in M_r^* and α primarily depend on the number of field galaxies in each magnitude bin. If a sample of nearby clusters with redshifts of individual galaxies is observed, the cluster members can easily be identified. In such case, there would be no need to subtract the field galaxies, and the error induced by the field galaxies can be eliminated. This can result in much smaller errors in the M_r^* and α measurement.

APPENDIX

ABSOLUTE MAGNITUDE

A difference of 5 magnitudes equals to a factor of 100 in apparent brightness. The magnitude scale is logarithmic and therefore,

$$\frac{m-5}{m} = \frac{\log(100 \times f)}{\log(f)},$$

where m is the apparent magnitude and f is the observed flux from an object. The above equation can be rewritten as

$$m = -2.5\log(f).$$

Flux (f) depends on the luminosity (L) and the distance (r) to the object.

$$f = \frac{L}{4\pi r^2}.$$

The distance modulus which is the difference between the absolute magnitude (M) and the apparent magnitude (m) for an object would depend on the flux received from the object (f_m), and the flux that would be received (f_M) if the object were at a distance of 10 parsec, since the absolute magnitude is the magnitude of an object if it were at the distance of 10 parsec.

$$M - m = 2.5\log(f_m/f_M),$$

which translates to

$$M - m = 5\log(10\ \mathrm{pc}/r).$$

$M - m$ is called the distance modulus.

For an object in the Hubble flow, the luminosity distance, r, is

$$r \simeq (1+z)\frac{c}{H_0}\left(z - \frac{1+q_0}{2}z^2\right),$$

where H is the Hubble constant, z is the redshift and $q_0 = 0.5\Lambda_m - \Lambda_k$. Λ_m and Λ_k are the density parameters (Peacock 1999). Substituting the r above into $M - m$ gives us

$$M - m \simeq 5\log\left(\frac{10\ \mathrm{pc}}{(1+z)\frac{c}{H_0}\left(z - \frac{1+q_0}{2}z^2\right)}\right).$$

This can be rewritten as,

$$M - m \simeq 5\log\left(\frac{100\ h \times 10\ \mathrm{pc}}{c\ (1+z)(z - 0.1875z^2)}\right),$$

with 100 $h = H_0$ in the units of Km/s/Mpc, $\Lambda_m = 0.25$ and Λ_k=0.75 (Bahcall 2000). This can be simplified to,

$$M - m \simeq 5\log(100 \times 10\ \mathrm{pc}/c) + 5\log(h) - 5\log(z) - 5\log(1+z) - 5\log(1 - 0.1875z),$$

which reduces to

$$M - m \simeq -42.385 + 5\log(h) - 5\log(z) - 5\log(1+z) - 5\log(1 - 0.1875z)$$

for $c = 2.998 \times 10^8$ Km/s.

The above distance modulus is bolometric and assumes no galactic extinction. For a given bandpass (i), after correcting for the extinction (A_i), the absolute magnitude becomes,

$$M_i \simeq m_i - 42.385 + 5\log(h) - 5\log(z) - 5\log(1+z) - 5\log(1 - 0.1875z) - A_i,$$

or simply,

$$M_i = m_i - \mu - A_i,$$

with

$$\mu \simeq 42.385 - 5\log(h) + 5\log(z) + 5\log(1+z) + 5\log(1 - 0.1875z).$$

BIBLIOGRAPHY

Abell, G.O. 1958, ApJS, 3, 211

Abell, G. O. 1975 in *Stars and Stellar Systems*, Vol. 9, *Galaxies and the Universe*, ed A. Sandage, M. Sandage, and J. Kristian, p. 601. Chicago: University of Chicago

Aguirre, A., Hernquist, L., Schaye, J., Katz, N., Weinberg, D. H., & Gardner, J. 2001, ApJ, 561, 521

Bekki, K., Couch, W. J., & Shioya, Y. 2002, ApJ, 577, 651

Bertin, E. & Arnouts, S. 1996, A&AS, 117, 393

Butcher, H. & Oemler, A. 1984, ApJ, 285, 426

Carlberg, R. G., Yee, H. K. C., Ellingson, E., Abraham, R., Gravel, P., Morris, S., & Pritchet, C. J. 1996, ApJ, 462, 32

Domainko, W., Gitti, M., Schindler, S., and Kapferer, W., arXiv:astro-ph/0405493

Dressler, A., Smail, I., Poggianti, B. M., Butcher, H., Couch, W. J., Ellis, R. S., & Oemler, A. J. 1999, ApJS, 122, 51

De Filippis, E., Schindler, S. and Castillo-Morales, A. arXiv:astro-ph/0201349

Gnedin, N. Y. 1998, MNRAS, 294, 407

Goto, T., et al. 2003, PASJ, 55, 757

De Grandi, S. & Molendi, S. 2001, ApJ, 551, 153

Gunn, J. E. & Gott, J. R. I. 1972, ApJ, 176, 1

Horner, D., PhD Thesis 2001

Ikebe, Y., Reiprich, T. H., Böhringer, H., Tanaka, Y., & Kitayama, T. 2002, A&A, 383, 773

Landolt, A. U. 1992, AJ, 104, 340

Larson, R. B. 1974, MNRAS, 169, 229

Larson, R. B. & Dinerstein, H. L. 1975, PASP, 87, 911

Lehnert, M. D., Heckman, T. M., & Weaver, K. A. 1999, ApJ, 523, 575

Lutz, R. K., 1979, The Comp. J. 23, 262

Mathews, W. G. & Baker, J. C. 1971, ApJ, 170, 241

Mewe, R., Gronenschild, E. H. B. M., & van den Oord, G. H. J. 1985, A&AS, 62, 197

Mewe, R., Lemen, J. R., & van den Oord, G. H. J. 1986, A&AS, 65, 511

Morrison, R. & McCammon, D. 1983, ApJ, 270, 119

Mushotzky, R., Loewenstein, M., Arnaud, K. A., Tamura, T., Fukazawa, Y., Matsushita, K., Kikuchi, K., & Hatsukade, I. 1996, ApJ, 466, 686

Parolin, I., Molinari, E., & Chincarini, G. 2003, A&A, 407, 823

Peacock, J. A. 1999, Cosmological physics (Cambridge University Press), p. 90-92

Raymond, J. C. & Smith, B. W. 1977, ApJS, 35, 419

Renzini, A. 1997, ApJ, 488, 35

rosati, P. *et al.*, arXiv:astro-ph/0309546

Sandage, A. 1973, ApJ, 183, 731

Sarazin, C. L. 1988, Cambridge Astrophysics Series, Cambridge: Cambridge University Press, 1988

Schechter, P. 1976, ApJ, 203, 297

Schindler, S. 2004, Ap&SS, 289, 419

Schlegel, D. J., Finkbeiner, D. P., & Davis, M. 1998, ApJ, 500, 525

Shu, F. H., 1986, The Physical Universe (University Science Books), p. 348

Stark, A. A., Gammie, C. F., Wilson, R. W., Bally, J., Linke, R. A., Heiles, C., & Hurwitz, M. 1992, ApJS, 79, 77

Struble, M. F. & Rood, H. J. 1999, ApJS, 125, 35

Tamura, N., Hirashita, H., & Takeuchi, T. T. 2001, ApJ, 552, L113

Tanaka, Y., Inoue, H., & Holt, S. S. 1994, PASJ, 46, L37

Wang, Q. D., Owen, F. and Ledlow, M. arXiv:astro-ph/0404602

White, D. A. & Buote, D. A. 2000, MNRAS, 312, 649

White, D. A. 2000, MNRAS, 312, 663

Wiebe, D. S., Shustov, B. M., & Tutukov, A. V. 1999, A&A, 345, 93

Wolf, M. 1906, Astronomische Nachrichten, 170, 211

Wolf, C., et al. 2004, A&A, 421, 913

De Young, D. S. 1978, ApJ, 223, 47

Zwicky, F., 1957, Morphological Astronomy (Berlin: Springer)

VITA

Graduate College
University of Nevada, Las Vegas

Sandip G. Thanki

Local Address:
9225 West Charleston Blvd., Apartment 2090
Las Vegas, NV 89117

Degrees:
Bachelor of Science, Physics and Electrical Engineering, 1997
Widener University, PA

Master of Science, Physics, 1999
University of Nevada Las Vegas, NV

Dissertation Title: X-ray Metallicities and Luminosity Functions of Galaxy Clusters

Dissertation Committee:
Chairperson, Dr. George Rhee, Ph. D.
Committee Member, Dr. Stephen Lepp, Ph. D.
Committee Member, Dr. Lon Spight, Ph. D.
Graduate Faculty Representative, Dr. David Emerson, Ph. D.